Learning from Plants – A Biologically Inspired Multi-Cellular Approach towards Multi-Functional Adaptive Structure based on Fluidic Flexible Matrix Composite

by

Suyi Li

A dissertation submitted in partial fulfillment
of the requirements for the degree of
Doctor of Philosophy
(Mechanical Engineering)
in the University of Michigan
2014

Doctoral Committee:

Professor Kon-Well Wang, Chair
Professor Diann E. Brei
Professor Karl Grosh
Associate Professor Erik E. Nielsen

To my deceased grandmother Huiying and aunt Yuefen,

for their sacrificial care and support.

To my God the almighty,

for His sustaining love and inspiration.

"Be strong and courageous. Do not be afraid, do not be discouraged, for the LORD your God will be with you wherever you go." -- Joshua 1:9

Acknowledgement

First and foremost, I would like to express my special appreciation and thanks to my advisor Professor Kon-Well Wang, who have been a tremendous mentor for me throughout the years of graduate school. I would like to thank you for your support, encouragement, and challenges that allow me to mature as a research scientist. Your advice will be priceless even for my future research career.

I would like to thank my committee members: Professor Karl Grosh, Professor Diann Brei, and Professor Erik Nielsen, for your brilliant and insightful comments and suggestions. Thank you for enriching my research and letting my thesis defense an enjoyable experience. I would also thank the colleagues in my interdisciplinary research team: Professor Michael Mayer, Professor Chris Rahn, Professor Charles Bakis, Brandon Bruhn, Yazan Billeh, Chris Paran, Bin Zhu, Ben Wimmer and Aniruddh Vashisth, for all of your precious support and brilliant advices from different perspectives. Especially Ben and Aniruddh for fabricating the F^2MC samples and assisting some of my experiment efforts. Research collaboration with you all is a rewarding experience. Thanks to my friends at Pennsylvania State University: Deepak Trivedi and Amir Lotfi, for your inspirations at the very beginning of my graduate school.

Thanks to the National Science Foundation for the financial support, under the program of Emerging Frontier Research and Innovation (Award # 0937323)

A special thanks to my beautiful wife Ally, for your love and most precious support during the last stage of my graduate school. You are the new fountain of inspirations for my work and your encouragements bring me far. And I am grateful to my father Ming Li and mother Yuechun Zheng in China for your support and care, even from the other side of the planet.

Last but not least, thanks to my brothers and sisters in the family of Jesus Christ, the prayer, laugh, and life-sharing with you all transform the years of graduate school into a blessing journey of character building. Thanks to Bill Zienert my spiritual father; Brent Hoover, Manor Gist, Joe and Laura Sullivan, Steve and Jean Swisher, Dave Johnson, Benbo Song and Xuwei Wang, John Hui Wang, Qinyi Yan and Wei Gu, Yilun Wu and Qin Li, Wei Li and Sha Li, Liuliu Du, Zeyu Li, Fei Liu and Biyun Wu, Chirs Mann, Pastor David Chang and Wenliang Zhong, Ming'en Sheh and Lei Jin, Hui Liang and Kun Lou, Jin Yu, Hao Li, Lynn and Mary Degener, Rich and Jennifer Steiner, and my lovely landlord family Dave and Ginger Raymond.

Table of Contents

Dedication ii

Acknowledgement iii

List of Figures viii

List of Tables xi

List of Appendices xii

Abstract xiii

Chapter 1 Introduction 1

Chapter 2 Literature Review and Problem Statement 6

2.1 Review of adaptive structures with a cellular architecture 6

2.2 Review on previous research of F^2MC 8

2.3 Lessons from plant physiology studies 15

2.4 Problem statement 19

2.4.1 Insights on F^2MC cellular interaction 20

2.4.2 Structural integration and synthesis 21

2.5 Research objectives and approach 22

Chapter 3 Preliminary Study on a Dual F^2MC String Structure 26

3.1 Analytical model 26

3.1.1 F^2MC cellular analysis 26

3.1.2 Flow port dynamics 32
3.1.3 System governing equation 35
3.2 System function analysis 37
3.2.1 Experimental set up 37
3.2.1 Passive type of operation 40
3.2.3 Active function as an enhanced actuator 48
3.3 Summary 52
Chapter 4 Dual Cellular String Structure: Physical Insight and Synthesis 54
4.1 Non-dimensional model development 55
4.1.1 Non-dimensional F^2MC cellular model 56
4.1.2 Non-dimensional system governing equation 60
4.1.3 Experimental test 62
4.2 Physical insights 67
4.2.1 Physical meaning of the equivalent stiffness matrix 67
4.2.2 Correlating physical parameters to structural dynamics 70
4.3 Synthesize the cellular structure 71
4.3.1 Definition of the synthesis problem 71
4.3.2 Synthesis procedure 72
4.3.3 A synthesis case study 74
4.4 Summary 79
Chapter 5 Multi-cellular string structure synthesis 81
5.1 Multi-cellular structure analytical model 82
5.1.1 Performance of the individual cell 82

5.1.2 Principles of cellular interaction. 83

5.1.3 System level derivation. 84

5.1.4 Physical Insight of the stiffness matrix 87

5.2. Synthesis procedure for a prescribed spectral data 88

5.2.2 Implementing genetic algorithm. 90

5.2.3 Implementing JIEP Solver. 91

5.2.3 Synthesis results case study. 95

5.3 Summary 100

Chapter 6 Architectural Design and Comprehensive Synthesis 102

6.1 Architecture of the F^2MC based cellular structural unit 104

6.1.1 Mathematically defining the architectures 104

6.1.2 Governing equations and physical insight 109

6.1.3 Experiment test 113

6.2 Structure synthesis with multiple target functions 118

6.2.1 Derivation of the synthesis procedure 119

6.2.2 Synthesis case studies 123

6.3 Summary 128

Chapter 7 Concluding Remarks and Recommendation for Future Work 131

7.1 Concluding remarks 131

7.2 Recommendation for future work 136

Appendices 145

Reference 185

List of Figures

Figure 2.1 Construction of a single F^2MC cell 10

Figure 2.2 Functionality of a single F^2MC cell..... 12

Figure 2.3 F^2MC based dual functional structure 14

Figure 2.4 Variation of the plant cell wall micro-fibril orientation 17

Figure 2.5 A conceptual illustration of a hyper-cellular structure 22

Figure 3.1 Schematic diagram of the dual cellular "string" structure..... 27

Figure 3.2 Schematic layout of the interface between two adjacent F^2MC cells 33

Figure 3.3 Schematic illustration of the compatibility conditions between the two F^2MC cell for equations (3.28, 29). 36

Figure 3.4 The dual cellular test setup under passive type of operation..... 39

Figure 3.5 Variation of cell wall damping with respect to fiber angle 40

Figure 3.6 The variable stiffness of a dual cellular string structure..... 42

Figure 3.7 Vibration absorption performance of the F^2MC cellular structure..... 45

Figure 3.8 System response with different effective bulk modulus (B_f)..... 46

Figure 3.9 Poles and zeros position with different fiber angle combinations..... 46

Figure 3.10 Poles and zeros position with different fiber angle combinations..... 47

Figure 3.11 Poles and zeros position moves as the flow-port length changes..... 47

Figure 3.12 Actuation performance of a single and dual cell structure 50

Figure 3.13 Effects of flow port length on the power density improvement 51

Figure 3.14 Effects of effective fluid bulk modulus 51

Figure 4.1 A schematic diagram of the construction of F^2MC cells with three important design variable group 58

Figure 4.2 Performance parametric space Ω 60

Figure 4.3 Experiment set up to measure the performance parameter β 64

Figure 4.4 Experiment set up to measure δ and α 65

Figure 4.5 Measured dual cellular structure system poles and zero positions matches well with prediction 67

Figure 4.6 Flow chart for the synthesis procedure 73

Figure 4.7 Illustration of step 5 in the synthesis flow chart 74

Figure 4.8 Synthesis results for cell #1 75

Figure 4.9 Synthesis results for cell #2 76

Figure 4.10 Synthesis results for cell #1 in terms of physical design variables 77

Figure 4.11 The achievable pole positions with different zero target 78

Figure 5.1 Illustration of the multi-cellular string structure. 83

Figure 5.2 Logic flows of the proposed hybrid synthesis procedure 90

Figure 5.3 Illustration of a mass spring-oscillator series 92

Figure 5.4 JIEP solver integrated with Householder tri-diagonalization 94

Figure 5.5 Achievable poles and zeros from a triple cell string structure 98

Figure 5.6 The histogram plot of the cellular synthesis results for a specific set of prescribed spectral data 99

Figure 6.1 Free body diagram of an individual F^2MC cell within the structure 105

Figure 6.2 Admissible constraints onto each type of state variables 107

Figure 6.3 Architectures of the cellular structure 108

Figure 6.4 Three different designs based on (AD) type of architrave 109

Figure 6.5 (AD) and (BD) linkage mechanism set up 114

Figure 6.6 Test results for (AD) architecture 117

Figure 6.7 Test results for (BD) architecture 117

Figure 6.8 Test results for (BC) architecture 118

Figure 6.9 The logic flow of the comprehensive synthesis procedure 122

Figure 6.10 A sample synthesis result for cell #1 125

Figure 6.11 Combination of variable stiffness and actuation authority based on the same spectral data target 127

Figure 6.12 Heat map summarizing the results of a performance survey 128

Figure 6.13 Illustration of extending the dual cellular unit into a larger scale structure 129

List of Tables

Table 3.1 Material and design parameters of the dual cell structure test 39

Table 3.2 Parameters of the sample F^2MC cells 40

Table 4.1 Some F^2MC sample design parameters and experiment setup 66

Table 4.2 The measured constitutive parameters and their corresponding prediction 66

Table 4.3 Several parameters in the synthesis case study. 75

Table 4.4 Two sample synthesis results. 75

Table 5.1 Sample synthesis results 97

Table 6.1 Derivation of K_{ij} in the system governing equations. 111

Table 6.2 The properties of the F^2MC cell samples 116

Table 6.3 Parameters for the synthesis case study 124

List of Appendices

Appendix A Derivation of A, B, C, and D in (3.19 and 20)..... 145

Appendix B Uniform Pressure Assumption in a Single F^2MC Cell..... 139

Appendix C Effects of Flow Port Intrusion into F^2MC Cell 146

Appendix D Measure the Constitutive Parameters of F^2MC Cell 148

Appendix E MATLAB Script of the Multiple Cellular Structure Synthesis..... 150

Appendix F Closed Form Relationships between the Constitutive Parameters of the Two F^2MC Cells in Four Unique Architectures..... 170

Appendix G MATLAB Script of the Comprehensive Synthesis Procedure..... 172

Abstract

Plants have many attractive characteristics for developing multi-functional adaptive structures, such as high strength and toughness per unit density, self-healing and reconfiguration, and nastic motion with short response time and large deformation. The vision of this thesis research is to develop enabling knowledgebase and design methodologies to synthesize plant-inspired adaptive structures. More specifically, investigations will focus on achieving multiple mechanical functionalities concurrently, such as actuation, variable mechanical properties, and vibration control. To reach this vision, this thesis research adopts the concept of multi-cellular structure based on the fluidic flexible matrix composite (F^2MC) cells. Because such concept offers a natural platform to incorporate design inspirations from plants into artificial adaptive structure study, both at the local level of individual cell development and at the global level of structure architectural design and synthesis.

This thesis research identifies several critical issues related to the development of F^2MC based cellular adaptive structure. It investigates the dynamic characteristics of a multi-cellular structure, where F^2MC cells with different configurations are connected to each other not only mechanically but also fluidically. It discovers new dynamic functionalities that are not feasible in an individual cell, including vibration isolation and dynamic actuation with enhanced authority within a designated frequency band. It provides a list of

unique architectural designs of the cellular structure based on rigorous mathematical principles, and compares their performance to gain design insights. Finally, it derives novel and comprehensive synthesis procedures that are capable of selecting appropriate design variables for the F^2MC cells, so that the cellular structure can achieve multiple performance targets concurrently, such as desired variable stiffness, actuation authority, and spectral data.

The plant inspired design principles, physical knowledgebase and synthesis methodologies developed from this thesis fully manifests the rich functionalities and design versatilities of the F^2MC based multi-cellular structure. They could foster the adoption of such novel adaptive structure concept to advance the state of art of many engineering applications, including aviation and aerospace, soft robotics, and intelligent civil infrastructure. The biologically inspired, multiple-cell oriented approach towards developing adaptive structure could also create a paradigm shift in other related academic research.

Chapter 1
Introduction

The field of adaptive structures (also referred to as smart structures or intelligent structures) has been an active research field for the past several decades (Wagg et al. 2008). The vision is to eventually create autonomous structures capable of altering their configuration, behavior, and properties, so that they can achieve desired functions or respond to changes in environment. In recent years, the research works in adaptive structures have developed into a richly diverse inter-disciplinary topic involving material science, electronics and transducers, solid mechanics, structural dynamics and controls, and even biological systems. One promising trend in this field is to seek inspirations from nature. While many novel biologically inspired adaptive structure concepts have been proposed, most of them focused on exploiting the knowledge from the animal kingdom. Relatively speaking, little research work has been performed on plant-inspired adaptive structures, despite of the fact that plants have many attractive characteristics for such purpose. For example, mature wood tissues are known for their excellent combination of strength, stiffness, and toughness per unit density. These tissues are organized to form tree trunk and branches with an optimized geometric shape so that any stress concentrations induced by self-weight, external load and injuries are minimized. These characteristics can be translated, in engineering terms, as efficient, lightweight, and high strength structural designs. Plants can also sense

external damages, heal themselves, and grow according to the environmental constraints; and this can be translated as the self-healing and self-reconfiguration in engineering systems. Furthermore, several plant species, such as *Mimosa Pudica*, are capable of rapid nastic motions at the macroscopic level (Burgert and Fratzl 2009) via microscopic cellular deformations. When Mimosa is stimulated, its leaves would fold up, and branches bend down as a self-defense mechanism. This kind of reversible motion can be translated as an actuation with a large stroke and block force yet in a short response time (Balmer and Franks 1975, Volkov et al. 2010a, Volkov et al. 2010b). All of the aforementioned characteristics are ideal functions that many adaptive structure researchers have tried to achieve. While animal tissue and organs exhibit some similar characteristics as well, plants achieve these concurrently with limited resources. Moreover, these characteristics can vary significantly over time and location in a single plant as dictated by global and local stimuli (Niklas, 1992). Therefore, plants have much to offer in terms of basic material development, structural architecture design, and actuation/sensing approaches that could cause a significant technology leap for future multi-functional adaptive structures.

Based on the arguments above, the vision of this thesis research is to develop enabling knowledgebase and design methodologies to synthesize plant-inspired adaptive structures. More specifically, investigations will focus on several mechanical functionalities, including actuation/morphing, variable mechanical properties, and vibration control. These functions should be achieved *concurrently* in one integrated system just like plants, because concurrent multi-functionality offers wide advantages in applications with a strict space and weight constraint. To achieve this aim, we propose adopting a *cellular structure* approach inspired by the nastic plant cellular architecture and functions as described above.

A cellular structure consists of a network of "cells" or basic structural elements, where each individual cell is capable of some simple functions by its own, yet integrating them together could extend their capabilities to a new level. This approach is a "bottom-up" process: the properties and behaviors of the individual cell are studied in priori; then the overall structural performance is an assembly or extension from the individual cells. Such approach offers a greater freedom to tailor structural characteristics as compared to the more conventional "bulk material" approach.

Furthermore, the cellular structure approach offers two unique aspects through which inspirations from the plant kingdom can be applied to advance the state of art. The first aspect is the design of the individual cell. A single plant cell by itself is already an engineering marvel, and its unique properties and behaviors are directly related to some of the aforementioned attractive characteristics. Therefore, the anatomy of individual plant cell is a rich source of engineering design inspirations. In this thesis research, the specific artificial "cell" we utilize and build upon is the fluidic flexible matrix composite cell (F^2MC for short). F^2MC is a fruit of biomimicry of plant motor cell; it emulates the plant cell wall fibrillar organization and the internal turgor pressure dynamics. After almost a decade of development, the artificial F^2MC cell has successfully demonstrated mechanical functions similar to the plant motor cell, even functions not seen in plants. Therefore, F^2MC is a solid foundation for developing more capable cellular structures. More details about the biological inspiration for the F^2MC development are discussed in the following chapter (section 2.2).

Once F^2MC is chosen as the basic structural element, the next challenge arises naturally: effective methodologies to design and assemble the F^2MC together to form a structure with compelling performance. This leads to the second aspect through which one can learn from plants: structural architecture and synthesis. Physiology study revealed many principles on how plants maximize the potential of their cells, and many of the principles can be applied to tackle the synthesis challenge. For example, differentiation is widely observed in the plant kingdom. The variation of the cell wall cellulose micro-fibril orientations among adjacent cells is directly related to the excellent combination of strength and stiffness of a tree branch (Fratzl 2003). This principle can be applied to the artificial structure by allowing F^2MC cells to differ from each other, so that the interaction between cells can be exploited for new type of functions. A list of design principles employed in this research is discussed in detail in the following chapter as well (section 2.3).

In summary, the F^2MC based cellular structure approach offers a solid platform on which one can apply lessons from plants to advance the state of art of adaptive multi-functional structure. This thesis research is novel and unique because, for the first time, it systematically incorporates *both* the aspects of local cellular design and global structure synthesis based on F^2MC composites. It provides knowledgebase and design tools to develop F^2MC based cellular structure that can concurrently achieve the targeted functions of actuations, variable mechanical properties and vibration control. The outcome of this thesis research can facilitate the adoption of F^2MC based cellular structure concept to a variety of engineering applications such as airframe morphing, soft robot, and intelligent civil infrastructure. Furthermore, even though this thesis is tailored specifically for F^2MC based structure, its lessons and experiences could trigger a paradigm shift in the field of

adaptive structure in general, and foster a new generation of cellular adaptive structure across different physical disciplines.

Chapter 2
Literature Review and Problem Statement

This chapter first reviews the current state of art of the cellular adaptive structure research in general; then discusses the previous research on F^2MC in detail, covering the development of individual F^2MC cell inspired by plant cell anatomy and some earlier attempts on multi-cellular structure. Critical research issues are identified. To address these issues, this chapter turns its focus into plant physiology studies again to search for lessons and guidelines, based on which research problem statements and objectives are defined. Finally, the overall research approach of this thesis is laid out. Section 2 of this chapter discusses the inspirations from plants through the aspects of local individual cell design; while section 3 of this chapter discuss the inspirations through the aspects of global structural architecture and synthesis.

2.1 Review of adaptive structures with a cellular architecture

The cellular adaptive structure approach itself is not new, as there are several concepts in this category in active investigation. They operate across a wide range of physical disciplines; yet they are all essentially assemblies of many structural elements or cells. These cells are usually arranged in a periodic pattern; they can perform some simple mechanical

functions individually; and combining them tougher can extend the overall structural performance to a new level. In the following, various cellular adaptive structure concepts are categorized and reviewed based on their functionalities.

Actuation/shape morphing: This is the most common type of cellular adaptive structures because of its potential in morphing applications in aviation and aerospace. For example, Pagitz et al. (2012) connected prismatic cells with tailored pentagonal or hexagonal geometry to form a leading edge of the airplane wing. When these cells are pressurized, the whole structure morphs between designated target shapes with geometric accuracy to maintain aerodynamic efficiency. Ramrakhyani et al. (2005) used tendon-activated compliant cellular trusses to construct a lattice structure for continuous shape change. Ueda et al. (2010) connected a series of piezoelectric stack actuators with a nested cellular architecture to amplify their effective strains, creating a linear actuator that combines both large stroke and large operating frequency bandwidth. More examples in this category can be found in Pagtiz and Bold (2013), Vasista and Tong (2012), Vos et al. (2011), and Luo and Tong (2013a and 2013b).

Variable mechanical properties: Changing mechanical property, such as stiffness, of a specific group of cells can give the whole structure highly tunable characteristics. For example, Puttmann et al. (2012) applied multi-state polymer infills into a traditional honeycomb core to form a semi-active panel. By switching the infill stiffness in the designated honeycomb cell between "rigid" and "soft" states, the overall in-plane stiffness profile of the panel becomes anisotropic and tunable with a large degree of freedom.

Unique load bearing capacity: Different cells can have different "specialties" in load bearing capacity, and assembling these cells together can result in a structure with

unique properties unseen from conventional materials. For example, Pontecorvo et al. (2012) proposed adding various internal features, such as contact elements, buckling beams, and dashpots into honeycomb core so that the whole panel exhibits some unique combinations of both high stiffness and high damping properties. And Schenk and Guest (2013) molded several layers of Miura sheets together to form a cellular "meta-structure" with different Poisson's ratio related to in-plane expansion and out-of-plant bending.

The aforementioned examples are not intended to be an exhaustive review on cellular adaptive structure, but rather, they illustrate the promising potentials and rich research opportunities in this subject. Compared to these cellular structure concepts, a significant uniqueness of the F^2MC based cellular structure is its multi-functional capability even on the individual cell level. The following section shall give a detailed review on the previous work on F^2MC.

2.2 Review on previous research of F^2MC

As mentioned earlier, F^2MC was developed by emulating one of the most distinctive features of the plant motor cell wall: fibrous organization. A mature cell wall usually consists of several layers of cellulose micro-fibrils that are cross-linked together by polysaccharides such as pectin and hemicelluloses (Cosgrove 2005). These micro-fibrils could orient randomly in the cell wall to act like structural reinforcements, similar to the short fiber reinforced composite seen in some engineering applications. In certain scenarios, however, these micro-fibrils arrange themselves into a helix pattern with a relatively uniform orientation, giving the cell wall anisotropic elasticity. This anisotropy, combining with the variation of internal turgor pressure, plays a vital role in some cellular functions

such as elastic osmotic swelling/shrinking, or plastic elongation. For example, there are evidences showing that the reversible bending motion of the guard cells in plant leaves is related to this cellulose micro-fibril distribution in the cell wall.

An F^2MC cell can be illustrated as a fiber composite tube filled with pressurized working fluid as shown in figure 2.1. The stiff fibers, winded in double helix pattern, are embedded into a soft matrix resin at a prescribed angle, resembling the micro-fibrils in the plant cell wall. Inner liner is included for sealing purpose if necessary. The F^2MC tube is fabricated by the filament winding procedure. In this procedure, a carriage applies wet carbon fiber strip onto a spinning mandrel to form the cell wall. The carriage moves along the mandrel axial direction at a customized speed, so that the fiber strip can be laid at a desired angle.

Because of the fibrous organization, the F^2MC cell wall is elastically anisotropic similar to the plant cell wall. This anisotropy, combined with the working fluid bulk modulus and pressure, gives a single F^2MC cell different cellular functions under different operating conditions. The work of Philen et al. (2007) and Shan et al. (2006) demonstrated that the F^2MC cell acts as an *active* device/actuator with large stroke and block force when fluids are pumped in. The stiff reinforcing fibers restrict the deformation of the pressurized F^2MC cell, and transform the internal pressure into axial pulling/pushing force. The cell will contract under internal fluid pressure increase if the fiber angle is less than ±55°, extend if the angle is greater than ±55° (figure 2.2b), such actuation mechanism closely resembles the elastic motor cell swelling/shrinking process.

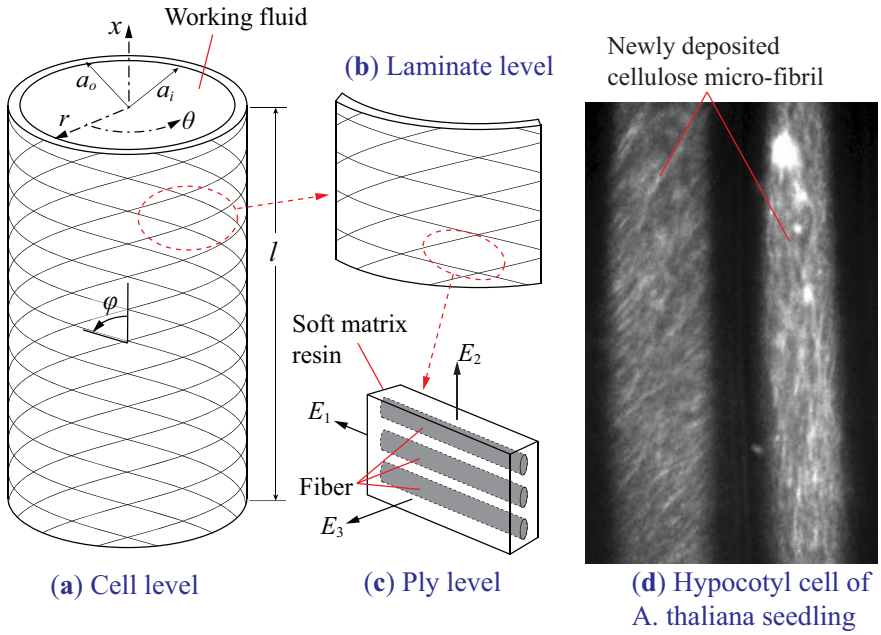

Figure 2.1 Construction of a single F^{2}MC cell. From (**a**) cell level, to the (**b**) laminate level, to the (**c**) ply level. Comparing to the confocal microscopic image of the plant cell wall (**d**), one can see the similar fibrillar organizations between the plant cell and the F^{2}MC cell [1].

In the active actuation operation, the F^{2}MC cell has some similarities to another type of elastic linear actuator called pneumatic artificial muscle (also called "McKibben actuator" or simply "PAM"). A typical McKibben actuator is made by inserting a rubber tube (bladder) into a braided fiber sleeve, and linear actuation is also achieved by internal pressurization, usually though pneumatic system. Many research were devoted to the modeling and controlling of the McKibben actuator, and it had already been adopted in various

[1] Strictly speaking, the fibrillar feature in the confocal microscopic image is not the image of the cellulose micro-fibril themselves, but rather the movement of the proteins that synthesis the fibril. It is a good representation of the orientation of the newly deposited fibril in the inner layer of the cell wall. The credit of the confocal microscopic images in figure 2.1 and 2.4 belong to Chris W. Paran, Dr. Feng Guo and Dr. Erik E. Nielsen at the Department of Molecular, Cellular and Developmental Biology at the University of Michigan.

industrial and medical robotic applications. Interested readers can refer to Chou and Hannaford (1996), Tondu and Lopez (2000), and Zhang and Philen (2012) for a comprehensive review on its development. The F^2MC, on the other hand, has several distinctive features compared to McKibben actuator. First, F^2MC can be fabricated with precision control on fiber angles to provide different type of actuation motions (contraction, extension; or twisting if there is only one helix fiber layer instead of two), while a typical McKibben actuator can only achieve contraction. Secondly, the reinforcing fiber of the F^2MC is imbedded into soft resin while McKibben has two separate layers of internal rubber bladder and external braided sleeve. The integrative construction of F^2MC can minimize the friction between the fibers to achieve a better actuation performance.

Another distinctive feature of F^2MC cell is its multi-functionality. While McKibben is developed solely for actuation purpose, F^2MC can also act as a variable stiffness element with simple on-off valve control (Shan et al. 2008). This is under adaptive-passive or semi-active type of operation condition where external pumping is removed. For certain fiber angles, the F^2MC cell has a low axial stiffness and high axial extensibility with open valves at both ends of the cell. When the valves are closed, the cell becomes significantly stiffer in its axial direction because the confined working fluid resists the volume change induced by the deformed fiber composite cell wall (figure 2.2c). A closed/open stiffness ratio of 56 was achieved in laboratory tests (Shan et al. 2008). Analysis showed that F^2MC cells could achieve a large range of combination between stiffness ratio and absolute open valve stiffness value.

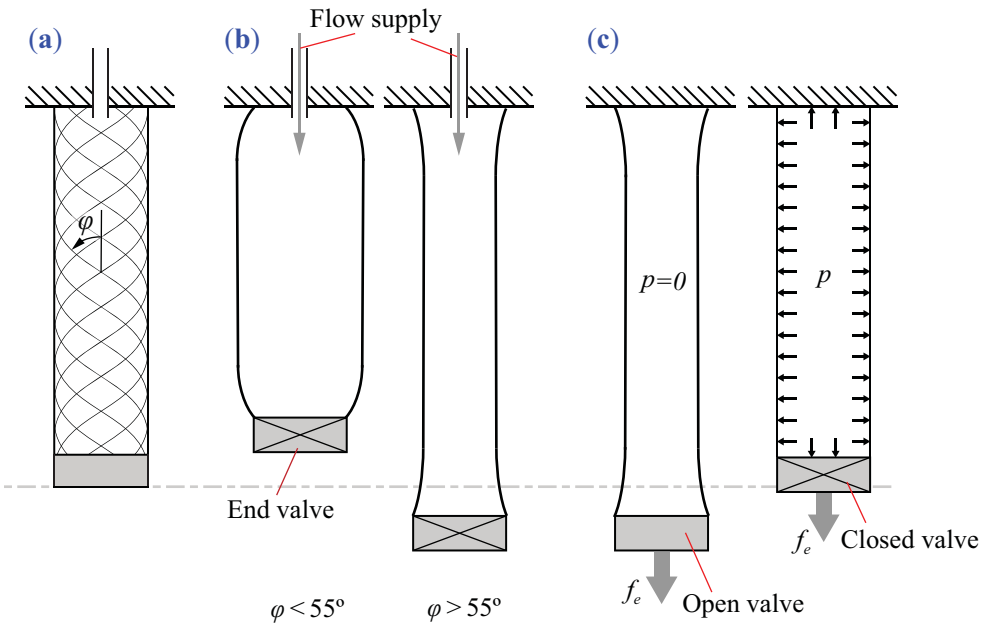

Figure 2.2 Functionality of a single F^{2}MC cell. **a**) Neutral state; **b**) active actuation; **c**) passive variable stiffness.

Multiple F^{2}MC cells can be grouped together to form simple cellular structures in order to expand the aforementioned functions of an individual cell. For example, for active actuation, two layers of parallel F^{2}MC cells were molded into a panel, and by applying pressure to different cells, this panel can provide complicated in-plane bending, out-of plane bending, and twisting actuation motions (Li and Wang. 2012). Regarding adaptive-passive type of operation, three layers of F^{2}MC cells spanning at 60 degree angles with respect to each other were molded together to form a panel, and by on/off valve control on different layers of cells, it can provide a tunable in-plane anisotropic variable stiffness (Shan et al. 2008).

The F^{2}MC cells can also be integrated with other types of structural elements. For example, a F^{2}MC cell was integrated with a honeycomb core to form a sandwich panel (Li

et al. 2008, figure 2.3). The honeycomb core is soft against bending but stiff against shear, so the transverse load on the sandwich panel was translated into the longitudinal load onto the F^2MC cell. As a result, the variable stiffness of the F^2MC cell in its longitudinal direction is transformed into a variable stiffness of the panel in its transverse direction. Analysis showed that a honeycomb sandwich panel with a single F^2MC cell as its face sheet could provide a high/low stiffness ratio of up to four, while multiple F^2MC cells connected in series could further increase this ratio (Li et al. 2008). To illustrate the potential of integrating the actuation and variable stiffness functionalities into one compact system, the F^2MC-honeycomb structure was connected to a piezoelectric-hydraulic pump (PHP) which can exercise both valve control and supply pressurization, making it dual functional (figure 2.3, Kim et al. 2010).

A series of efforts were carried out to explore potential applications for F^2MC featured adaptive structure other than actuation and variable stiffness. One of the promising applications is vibration control. So far, two approaches had been investigated for this purpose. One was to exploit the variable stiffness function by connecting the cell to a fast open/closing solenoid valve, the stiffness of the F^2MC cell can be switched between high/low state to reduce or isolate the vibrations applied onto the cell (Lotfi et al. 2012 and Philen 2012a). The other approach was to connect the cell (in open valve state) to an external flow port, so that the port inertance acted like a sacrificial mass in a vibration absorber (Scarborough et al. 2012). Other applications were also explored such as force tracking control (Philen 2012b), or variable impedance material for prosthetic devices (Philen 2009); these two applications were still based on the variable stiffness function of a single F^2MC cell.

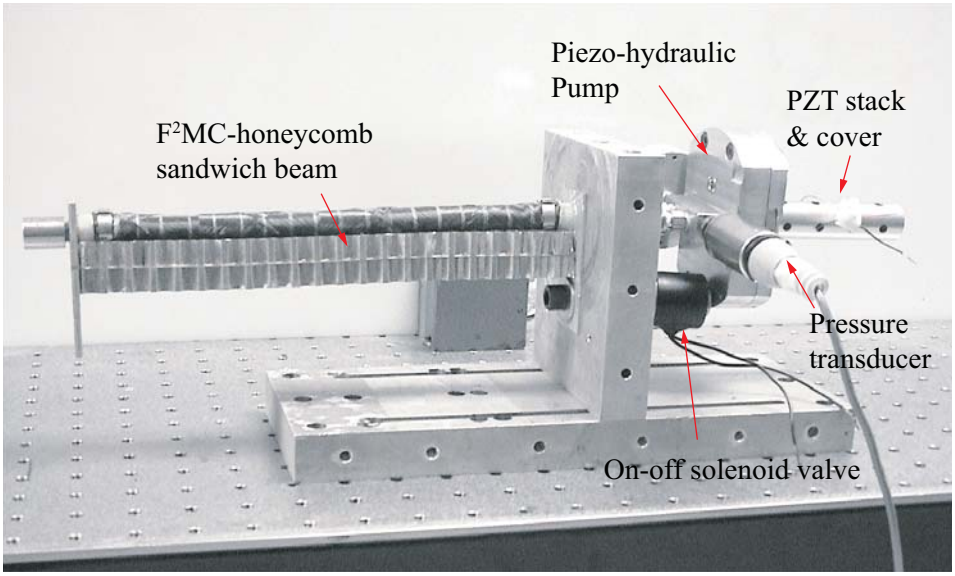

Figure 2.3 F²MC based dual functional structure (Kim et al. 2010). An F²MC-honeycomb sandwich beam is integrated with a piezoelectric-hydraulic pump, which can provide us with both actuation and variable transverse stiffness in one compact system.

As can be concluded from these previous works on F²MC, the physical properties and behaviors of an individual F²MC cell were extensively studied and well understood. And even some F²MC based multi-cellular structural concepts were explored. However, these early attempts on cellular structure were far from systematic, because they mostly focued on extending one specific type of function, and serve only for a proof-of-concept purpose. To systematically develop the F²MC based multi-cellular structure for its potential of achieving concurrent multi-functionality, several critical questions need to be answered, such as:

i) Are there any new functions from multi-cellular structures that are not feasible from a single cell? Because all of the previous attempts on

F^2MC based cellular structure focused on extending the functions that are already known from a single cell.

ii) What are the unique architectures by which F^2MC cells can be assembled together to achieve multi-functionality? In the previous work, F^2MC cells were simply laid out in parallel and molded into a rubber-based panel, and each cell are controlled separately without any direct interaction.

iii) How to design each individual cell so that the overall structural performance can be optimized? In the previous work, all of the F^2MC cells were assumed identical, which negated the advantage of design versatility of individual cell.

To answer these questions, deeper physical insights, new methodologies and robust synthesis procedures are necessary, so we turn to plants for inspirations and guidelines for structural architecture and synthesis. The following section shall review the lessons we learned from plant physiology studies.

2.3 Lessons from plant physiology studies

Extensive physiology research revealed numerous design and synthesis principles behind those attractive characteristics in plants as mentioned in the introduction, and many of these principles are applicable to advance the development of artificial cellular structures.

The advantage of multiple cells: Some of the rapid motion in plant world is not physically possible without a large number of small cells. For example, mimosa pulvinus, the organ responsible of the fast leave-folding motion, consists of a large number of small motor cells. These motor cells activate the folding motion by osmotic swelling or shrinking

(Burgert and Fratzl, 2009; Martone et al. 2010). Osmosis itself is a relatively slow process; however, the small motor cell size guarantees a large surface-to-volume ratio to overcome this limitation. Moreover, if the response time and deformation requirement exceed the physical limit of osmotic process, elastic bi-stability or "snap-through" behavior is introduced to further increase the nastic motion speed, the best know example of this is the venus flytrap (Skotheim 2005; Dumais and Forterre 2012). Such kind of bi-stability, as argued by the work of Pagtiz and Bold (2013), can be achieved naturally from a cellular structural organization. On top of fast response time, a cellular layout is also beneficial for structural maintaining high strength per unit density.

Therefore, understanding the advantage of multiple cells is crucial for developing artificial cellular structure, because some functions might be feasible only with multiple F^2MC cells. This requires a deep understanding in physics behind cellular interaction.

Differentiation in the cell wall fibrous organization: As mentioned earlier, one of the most distinctive features of the plant cell wall is its fibrous organization. And the differentiation of this fibrous organization, both within one plant cell or between adjacent cells, plays a vital role in some plant functions.

For example, the orientation of the micro-fibril has a strong linkage to the rate and direction of fast cell expansion and growth. Different from the nastic motion, the rapid cell growth is initiated by plastic "loosening" of the cell wall while the internal turgor pressure is hold unchanged. Yet, the stiff cellulose micro-fibrils can still constrain the direction of wall expansion if they are organized at a uniform orientation. It was argued that at different stages of the rapid cell elongation, the micro-fibril orientation will adjust accordingly to

control the elongation rate (Richmond et al. 1980, Baskin 2005, and Cosgrove 2005, Anderson et al. 2010). Figure 2.4 presents an illustrative example of the dynamic changes of fibril orientation in the elongating hypocotyl cell.

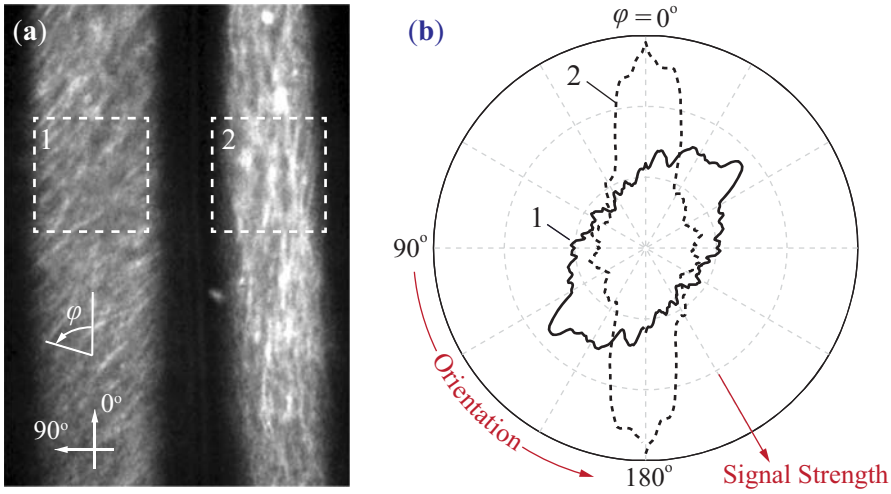

Figure 2.4 Variation of the plant cell wall micro-fibril orientation. (**a**) The confocal microscope image shows two adjacent hypocotyl cells in an *A. thaliana seedling*. A Fast Fourier Transformation (FFT) script is applied to the two sample areas (the two white boxes) to calculate the net fibril orientation. (**b**) The FFT results, where the peak in the curve represents the dominant fibril orientation in the corresponding sample area. One can clearly see the orientation difference between the two cells, where cell #1 has a fibril orientation at around 130°; cell #2 around 0° [1].

Another example, since the relatively stiff cellulose micro-fibril provides highly anisotropic elastic properties, differentiation of micro-fibril orientations can give an optimized structural performance. The cylindrical shaped plant cell with the micro-fibril oriented close to its longitudinal axis has a relatively higher longitudinal stiffness, so that it is capable of withstanding large tensional loads. On the other hand, cell with fibril perpendicular to its longitudinal axis is better suited for compression load (Cave and Hutt 1968).

In tree branches, the orientation of the micro-fibril varies between cells at different locations in order to optimize the balance between the branch load bearing capacity and its flexibility (Fratzl 2003, and Fratzl et al. 2004).

The differentiation of cellulose micro-fibro orientation also enables some plants nastic motion without any energy cost (Stahlberg and Taya 2006). The most impressive example is probably the wheat awn in the seed disposal unit (Fratzl et al 2008; and Elbaum et al. 2011). The cellulose fibrils in the cap and ridge side of wheat awn have different orientations, which cause the awn to bend with changing humidity. As a result, the awn can propel the seed deeper into soil with the help of the high-low air humidity cycle between nighttime and daytime. Another similar example is the opening and closing of pinecone (Dawson et al. 1997).

The principle of differentiation observed in plants suggests that the F^2MC cells can be different from each other in the same structure. This could bring in richer cellular interactions that can be exploited for our benefits. On the other hand, rigorous synthesis procedure is necessary to manage the large number of design variables in the system once the cell can differ from each other.

Hydraulic network and fluidic properties: Plants, especially the higher vascular species, are essentially hydraulic machines. The change of internal turgor pressure is the activating mechanism of the many nastic motions, such as mimosa pudica, venus flytrap, and ice-plant seed capsules (Hill and Findlay 2009; Volkov et al. 2010a and 2010b; Forterre et al. 2005; and Harrington et al. 2011). There are also evidences that the internal turgor pressure, together with the micro-fibril can provide pre-tension stress to the tree trunk to better withstand external load. Other than turgor pressure, the vascular plants also have a

complex fluidic network (xylem and phloem) to transport water and nutrients throughout the plant body, enabling the plants to grow into a larger size.

Other than pressure, plants also exploit different types of fluid properties. An impressive example is the catapult mechanism of distributing fern spore (Burgert and Fratzl, 2009), which is achieved by the water cohesion force in a ring of small annular cells. During this catapult process, there is an intricate balance between the cohesion force and the cell wall spring force in a tug-of-war style. When this balance reaches a threshold level, the stored elastic deformation energy is released rapidly to catapult the spores over a large distance.

In the previous artificial cellular structure research, most attention is focused on pressure related applications, and the cells are not fluidically connected to each other. Therefore, it is worthwhile to investigate the potential from connecting different cells together through fluidic network, so that other fluid properties such inertia and viscosity can be exploited for new types of structural functions.

2.4 Problem statement

Based on the critical issues raised in the F^2MC based cellular structure development (section 2.2) and the inspirations from plants (section 2.3), several technical problems are identified for this thesis work. Addressing these problems successfully can significantly advance the state of art in this research field.

2.4.1 Insights on F^2MC cellular interaction

Understand cellular interaction through fluidics: In the previously reviewed simple multi-cellular structures (Li and Wang 2012; Shan et al. 2008), the F^2MC cells are simply molded into an elastomer matrix, so they interact with each other only through transferring mechanical stress. However, F^2MC cell operates based on both mechanical and hydraulic principles, so adding a fluidic link between cells could be beneficial. If the F^2MC cells are connected through fluid circuits, the fluid inertia, viscosity and bulk modulus could be exploited to develop new type of functions. Moreover, fluid circuits can assist transporting chemicals for non-mechanical adaptive functions such as self-healing.

Explore the advantages of varying cellular configuration: Cell wall fiber orientation is one of the most important physical variables of F^2MC because it determines the orientation of anisotropy. The previously reviewed F^2MC cellular structure assume the same fiber orientation among all cells, however, the distribution of plant cell wall microfibril orientation is much more complicated as discussed earlier. This raises the topic of how the structural behavior would change if the F^2MC cells have different fiber orientations. It is particularly interesting when the cells are connected through a fluid circuit, because the difference between F^2MC cells will generate a pressure gradient and induce internal pulsate fluid flows under dynamic loading.

It is worth noting that other than the variation of fiber orientation, the variation of other cell wall properties between different cells, such as wall thickness, anisotropic elasticity are also subjects of interests in this thesis work.

Investigate dynamic characteristics: Many cellular-based adaptive structure functions require the understanding of the dynamic characteristics of the cellular elements.

Several studies reviewed earlier in this chapter have initiated the investigations on this topic, however most research to date are based on the principles and knowledge developed from static operations. It is thus necessary to investigate the system dynamics in order to search for functions that would otherwise not be feasible in the static regime.

2.4.2 Structural integration and synthesis

Discover unique structural architecture: Plant cells have unique ways to spatially distribute and connect themselves together, enabling a diverse structure performance to adapt to their changing environment. When integrating multiple F^2MC cells, it is also important to survey the unique architectures by which the cell can be kinematically and fluidically connected together to achieve various target performance.

Derive robust synthesis procedure: Synthesizing a cellular structure is very challenging because of the large number of design variables involved, especially when the cells can be different from each other. Plant structure is efficient in this aspect because it can maximize the potential of each individual plant cells through selective growth, turgor pressure distribution, and cell reconfiguration. For the artificial cellular structure, synthesis procedures need to be developed in order to maximize the potential of individual F^2MC cells as well. Such procedures should incorporate the knowledge on individual cells and the insights on cellular interactions, so that it can assign appropriate values to the large number of design variables to achieve a set of performance targets.

2.5 Research objectives and approach

To address the problem statements from the previous section, this thesis research proposes to investigate the dynamic characteristics and the application potentials of F^2MC based multi-cellular structures. It will rigorously analyze the fluidic interactions between cells with varying configurations; gain good insight on the system behavior; survey unique structural architectural designs, and then develop systematic methodologies to synthesize and optimize such advanced structural system. The outcome of this research would be the building blocks towards synthesizing "hyper-cellular structures" with a large number of F^2MC cells (figure 2.5), and such structure could be capable of performing different types of functions simultaneously by controlling different cells strategically.

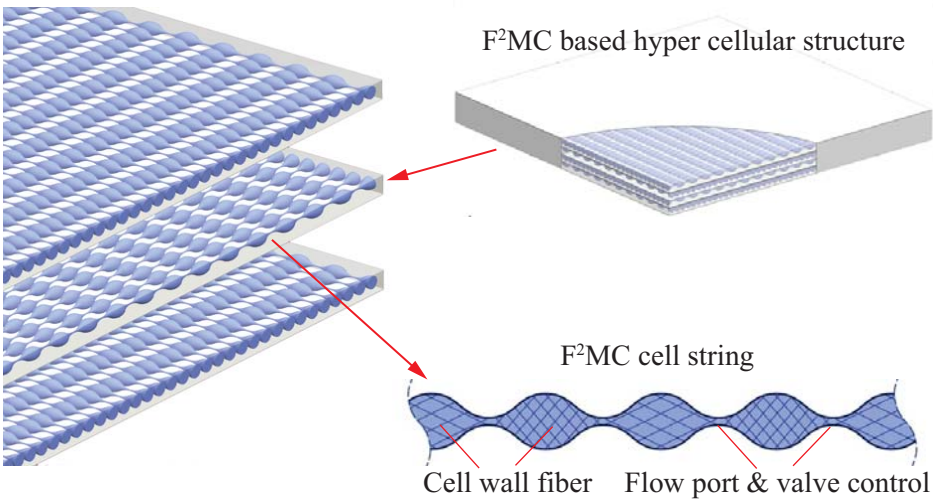

Figure 2.5 A conceptual illustration of a hyper-cellular structure. It consists of a large number of F^2MC cells of different configurations, so that multiple functions can be achieved concurrently by activating and controlling different group of cells strategically.

In order to gain a basic understanding on the F^2MC based cellular structural behavior, the thesis research first investigates the dynamic characteristics and functions of a dual-cellular "string" structure with two F^2MC cells with different fiber orientations (chapter 3). An analytical model is developed, which incorporates the performance of the individual F^2MC cell, as well as the dynamics of the end mass and flow port inertia. Experimental efforts are carried out in parallel. As a result of this preliminary investigation, two new dynamic functions are discussed; they are 1) vibration absorption and 2) dynamic actuation with an enhanced authority in a designated frequency band. This significantly enriches the list of functions that the F^2MC based cellular structure can offer. The knowledge and experiences from this preliminary investigation become the basis of the thesis research.

Chapter 4 furthers the analysis on the dual-cellular "string" structures in order to obtain deeper physical insight, and to lay down the basics for structure synthesis. A non-dimensional dynamic model is developed based on the preliminary version discussed in chapter 3. This model reveals the missing linkage between individual cell performance and structural dynamics as a whole. It also defines a set of non-dimensional *performance parameters* that describes the performance of an individual F^2MC cell; working with these parameters can significantly simplify the math derivation. Experimental effort is carried out to test the derivation of these parameters. A synthesis tool for the dual cell string is then derived based on the non-dimensional model, where the system poles and zeros positions are the performance target. Synthesis case studies in this chapter demonstrate the strong design versatility of F^2MC based cellular structure, which are exploited in more

sophisticated synthesis in the following chapters. And the concept of performance parameters also becomes a useful tool to mathematically simplify the research work presented in the following chapters.

In Chapter 5, the synthesis effort is attempted on a multi-cellular "string" structure with at least three F^2MC cells connected by an internal fluid circuit. The system poles and zeros positions are again the synthesis target, since they are closely related to the dynamic functions. The mathematical problem behind multiple-cell synthesis is fundamentally different from the dual cell synthesis and more challenging, thus a brand new procedure is required. This new procedure relies on the generalized dynamic model, which is applicable to a string structure with any number of cells; and it attempts to tackle the complexity of the problem by integrating two ingredients together: one is genetic algorithm with discrete variables, and the other is the Jacobi inverse eigenvalue problem solver (JIEP). Such hybrid procedure should be computationally more efficient compared to brute force optimization iteration. Case studies demonstrate that the proposed hybrid synthesis procedure is successful for a string structure with three different F^2MC cells. And the design versatility of the triple cellular structure is again illustrated by the large range of achievable spectral data targets. On the other hand, the hybrid synthesis procedure fails to converge to feasible designs when the cell number exceeds three due to numerical complexities. Nevertheless, such efforts and findings would pave the path for future research on multi-cell synthesis.

Chapter 6 consolidates the experiences and lessons from the previous chapters and focuses on exploiting the full potential of an F^2MC based dual cellular structure in order to fully address the thesis problem statements. This chapter includes two sections: the first is on the architecture design of a dual-cell structural unit, and surveys the unique ways to

fluidically and kinematically connect the two cells together to achieve multiple functions. Four types of architectures are identified based on rigorous mathematical principles, and then their governing equations of motion are derived and experimentally tested. The second section of this chapter discusses the synthesis strategy with multiple function targets, where spectral data, variable stiffness, and actuation authorities are all considered *concurrently*. Case studies are presented to compare the performance of different architectures based on the same target to offer design insights and guidelines.

At the end of this chapter 6, a viable approach is proposed to reach our research vision: plant-inspired, large-scale adaptive structure concept capable of sophisticated, concurrent multiple functions. Instead of connecting a large number of F^2MC cells together through a single fluidic circuit, it is more efficient to first synthesize duals or triples of fluidically connected F^2MC cells as a functional unit, and then assemble them mechanically into a large-scale structure. The generic analysis tools and robust synthesis methodologies developed in this thesis can be utilized extensively to optimize the performance of each F^2MC pair or triple, so that the overall structural performance can be tailored for various application requirements.

The final chapter 7 proposes the possible future work on F^2MC based cellular structure, and discusses the potential impact of this thesis work to the field of adaptive structure development in general.

Chapter 3
Preliminary Study on a Dual F^{2}MC String Structure

This chapter discusses the preliminary investigation on a F^{2}MC based dual cell "string" structure in order to gain a basic understanding on the system behavior. The first section of this chapter discusses the derivation and experimental testof an analytical model for the dual cell structure. The second section is on the analysis process and results, where both active and passive operating conditions are considered to search for new types of dynamic functions. Parametric analyses are conducted to identify some system parameters that significantly influence the structure performance. The knowledge and experiences gain from this preliminary work form the basis of the overall thesis research.

3.1 Analytical model

The concept of the F^{2}MC based dual cellular structure is illustrated in figure 3.1. The cells are connected through an internal flow port, which is, in essence, an inertance tube. A fluid flow supply is connected to the grounded cell (cell # 1) and an end mass is attached to the other cell (cell # 2) with an external dynamic force applied on it.

3.1.1 F^{2}MC cellular analysis

The free body diagram in figure 3.1b illustrates that each F^{2}MC cell is subjected to two external loads: an axial force (f), and net fluid pumping (v^{net}) both through the flow

port and from the external flow supply; these two loads will consequently change the two system states: the axial strain (ε_x) and internal fluid pressure (p). It is necessary to understand the correlation between these external loads and system states, because it describes the constitutive relations of the cell wall as well as the coupling between structural deformation and fluid flow. The challenge here is the anisotropy of cell wall in terms of both elasticity and damping. In this study, a hybrid method proposed by Shan (2006) is adopted because it is capable of analyzing the anisotropy by linking the mechanical properties of the cell wall at three different structural scale levels: ply, laminate, and cell level as shown in figure 2.1.

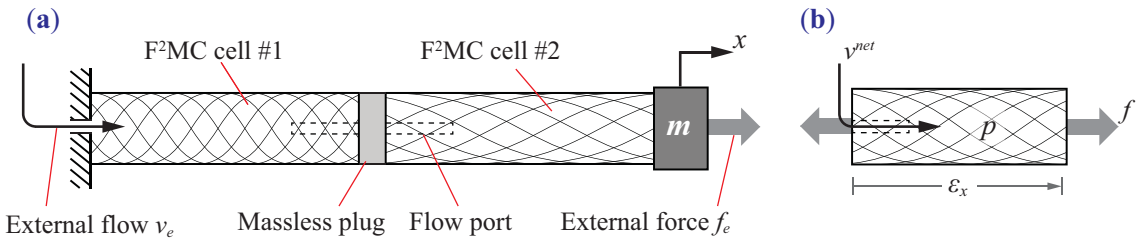

Figure 3.1 Schematic diagram of the dual cellular "string" structure. (**a**) The dual F²MC cellular structure, and (**b**) free body diagram of an individual cell. Positive f means tension force, and positive v^{net} follows the direction to increase the internal volume of F²MC cell, as shown by its arrow.

Cell wall elasticity: In order to analyze the anisotropic elasticity of the cell wall, one can start from the ply level by measuring the storage modulus of the fiber ply in the principle orientations: parallel to fiber (E_1) as well as transverse to the fiber (E_2 and E_3). Then apply Sun's (1998) three-dimensional analysis of thick laminates to calculate the compliance matrix at the laminate level (a_{mn} in the following equations, where $m, n = r, \theta,$

x as illustrated in figure 2.1a). Finally, apply Lekhnitskii's (1963) solution to calculate the normal stress field under the external loads at the cell level:

$$\sigma_r = [Q_1(r) - Q_2(r)]p + \frac{h}{a_{xx}}[1 - Q_3(r) - Q_4(r)]\varepsilon_x, \tag{3.1}$$

$$\sigma_\theta = [\kappa Q_1(r) + \kappa Q_2(r)]p + \frac{h}{a_{xx}}[1 - \kappa Q_3(r) + \kappa Q_4(r)]\varepsilon_x, \tag{3.2}$$

$$\sigma_x = \frac{\varepsilon_x}{a_{xx}} - \frac{1}{a_{xx}}\left(a_{rx}\sigma_r + a_{\theta x}\sigma_\theta\right), \tag{3.3}$$

where $Q_1(r),\ Q_2(r),\ Q_3(r),$ and $Q_4(r)$ are high order polynomial terms that describe the stress distribution in the radial direction. Since the cell wall is physically axisymmetric, the stress and strain distribution is independent to the circumferential coordinate θ. Lekhnitskii gave us the closed form analytical descriptions of these term as follows,

$$Q_1(r) = \frac{a_i^{\kappa+1}}{a_o^{2\kappa} - a_i^{2\kappa}} r^{\kappa-1}, \tag{3.4}$$

$$Q_2(r) = \frac{a_i^{\kappa+1} a_o^{2\kappa}}{a_o^{2\kappa} - a_i^{2\kappa}} r^{-\kappa-1}, \tag{3.5}$$

$$Q_3(r) = \frac{a_o^{\kappa+1} - a_i^{\kappa+1}}{a_o^{2\kappa} - a_i^{2\kappa}} r^{\kappa-1}, \tag{3.6}$$

$$Q_4(r) = \frac{a_o^{\kappa-1} - a_i^{\kappa-1}}{a_o^{2\kappa} - a_i^{2\kappa}} a_i^{\kappa+1} a_o^{\kappa+1} r^{-\kappa-1}, \tag{3.7}$$

where a_o and a_i are the outer and inner radius of F^2MC cell wall and the constants h and κ are calculated as follows,

$$\beta_{ij} = a_{ij} - \frac{a_{ix}a_{jx}}{a_{xx}} \quad (i,j = r,\theta,x)\,, \tag{3.8}$$

$$h = \frac{a_{\theta x} - a_{rx}}{\beta_{rr} - \beta_{\theta\theta}}\,, \tag{3.9}$$

$$\kappa = \left(\frac{\beta_{rr}}{\beta_{\theta\theta}}\right)^{1/2}. \tag{3.10}$$

The normal strain in the fiber composite cell wall can be calculated using three dimensional Hooke's law,

$$\begin{bmatrix} \varepsilon_r \\ \varepsilon_\theta \\ \varepsilon_x \end{bmatrix} = \begin{bmatrix} a_{rr} & a_{r\theta} & a_{rx} \\ a_{r\theta} & a_{\theta\theta} & a_{\theta x} \\ a_{rx} & a_{\theta x} & a_{xx} \end{bmatrix} \begin{bmatrix} \sigma_r \\ \sigma_\theta \\ \sigma_x \end{bmatrix}. \tag{3.11}$$

Note that in the F^{2}MC cell wall constitutive relationship in equation (3.1-3), the fluid pressure inside each individual cell is assumed be uniform. This is essentially a low frequency simplification because at higher frequencies, the fluid pressure wave propagation along the axis of the cylindrical cell might form higher order standing wave modes within. Analytical estimation on the propagation wave length as well as some experiments suggest that the frequency of interest in this study should be below the first acoustic wave propagation natural frequency $f_{cr}\left(=4c_0 \big/ \overline{k}_1 l\right)$, where $\overline{k}_1$ is related to the phase velocity of the wave propagation in F^{2}MC and it can be calculated from dispersion equation, c_0 is the reference velocity, and l is the F^{2}MC cell length. The technical details leading up to f_{cr} are discussed in appendix A. Based on the available F^{2}MC samples, it is recommended to maintain the frequency of interest below 100Hz in this thesis as a rule of thumb to guarantee the accuracy of this uniform pressure distribution assumption.

Cell wall damping: The damping of the fiber composite material could come from different sources (Chandra et al. 1999). In some related studies on the dynamic performance of pneumatic artificial muscles, it is argued that the damping of the fiber composite layer comes from the contact friction between fiber strands, as well as the structure damping of rubber bladder (Tondu and Lopez 2000, Chou and Hannaford 1996, Davis et al. 2003, Kang et al. 2009 and Reynolds et al. 2003). In F^2MC cell, however, the fibers are embedded into the resin so they do not contact with each other directly; therefore, the cellular damping comes mostly from the structural damping of the soft matrix resin material. Two hysteric loss factors of the cell level (η^p and η^ε) are proposed in corresponding to the two system states. To calculate η^p, for example, one can prescribe an internal pressure to the cell without axial strain in equation (3.1) and (3.2). Then calculate the principle stress and strain at the ply level to derive the total wall strain energy (Shan 2006),

$$W(p) = \frac{1}{2}\int_V \left(\sigma_{11}\varepsilon_{11} + \sigma_{22}\varepsilon_{22} + \sigma_{33}\varepsilon_{33} + \tau_{12}\gamma_{12}\right) \mathrm{d}V\,, \tag{3.12}$$

where the sub-index 1 represents the orientation parallel to the fiber, 2 and 3 transverse to fiber (figure 2.1c), and V stands for the volume of the F^2MC cell wall. The total energy loss due to damping can then be calculated as,

$$\Delta W(p) = \pi\int_V \left(\eta_{11}\sigma_{11}\varepsilon_{11} + \eta_{22}\sigma_{22}\varepsilon_{22} + \eta_{33}\sigma_{33}\varepsilon_{33} + \eta_{12}\tau_{12}\gamma_{12}\right) \mathrm{d}V\,, \tag{3.13}$$

where η_{mn} (m, n = 1, 2, 3) are the principle material loss factors, which can be measured by dynamic modulus analysis test (DMA) on the fiber composite sample. The loss factor at the cell level is the ratio of net strain energy loss over total strain energy:

$$\eta^{p} = \frac{\Delta W(p)}{2\pi W(p)}. \tag{3.14}$$

The other cell loss factor η^{ε} can be calculated in a similar fashion by prescribing an axial strain to the cell without internal pressure.

Correlation between system states and external loads: With the anisotropic elasticity and damping analyzed, one can calculate the internal cell volume change as follows,

$$\Delta V^{cell} = V_o^{cell}\left(2\varepsilon_\theta + \varepsilon_x\right)\Big|_{r=a_i}, \tag{3.15}$$

where V_o^{cell} is the initial cell internal volume. If the working fluid is incompressible, the change in cell volume (V_o^{cell}) equals to the net volume of the fluid flow into the cell. In reality, however, the fluid is compressible and its effective bulk modulus (B_f) is influenced by the entrapped air bubbles and other structural compliances such as fluid circuit dead volume and flow port wall elasticity. Under such conditions, we can apply the ideal linear compressible fluid model to relate the net fluid flow (v^{net}) to cell volume change as follows,

$$v^{net} = \frac{B_f}{B_f - p}\left(V_o^{cell} - \Delta V^{cell}\right) - V_o^{cell} \cong Ap + B\varepsilon. \tag{3.16}$$

For simplicity, we will denote ε_x as ε from now on. Note that the linearization in equation (3.16) uses Taylor expansion, assuming only small deformations considered in this study. One can calculate the internal axial force on F^2MC cell from its storage modulus as follows,

$$f = 2\pi\int_{a_i}^{a_o} \sigma_x r\mathrm{d}r - \pi a_i^2 p = Cp + D\varepsilon. \tag{3.17}$$

If the cell is subject to dynamic loading, the loss factor needs to be considered,

$$f = C\left(1+\mathbf{i}\eta^p\right)p + D\left(1+\mathbf{i}\eta^\varepsilon\right)\varepsilon, \tag{3.18}$$

where **i** is the imaginary unit. A sub-index k is introduced to distinguish the variables corresponding to different cells (in this chapter, k = 1 and 2), and the correlation between the system states of the F^{2}MC cells (p_k and ε_k) and the applied loads (f_k and v_k^{net}) can be written based on equation (3.16) and (3.18)

$$v_k^{net} = A_k p_k + B_k \varepsilon_k, \tag{3.19}$$

$$f_k = C_k\left(1+\mathbf{i}\eta_k^p\right)p_k + D_k\left(1+\mathbf{i}\eta_k^\varepsilon\right)\varepsilon_k = C_k^* p_k + D_k^* \varepsilon_k, \tag{3.20}$$

where the detailed derivations of A_k, B_k, C_k, and D_k are given in appendix B.

3.1.2 Flow port dynamics

Figure 3.2 is a detailed blow-up view of the flow port layout. The flow port is essentially an inertance circular tube embedded through the plug with two ends intruding into the two adjacent F^{2}MC cells. The inertance tube has a cross-section area of S and length of l_p, while the length of its intrusion into the two cell are l_{i_1} and l_{i_2}, respectively. Denote S_2 as the annular area between the cell wall and inertance tube ($S_2 = \pi a_i^2 - S$), ρ as the fluid density, c is the wave propagation speed, and ω as the angular frequency. Denote v_1 as the flow volume from cell #1 into the flow port, and v_2 as the flow volume from cell #2. The pressure p_k and flow volume v_k (not to be confused by flow rate, which is

the time derivative of the flow volume) between the two ends of the inertance tube can be related by a transfer matrices, in *Laplace domain*, as follows:

$$\begin{bmatrix} p_1 \\ -v_1 \end{bmatrix} = \mathbf{T}_{i_1} \mathbf{T}_f \mathbf{T}_{i_2} \begin{bmatrix} p_2 \\ v_2 \end{bmatrix}, \tag{3.21}$$

where the minus sign before v_1 is added to be consistent with the definition in figure 3.1.

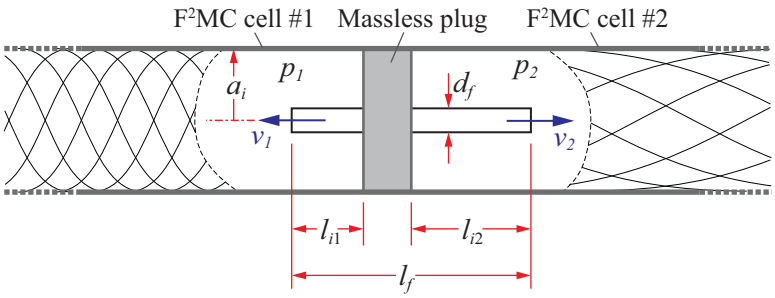

Figure 3.2 Schematic layout of the interface between two adjacent F²MC cells. A massless plug block the fluid flow between two cylindrical shaped cells except though the flow port. The dimension of the flow port, as well as length of its intrusion into the cell interior all affects the fluid dynamics.

The transfer matrixes $\mathbf{T}_{i_k}$ relates to the two intrusions, and $\mathbf{T}_f$ relates to the inertance of the flow port:

$$\mathbf{T}_{i_k} = \begin{bmatrix} 1 & 0 \\ -\dfrac{S_2}{\rho \omega c} \tan\left(\dfrac{\omega l_{i_k}}{c}\right) & 1 \end{bmatrix}, \quad k = 1, 2, \tag{3.22}$$

$$\mathbf{T}_f = \begin{bmatrix} \cos(\frac{\omega l_f}{c}) & \frac{\rho\omega c}{S}\sin(\frac{\omega l_f}{c}) \\ -\frac{S}{\rho\omega c}\sin(\frac{\omega l_f}{c}) & \cos(\frac{\omega l_f}{c}) \end{bmatrix}, \tag{3.23}$$

Since the frequency of interest in this thesis work is below 100Hz ($\frac{\omega l}{c} << 1$), low frequency estimation can be applied to simplify the transfer matrixes as follows,

$$\mathbf{T}_{i_k} = \begin{bmatrix} 1 & 0 \\ -\frac{S_2 l_{i_k}}{\rho c^2} & 1 \end{bmatrix}, \tag{3.24}$$

$$\mathbf{T}_f = \begin{bmatrix} 1 & \frac{\rho l_f}{S}\omega^2 \\ -\frac{S l_f}{\rho c^2} & 1 \end{bmatrix} \cong \begin{bmatrix} 1 & I\omega^2 \\ 0 & 1 \end{bmatrix}. \tag{3.25}$$

Note that the $-\frac{S l_f}{\rho c^2}$ element in equation (3.25) is assumed to be zero since it's infinitesimally small compared to other elements in $\mathbf{T}_f$; this indicates that the flow volume into and out of the flow port are assumed to be the same ($-v_1 = v_2$). Finally, if the intrusion is short enough so that $-\frac{S_2 l_{i_k}}{\rho c^2}$ in equation (3.24) becomes a magnitude smaller than A_k from equation (3.19 and 20, $k = 1$ or 2), its effects onto the fluid dynamics become negligible (see appendix C). As a result, the flow port dynamics equation (3.21) can be simplified into a classic flow port equation in *time domain* (Watton, 1989),

$$I\dot{v} + R\dot{v} + (p_2 - p_1) = 0, \tag{3.26}$$

where $v\,(=v_2=-v_1)$ is defined as the flow volume through the flow port. I is the flow port inertance as defined in equation (3.25), and R is the port resistance. To estimate the resistance, a laminate flow port inertance model is employed (Merritt, 1991),

$$R=\frac{128\mu l_f}{\pi d_f^4}\left(1+\frac{2.28+K_m}{64}\frac{d_f R_e}{l_f}\right), \tag{3.27}$$

where μ is the dynamic viscosity of the working fluid, K_m is the minor head loss in the flow circuit from the inlet and outlet of the flow port, R_e is the Reynolds number and d_f is the flow port diameter. It is hard to characterize the Reynolds number of the oscillating flow through the port, so the value of 2000 will be used as an estimation based on the laminate flow assumption.

3.1.3 System governing equation

Two compatibility conditions are derived based on physical principles. The first compatibility condition states the conservation of fluid mass,

$$\begin{cases} v_1^{net}=v_e-v \\ v_2^{net}=v \end{cases} \tag{3.28}$$

where v_e is the fluid volume displacement from external pumping. Assuming the flow port massless, the second compatibility condition states the balance of internal force between the two F^{2}MC cells (figure 3.3),

$$f_1=f_2. \tag{3.29}$$

And, the end mass dynamics can be characterized as,

$$m\ddot{x} + f_2 = f_e, \tag{3.30}$$

where the end displacement $x = l_1\varepsilon_1 + l_2\varepsilon_2$, and l_k are the length of the corresponding F^{2}MC cells, and m is the end mass.

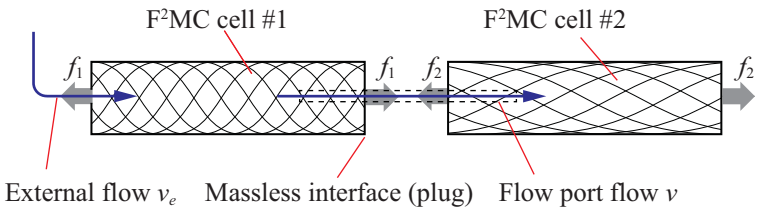

Figure 3.3 Schematic illustration of the compatibility conditions between the two F^{2}MC cell for equations (3.28, 29).

Choosing the end mass displacement (x) and the flow port fluid flow volume (v) as the dependent variables, one can combine the compatibility conditions (3.28, 3.29), the dynamic equations (3.26, 3.30), and performance relationship (3.19, 3.20) to write the system governing equations in the following form:

$$\begin{bmatrix} m & 0 \\ 0 & I \end{bmatrix}\begin{bmatrix} \ddot{x} \\ \ddot{v} \end{bmatrix} + \begin{bmatrix} 0 & 0 \\ 0 & R \end{bmatrix}\begin{bmatrix} \dot{x} \\ \dot{v} \end{bmatrix} + \begin{bmatrix} \mathbf{K}_{11}^* & \mathbf{K}_{12}^* \\ \mathbf{K}_{12}^* & \mathbf{K}_{22}^* \end{bmatrix}\begin{bmatrix} x \\ v \end{bmatrix} = \begin{bmatrix} 1 \\ 0 \end{bmatrix} f_e + \begin{bmatrix} \mathbf{G}_1^* \\ \mathbf{G}_2^* \end{bmatrix} v_e, \tag{3.31}$$

where the complex value variables $\mathbf{K}_{ij}^*$ and $\mathbf{G}_j^*$ are complicated expressions of the aforementioned material and design parameters. As can be seen, this F^{2}MC dual cellular ele-

ment is equivalent to a two-degree of freedom oscillator that consists of a structural generalized coordinate (x) and a fluidic generalized coordinate (v). These two generalized coordinates are coupled through $\mathbf{K}_{12}^{*}$, which relates to the difference between anisotropic properties of the two F^{2}MC cells. From this observation, it is clear that the design of the two F^{2}MC cells, especially the difference between them, plays an important role in the system dynamical response.

Overall, the dual-cell F^{2}MC cellular structure model presented above provides us with an effective analytical tool for system functionality analysis, as discussed in the following section.

3.2 System function analysis

In this section, the dynamic characteristics of the cellular structure are analyzed based on the derived model, under both passive and active operation conditions. In parallel, experimental investigations are carried out on several specimens to test the analytical observations.

3.2.1 Experimental set up

Three F^{2}MC cell samples are fabricated, with ±32º, ±42º, and ±70º fiber angles, by filament winding (AS4D carbon fiber and Reoflex20 urethane rubber resin at 57% fiber volume ratio). The cell samples are assembled into a dual cell testing setup for passive type of functions, where the external force is provided by a shaker and the end mass motion measured by an accelerometer (figure 3.4). The measurement data from the force trans-

ducer and accelerometer are sent to a digital signal analyzer (HP 35670A) for signal analysis, and uniform windowing and simple moving average technique are used to reduce the instrument electronic noise. Water is selected as the working fluid. The flow port is made of PVC tubing with three different lengths. Table 3.1 outlines the material properties and structural parameters, and table 3.2 outlines the key performance parameters of the sample F^2MC cells.

The principle loss factor (η^p and η^ε) and ply stiffness transverse to the fiber orientation (E_2) are estimated by the following procedure: 1) the empty ±70º cell sample is connected to the end mass, a sweeping frequency signal is applied by the shaker to identify the resonance peak in the frequency response. 2) The E_2 value is estimated by matching the position of the measured peak to the analysis prediction, and η^p, η^ε are estimated by matching the amplitude of the peaks. To test the estimated E_2, η^p and η^ε values, they are used to predict the frequency responses of the ±42º and ±32º cells and compared with the direct experimental results obtained via sweeping frequency tests on the corresponding cell samples. The outcomes show that the measured resonance peaks match the predictions well, indicating that the E_2, η^p, and η^ε values are correctly estimated. Figure 3.5 demonstrates the variation of the cell wall damping coefficient with respect to the fiber angle. The rest of the experimental results are also obtained by the same sweeping frequency test set up. These results are reported in the following section and they are compared to the analysis predictions.

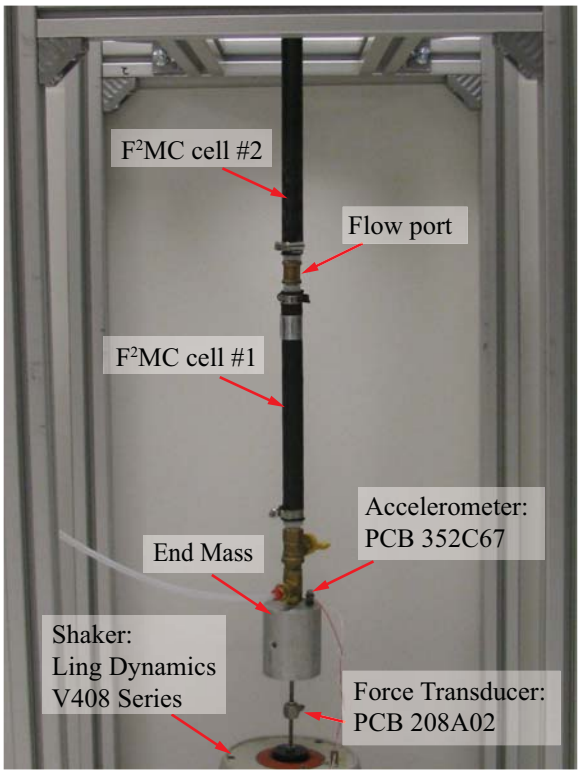

Figure 3.4 The dual cellular test setup under passive type of operation. This set up follows closely to the schematic design shown in figure 3.1.

Table 3.1 Material and design parameters of the dual cell structure test

Properties	Value	Properties	Value
E_1	145 GPa	E_2 ,E_3	50 MPa
$G_{12} = 0.8\ E_2$	40 MPa	η_{11}	0.011
η_{22}, η_{33}	0.4	$\eta_{12} = \eta_{22}$	0.4
Cell outer radius (a_o)	11.3 mm	Flow port length (l_f)	10.1, 15.2, 20.3 cm
Cell inner radius (a_i)	10 mm	Flow port diameter (d_f)	4.3 mm
Cell length (l_1, l_2)	20 cm	Minor head loss (K_m)	0.8
End mass (m)	0.9 kg	Dynamic viscosity (μ)	0.798×10^{-3} N s/m^2
F^{2}MC cell mass (m_{cell})	0.03 kg		

Table 3.2 Parameters of the sample F^2MC cells as in equation (3.19, 20), the estimated critical frequency uniform pressure distribution is calculated based on appendix A. (fluid effective bulk modulus: 17 MPa)

φ	±32º	±42º	±70º
A (m^3/Pa)	3.80×10^{-12}	3.74×10^{-12}	3.71×10^{-12}
B (m^3)	-2.88×10^{-4}	-1.02×10^{-4}	5.01×10^{-5}
C (N/Pa)	1.44×10^{-3}	5.11×10^{-4}	-2.51×10^{-4}
D (N)	6.51×10^{4}	2.33×10^{4}	8.98×10^{3}
η^p	0.07	0.11	0.18
η^ε	0.30	0.31	0.31
f_{cr} (Hz)	76	91	158

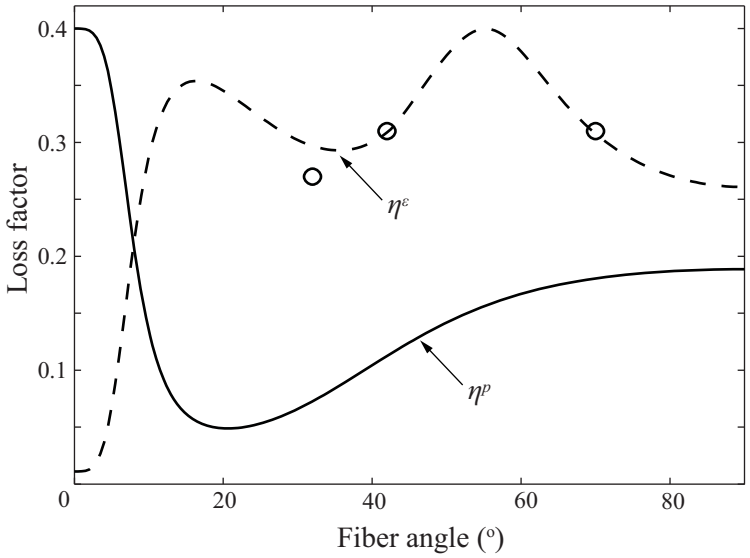

Figure 3.5 Variation of cell wall damping with respect to fiber angle (equation 3.12-14). The circles are the test results of η^ε from the cell samples

3.2.1 Passive type of operation

In a passive operation, the working fluids are not being pumped into the cell and the dual cellular pair is subject to external load on the end mass. As mentioned in the

review section of chapter 2, a single F^2MC cell exhibits variable axial stiffness with on/off valve control at both ends of the cell. It is then natural to investigate whether a dual F^2MC cellular structure can exhibit similar variable stiffness.

The analytical model derived in the previous section can answer this question by comparing the static displacement of the end mass when the two cells have different fiber angle combinations. Figure 3.6 shows the close/open valve axial stiffness ratio of the dual cell structure, where the fiber angle of cell #1 is fixed, and the fiber angle of cell #2 span from 0º to 90º. The close valve stiffness is calculated as the ratio of external force f_e over the end mass displacement, at static condition,

$$K_{close} = \frac{f_e}{x} = \mathbf{K}_{11} - \frac{\mathbf{K}_{12}^2}{\mathbf{K}_{22}}, \tag{3.32}$$

where $\mathbf{K}_{ij}$ is the real part of the stiffness matrix entries in governing equation (3.31). Note that in the closed valve stage, the working fluid could not flow in and out of the cellular structure, but is still free to flow between the two cells through the flow port. When the two cells have the same fiber angle, the dual cell structure is equivalent to a single cell structure in static condition.

The dual cellular structure is considered in open valve stage when the working fluid is free to flow in and out of the whole system as well as in between the cells. The open valve stiffness is of the whole structure is equivalent to the two individual cell wall axial stiffness connected in series:

$$K_{open} = \left(\frac{l_1}{\delta_1} + \frac{l_2}{\delta_2} \right)^{-1} . \tag{3.33}$$

As can been seen from the simulations, the dual cellular structure still exhibit variable axial stiffness by opening and closing the valve, however the equivalent stiffness ratio is less than those of a single F^{2}MC cell. This is due to the fact that the axial stiffness increases in closed valve state because the high bulk modulus working fluid resists the volume change induced by the anisotropic cell wall. When the two cells have different fiber angles, the working fluid is free to flow from one cell to another, so it cannot effectively resist the volume change.

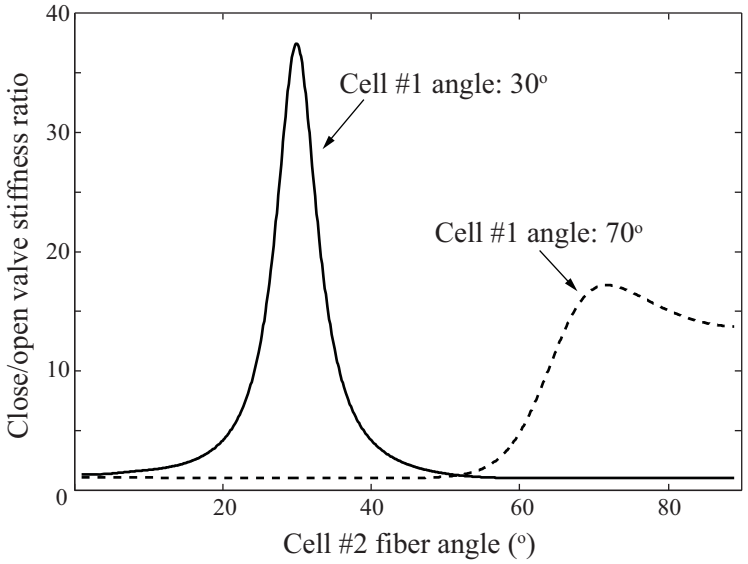

Figure 3.6 The variable stiffness of a dual cellular string structure. Bulk modulus is assumed 2GPa. The peaks represent the stiffness ratio when the two cells have the same fiber angle.

Although the going from single cell to dual cell does not directly benefit us regarding to increasing the ratio of open/close valve static stiffness, it will offer us new type of

functionalities in the dynamic regime. Compared to a single F^2MC cell, the extra flow port inertance in the dual cellular structure resembles a sacrificial mass in a vibration absorber. Therefore, we could exploit the system dynamic characteristics for vibration management purposes. Here the ratio of the end mass acceleration over the external force magnitude is used as the performance index.

If the two F^2MC cells are identical, the coupling stiffness $\mathbf{K}_{12}^{*}$ term in equation (3.31) becomes zero, which means the fluidic dynamics is decoupled from the structural dynamics, and it would not be excited by external force alone. As a result, the structural system response resembles a typical single degree of freedom oscillator. On the other hand, when the two cells have different fiber angles, $\mathbf{K}_{12}^{*}$ becomes finite and the system response will show a zero-poles response, where the lower frequency pole is dominated by the flow port dynamics (here referred as *fluidic pole* and *fluidic mode*), and the higher frequency pole is dominated by the cell wall structural dynamics (*structural pole* and *structural mode*). The system zero can then be used as the vibration absorption frequency (figure 3.7).

The experiment results plotted in figure 3.7 match well with analytical predictions in terms of the pole and zero positions. There are some discrepancies in terms of the magnitude of the poles and zeros, indicating that overall damping from the tested prototype is higher than the analysis prediction. Given the fact that the F^2MC cell wall damping is predicted well by the analytical model, the extra damping is probably due to the turbulent nature of the pulsate flow in the flow port. Luo et al. (2005) pointed out that the viscous component becomes predominant in the small diameter inertance tube from turbulent flow, especially at higher frequencies. One can reduce this extra flow resistance by adjusting the

flow circuit design for a lower Reynolds number, such as using a larger flow port diameter, smoother port inlet and outlet, and other type of working fluid. Overall, despite the discrepancies, the proposed model can still be utilized for system analysis of the F^2MC cellular structure, for it gives us clear physical insights on the characteristics of the integrated system, as well as how its dynamics are influenced by the key parameters.

The effective fluid bulk modulus plays an important role in the frequency response. If the effective fluid bulk modulus is reduced because of entrapped air bubble, the system zero and the structural modal frequency will shift to the lower frequency range (figure 3.8). By examining the mode shapes, one can find that the structural mode (the higher frequency pole) involves compressing the working fluid while the fluidic mode not as much, and thus the fluidic modal frequency is not much affected by the bulk modulus variations. Since the bulk modulus serves as a potential energy storage element, a decrease in effective bulk modulus will reduce the system equivalent stiffness contributing to the structural mode, therefore lower its frequency. In the experiment results, the effective bulk modulus is estimated to be 17MPa by fitting the poles and zero positions on the 32º-70º pair test with 15.2cm port length. This estimated value produces good matching between the analysis and experimental results for all the other tests.

Different combinations of fiber angles will assign the system poles and zeros to different positions, which can be seen in results shown in figures 3.9 and 3.10. The system zero varies in a wide range, especially when both cells are of contraction type (fiber angle smaller than 55°) and the fluid bulk modulus is high. In each plot, there are two points where pole-zero cancellation occurs. One with the same fiber angles between two cells, the other with one fiber angle close to ±55°. This ±55° fiber angle is a critical value where

axial strain would not induce any noticeable internal cell volume change, and consequently no fluid flow.

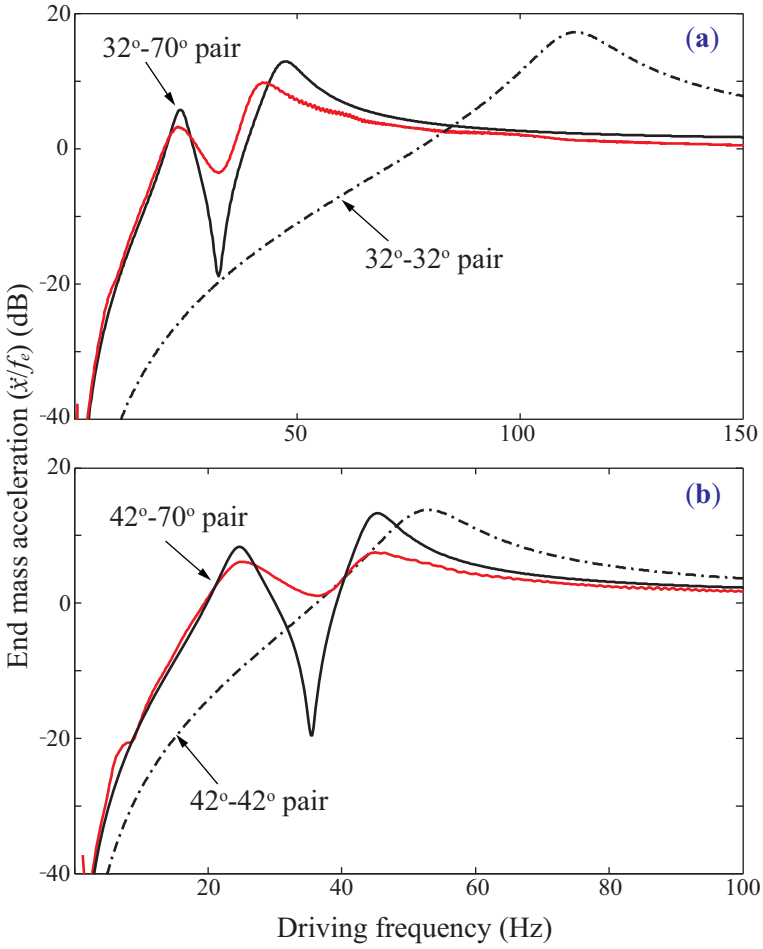

Figure 3.7 Vibration absorption performance of the F^{2}MC cellular structure. (**a**) Response of a 32°-70° pair compared to a 32°-32° pair. (**b**) Response of a 42°-70° pair compared to a 42°-42° pair. The black solid lines are analysis prediction, and the red solid lines are experiment results. The effective fluid bulk modulus is 17 MPa, and port length is 15.2 cm.

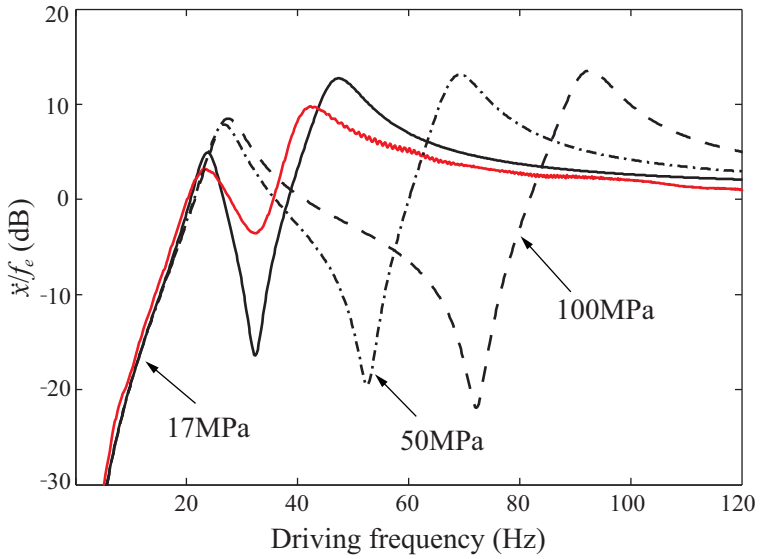

Figure 3.8 System response with different effective bulk modulus (B_f). 32º-70º pair, port length 15.2cm. The dashed line is the experiment result.

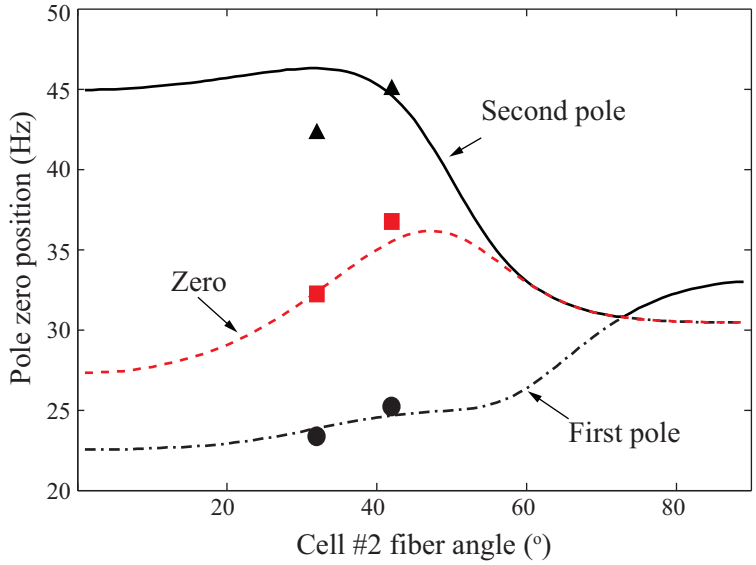

Figure 3.9 Poles and zeros position with different fiber angle combinations. Cell #1 fiber angle is fixed at 70º, port length at 15.2 cm. The markers are corresponding experiment results

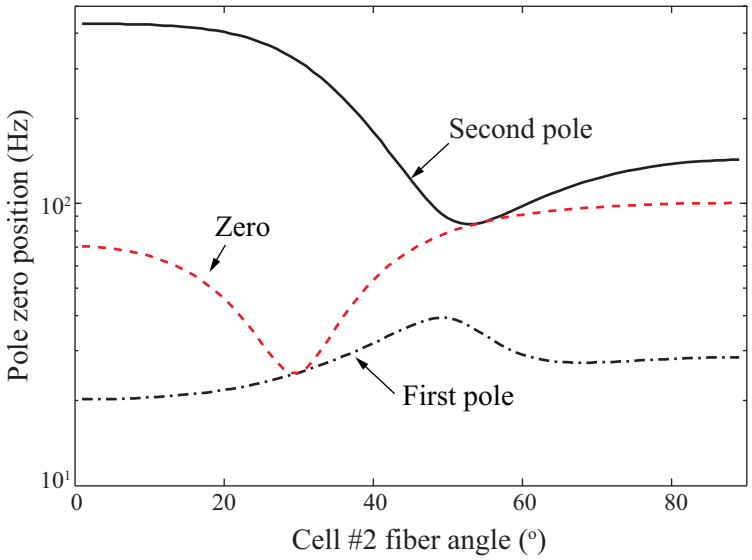

Figure 3.10 Poles and zeros position with different fiber angle combinations, Cell #1 fiber angle is fixed at 30°, B_f = 200MPa.

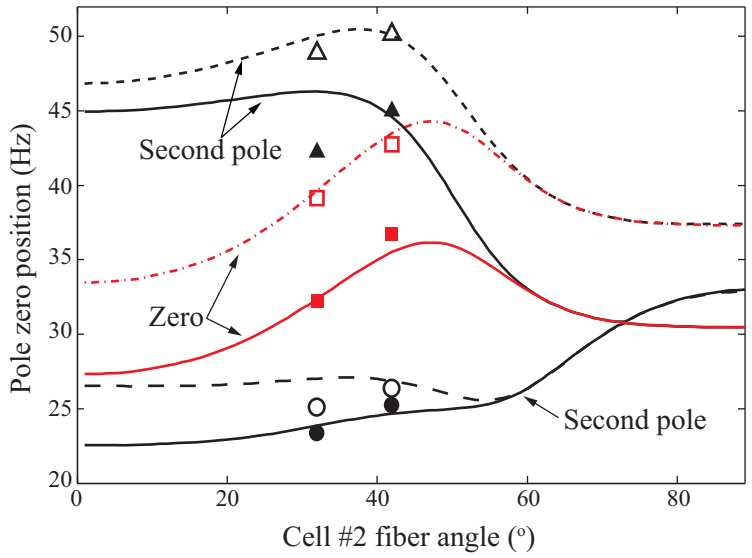

Figure 3.11 Poles and zeros position moves as the flow-port length changes. The markers are corresponding experiment results. The solid lines and solid markers represent the test with port length of 10.1cm, dashed lines and hollow markers with 20.3cm port length.

The flow port length is another parameter for tuning the vibration absorber, which is tested by the experiments with 3 different flow port lengths (figures 3.9 and 3.11). As shown, the test results agree with the analysis in terms of the pole and zero positions with error less than 5Hz. Based on these plots, one can make the vibration absorber adaptable to system operating condition changes by adjusting the flow port inertance.

3.2.3 Active function as an enhanced actuator

With the analytical model, it is feasible to further explore the active function of the F^2MC as an actuator. In this case external flow is pumped into the cellular structure and no external force is applied to the end mass. The actuation performance of a dual F^2MC cellular structure is compared to that of a single cell device based on actuation free stroke and power density. As the system would be excited by a harmonic external flow, the power density is defined as the end mass kinetic energy per time period, normalized by the total mass of fluid-filled F^2MC cells (m_{cell}):

$$PD(\omega) = \frac{1}{T}\frac{KE_{mass}}{m_{cell}} = \frac{m}{m_{cell}}\frac{\dot{x}^2}{2T}, \tag{3.34}$$

where T is the period corresponding to exciting frequency. Figure 3.12 shows the system performance of a single 30° F^2MC cellular structure (dashed line), which resembles a typical single degree of freedom elastic actuator. If half of the 30° cell at the flow supply end is replaced by an 80° cell, with an internal flow port connecting the two segments (figure 3.12a), one can identify a frequency range where the dual cellular actuator has a higher actuation authority over the single cell device (the dot overlay on solid line). This higher

authority frequency bandwidth is defined according to the industrial convention as the frequency between the two peaks with 3 dB drop from the peak value. This range spans from below 20 Hz to the 50 Hz level, which is practical for a hydraulic actuation system.

With a quasi-static external fluid supply, the deformations of the 30º and 80º cell are out of phase, so they will cancel out each other at the free end and the frequency response shows a system zero very close to 0 Hz. However, once the driving frequency exceeds the system zero frequency, the resonance effect will increase the system response amplitude between the two system poles. F^2MC cell, by nature, is a heavily damped composite so utilizing this resonance effect is safe in practical applications.

Similar to the passive type of operation, the system response can be tailored by changing the fiber angle combination. However, not all of the combination will provide the desired increase in actuation authority. Generally speaking, starting from a contraction type of actuator with fiber angle smaller than 55^o, actuation authority can be increased in the desired frequency range by replacing part of the cell with a fiber angle higher than at the flow supply end.

Figure 3.13 shows the effects of flow port length on actuator authority (for comparison sake, the increase of power density is plotted against their corresponding operation frequency). It can be shown that, the longer the flow port length (i.e. higher flow port inertance), the wider the high authority frequency bandwidth. However, the tradeoff is that the corresponding increase in authority would be reduced. Effective working fluid bulk modulus, again, has impact on actuation performance similar to the passive case. Figure 3.14 shows that a decrease in the bulk modulus will reduce the available operation bandwidth for higher authority.

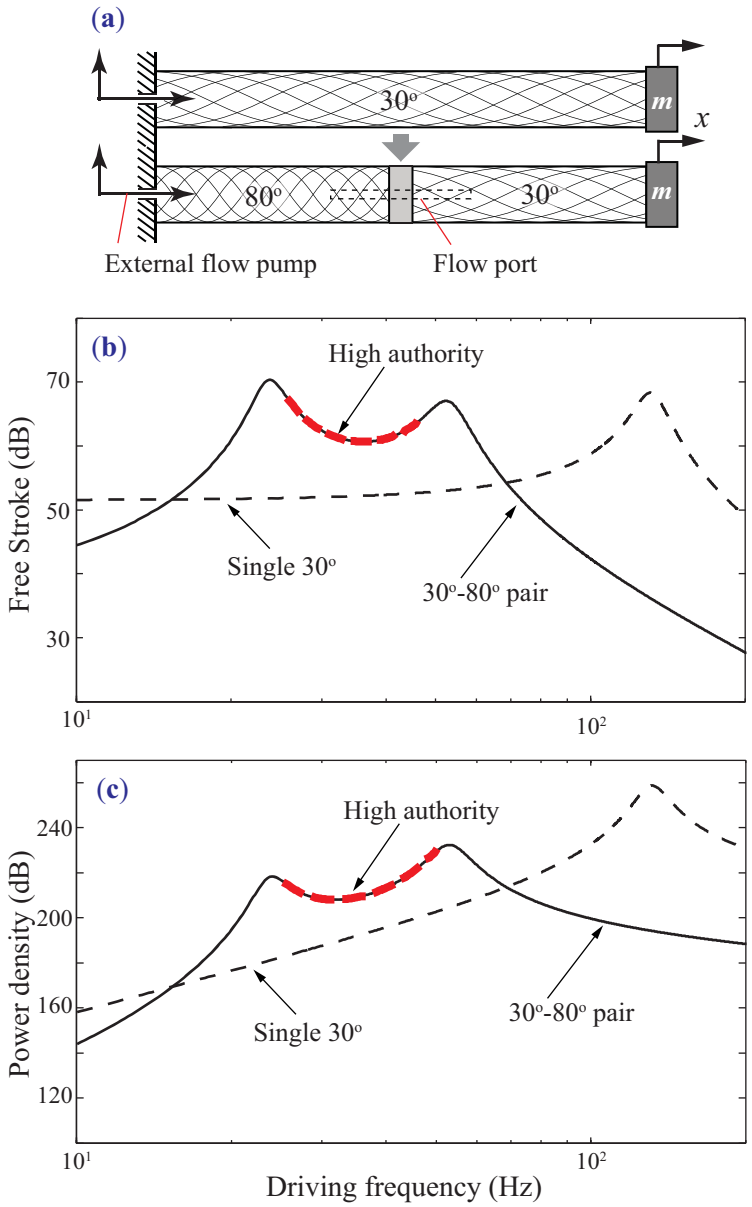

Figure 3.12 Actuation performance of a single and dual cell structure. (**a**) The laid out of the dual cellular structure for actation purposes, compared to a single cell. (**b**) Actuation performance in terms of free stroke. (**c**) Actuation performance in terms of power density. Dashed line: singe 30° cell, solid line: 30°-80° pair, port length: 15.2cm, bulk modulus 17MPa

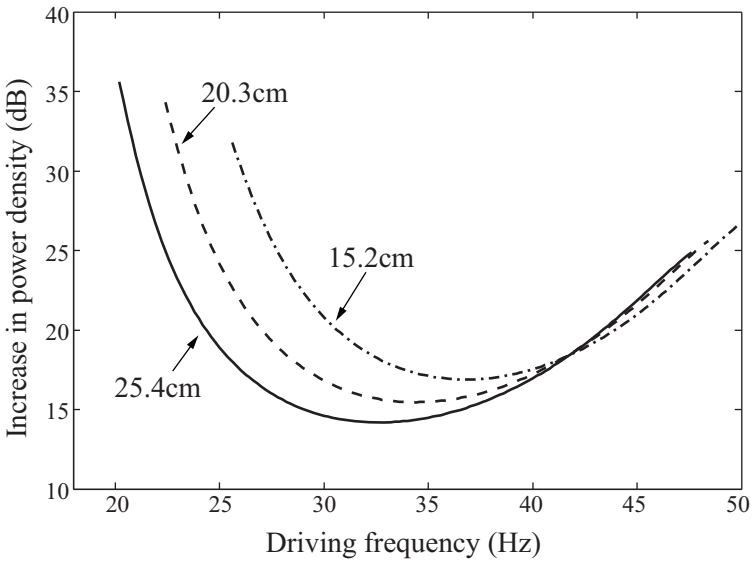

Figure 3.13 Effects of flow port length on the power density improvement (bulk modulus 17MPa)

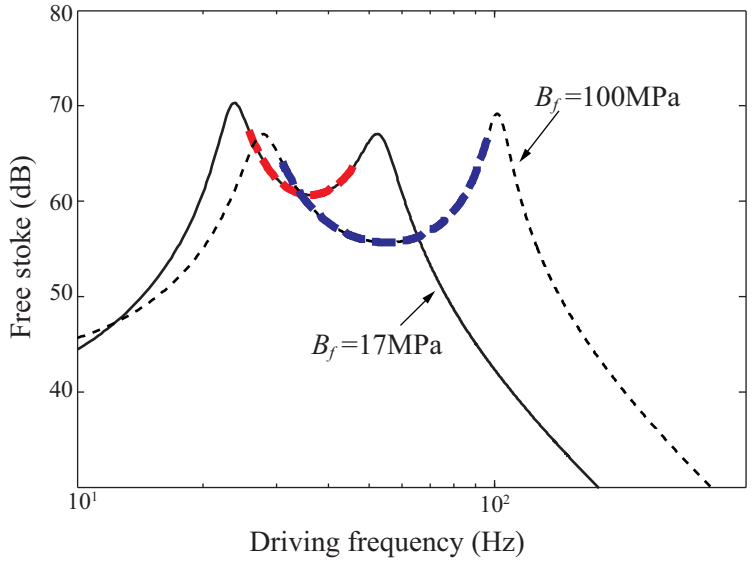

Figure 3.14 Effects of effective fluid bulk modulus.
solid line: B_f=17MPa, dashed line: B_f=100MPa, port length 15.2cm

It is worth noting that in governing equation of motion (3.31), the activating input is external fluid volume input v_e. In practical engineering applications, external pressure supply is another common activating input. Working with pressure pumping will result in a different dynamic system, and it will be discusses in chapter 6.

3.3 Summary

The dynamic characteristics of an F^2MC based dual cellular structure are investigated to gain new understanding and explore new types of functionalities. An analytical model is developed and analyzed, and experimental investigations are performed. This preliminary investigation is the first attempt in this research field to understand interaction between different F^2MC cells through fluidics, therefore it brings a paradigm shift from a single cell focused study to multiple cell focused study. The functionality study results in the development of two new types of dynamic functions. In a passive operation, the dual cellular structure can be used as a vibration absorber. On the other hand, in an active operation, the dual cellular structure can be used as a resonance actuator with an enhanced authority in certain bandwidth as compared to the single cell actuator. Combined with the previous work on actuation and variable stiffness discussed in chapter 2, these new dynamic functions makes the F^2MC based cellular structure even more appealing for various engineering applications.

The versatility of design of the proposed cellular structure is also explored in the preliminary parametric analysis. The fiber angle combination of the F^2MC cells and the flow port inertance are identified as two of the parameters that affect system performance significantly. It is recognized that the system performance can be tailored in a large range

in terms of pole and zero positions. It is also recognized that the variation of effective bulk modulus of the working fluid has significant effects on the system characteristics. Therefore the effective bulk modulus shall be closely monitored in the experiment efforts in the following research works.

Despite of the development of new functionalities and the knowledge of the system dynamic behavior, the research work in this chapter focuses on performance modeling and case studies. Deeper physical insights and robust design methodologies are necessary, and they are discussed in the next chapter.

Chapter 4
Dual Cellular String Structure: Physical Insight and Synthesis

The preliminary development of the dual F^2MC cellular string structure discussed in chapter 3 has demonstrated promising potential. However, these investigations have focused on performance modeling and case studies. It is clear that to advance the state of the art, the next steps are to develop rigorous and systematic methodologies so one can gain better insights and synthesize dual-cell F^2MC structural systems to achieve desired performance.

First, the complexity of a multiple cellular structure requires us to understand how a change in individual cell influences the overall structural dynamics. This requires a model that one can efficiently perform large-scale parametric analysis, which is beyond the capability of the model in chapter 3. The challenge comes from the large number of system parameters: the F^2MC cellular structural dynamics is determined by different types of physical variables, such as the cell wall material properties, fiber layout, and fluid circuit design. The complicated mathematics employed in the previous model makes it challenging to systematically analyze and understand the correlation between all of these individual parameters to the system dynamics as a whole. That is, the previous model could neither provide much physical insight nor be used to perform parametric analysis effectively and efficiently.

Secondly, in order to investigate the potential of the multiple F^2MC cellular structures in any real-world applications, a viable synthesis tool is a necessity. Such tool needs to be able to search for feasible cellular structural designs for a given target performance (e.g., poles and zero positions, or spectral data). However, with the previous model one could only rely on an optimization iteration procedure to perform such synthesis, which might be computational expensive yet non-comprehensive.

In this chapter, we propose to address the aforementioned issues and advance the state of the art through a three-step effort. The first step is to develop a non-dimensional dynamic model of the F^2MC based dual-cellular "string" structure. Through this process, the number of analysis and design parameters can be reduced. The second step is to analyze and gain physical insight of the equivalent "stiffness matrix" in the governing equation of motion in the non-dimensional model. This helps us uncover the missing link between the overall structural dynamics and the individual cell performance. The third step is to develop a synthesis tool for the dual cellular structure based on the *performance parameters* of each individual cell. Working with these parameters, rather than the physical variables, can greatly simplify the synthesis procedure and makes it realistic to handle. The following sections of this chapter are organized according to the aforementioned three steps.

4.1 Non-dimensional model development

The dual cellular structure studied in this chapter is the same as the one in chapter 3 (figure 3.1), however, to illustrate the physical principles without unnecessary complexity, only the passive cases are studied; that is, there would be no external pumping of fluids into the dual cellular system. Therefore, the total amount of working fluid contained in the two

F^2MC cells is a constant, even though the fluid can flow from one cell to another through the flow port. The structural damping of the F^2MC cell is neglected as well but this will not compromise the purpose of the study in this chapter.

To non-dimensionalize the analytical model, the following characteristic units are employed: inner radius of the F^2MC cell (a_i [m]), the elastic modulus of the cell wall fiber ply transverse to the fiber direction (E_2 [m sec^{-2} kg^{-1}], figure 2.1c), and the working fluid density (ρ [kg m^{-3}]). These three units are intrinsic to the cellular structure and they form an equivalent basis as the three fundamental dimensions in mechanical system: mass, length, and time (Palacios, 1964).

4.1.1 Non-dimensional F^2MC cellular model

One can use these characteristic units to non-dimensionalize the internal pressure in F^2MC cell #k (p_k), axial strain (ε_k), internal force (f_k), and the flow volume through flow port (v) (figure 3.1b), note that from equation (4.1) to (4.13), the sub index k are omitted for clarity, and these equations are intended for an individual cell.

$$\varepsilon = \frac{dx}{l} = \frac{dx}{a_i}\frac{a_i}{l} = \frac{\hat{\varepsilon}}{g}, \tag{4.1}$$

$$p = E_2 \hat{p}, \tag{4.2}$$

$$v = \pi a_i^3 \hat{v}, \tag{4.3}$$

$$f = E_2 \pi a_i^2 \hat{f}\ . \tag{4.4}$$

Here the parameters with an over-hat are in their dimensionless form. g is the aspect ratio relating to the shape of the cell ($g = l/a_i$). Equation (3.19) and (3.20) can be normalized as,

$$\phi_k \hat{v} = g\hat{\alpha}_k \hat{p}_k + \hat{\beta}_k \hat{\varepsilon}_k , \tag{4.5}$$

$$\hat{f}_k = \hat{\gamma}_k \hat{p}_k + \hat{\varepsilon}_k \hat{\delta}_k / g , \tag{4.6}$$

where the constant ϕ_k equals to -1 when $k=1$; or equals to 1 when k=2. The dimensionless parameters $\hat{\alpha}_k$, $\hat{\beta}_k$, $\hat{\gamma}_k$, and $\hat{\delta}_k$ can be called *performance parameters*, and they are calculated in detail as follows,

$$\hat{\alpha} = E_2(-2\beta_{r\theta} + 2\kappa\beta_{\theta\theta}\frac{1+c^{2\kappa}}{1-c^{2\kappa}}) + \frac{E_2}{B_k} , \tag{4.7}$$

$$\hat{\beta} = 1 + \frac{2}{a_{xx}(c^{2\kappa}-1)}[\frac{a_{rx}+\kappa a_{\theta x}}{\kappa+1}c^{2\kappa} + \frac{a_{rx}-\kappa a_{\theta x}}{\kappa-1} - \frac{2\kappa(a_{rx}-a_{\theta x})}{\kappa^2-1}c^{\kappa-1}], \tag{4.8}$$

$$\hat{\gamma} = -\hat{\beta} , \tag{4.9}$$

$$\hat{\delta} = \frac{2}{E_2 a_{xx}^2}[\frac{h(a_{rx}+\kappa a_{\theta x})}{\kappa+1}\frac{(c^{\kappa}-c^{-1})^2}{1-c^{2\kappa}} + \frac{h(a_{rx}-\kappa a_{\theta x})}{\kappa-1}\frac{(1-c^{\kappa-1})^2}{1-c^{2\kappa}} \cdots - \frac{(a_{xx}-ha_{rx}-ha_{\theta x})(c^{-2}-1)}{2}] . \tag{4.10}$$

In equation (4.7) to (4.10), a_{mn} ($m,n = r,\theta,x$) are the elements of the compliance matrix of F^{2}MC cell wall at the laminate level (figure 2.1b, and Sun 1998). B_f is the effective bulk modulus of the working fluid, and c is the ratio of the inner cell radius to

outer cell radius: $c = a_i / a_o$. The constants h and κ can be calculated based on equations (3.8 to 3.10).

It is worth noting that the parameter $\hat{\beta}$ and $\hat{\gamma}$ are identical in value but opposite in sign. Later this relation will be used to explain the symmetry of the equivalent stiffness matrix.

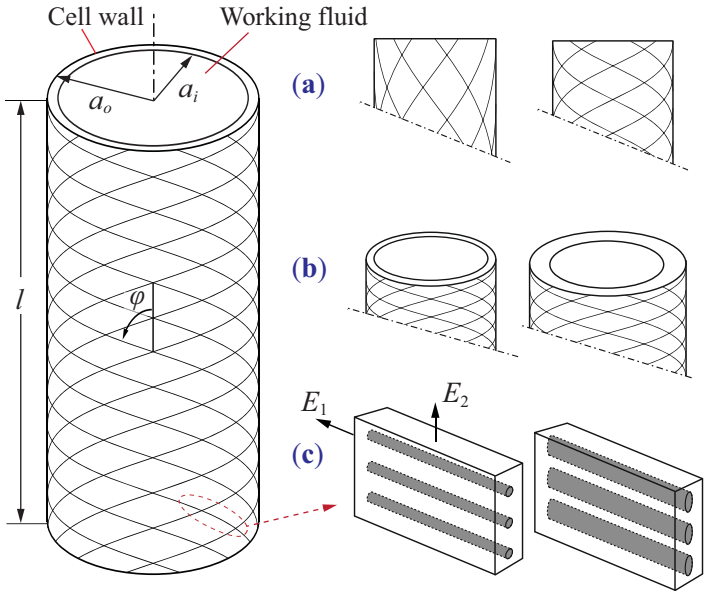

Figure 4.1 A schematic diagram of the construction of F^{2}MC cells with three important design variable groups: (**a**) fiber orientation φ; (**b**) cell wall thickness a_i/a_o, and (**c**) the ratio of elastic anisotropy E_1/E_2.

While the performance parameter formulations look complicated, they are essentially functions of three physical variables: the fiber angle φ, the cell wall thickness ratio a_i / a_o, and the level of elastic anisotropy E_1 / E_2 (figure 2.1c), these three physical variable are illustrated in figure 4.1. The only exception is $\hat{\alpha}$ since it also depends on the in-

verse of normalized fluid bulk modulus E_2/B_f. If our focus is on the F^{2}MC cellular structural design, we can assume the normalized bulk modulus a constant. The performance parameters cannot take any arbitrary values because they are determined by the physical variables, so it is necessary to calculate their range. Through numerical analysis, one can construct a three-dimensional mesh grid corresponding to the combinations of the three physical variables within their feasible range, and then calculate the performance parameters at each grid point to form a parametric space. Figure 4.2 illustrates the parametric space spanned by the performance parameters mapped from a physical variable mesh grid defined by $1^\circ \le \varphi \le 89^\circ$, $0.6 \le a_i/a_o \le 0.95$, and $50 \le E_1/E_2 \le 3000$ ($B_f/E_2 = 0.4$). This performance parametric space will be called Ω for simplicity.

Since the F^{2}MC cell is fabricated through a filament winding process, the fiber angle and cell wall thickness ratio can be tailored by programming the winding machine. The elastic anisotropy ratio can be tailored by selecting the fiber and resin materials with appropriate elastic stiffness, as well as by adjusting the fiber volume fraction.

The mapping from physical variables to Ω is non-linear, however it is a one-to-one, smooth mapping, so that each point within Ω corresponds to only one unique F^{2}MC physical design. This uniqueness can be verified by the non-zero Jacobian of the mapping, which can be calculated by a numerical difference scheme (Hubbard, 2006).

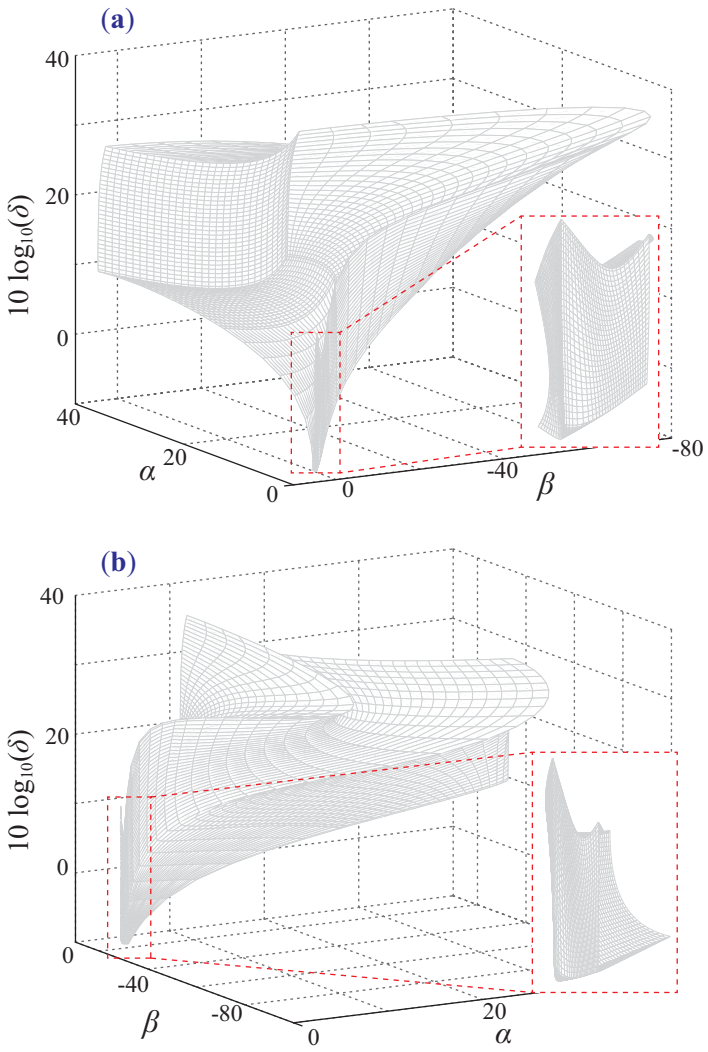

Figure 4.2 Performance parametric space Ω. (**a**, **b**): two equivalent plots but from different views. The surface grid reflects the discrete three-dimensional grid, which will be used in synthesis procedure. Part of Ω is blown up for a clearer view, and the complex geometry poses a challenge for developing the synthesis procedure. (The normalized fluid bulk modulus B_f/E_2 is assumed at 0.4)

4.1.2 Non-dimensional system governing equation

With the three characteristic units, one can derive the time unit as,

$$\tau = t \Big/ \sqrt{\frac{\rho a_i^2}{\pi E_2}} \,. \tag{4.11}$$

One can substitute the characteristic units into the end mass dynamic equation:

$$m(\frac{\pi E_2}{\rho a_i^2})\frac{\mathrm{d}^2(l_1\varepsilon_1 + l_2\varepsilon_2)}{\mathrm{d}\tau^2} + (\pi E_2 a_i^2)\hat{f}_2 = (\pi E_2 a_i^2)\hat{f}_e\,, \tag{4.12}$$

which can be simplified to,

$$\hat{m}\frac{\mathrm{d}^2\hat{x}}{\mathrm{d}\tau^2} + \hat{f} = \hat{f}_e\,, \tag{4.13}$$

where $\hat{m}$ is the normalized end mass ($\hat{m} = m/\rho a_i^3$), and $\hat{x}$ is the normalized displacement ($\hat{x} = \hat{\varepsilon}_1 + \hat{\varepsilon}_2$).

Similarly, one can substitute the characteristic units into the flow port dynamic equation,

$$I(\pi a_i^3)(\frac{\pi E_2}{\rho a_i^2})\frac{\mathrm{d}^2\hat{v}}{\mathrm{d}\tau^2} + R(\pi a_i^3)\sqrt{\frac{\pi E_2}{\rho a_i^2}}\frac{\mathrm{d}\hat{v}}{\mathrm{d}\tau} + E_2(\hat{p}_2 - \hat{p}_1) = 0\,, \tag{4.14}$$

which can be simplified into,

$$\hat{I}\frac{\mathrm{d}^2\hat{v}}{\mathrm{d}\tau^2} + \hat{R}\frac{\mathrm{d}\hat{v}}{\mathrm{d}\tau} + (\hat{p}_2 - \hat{p}_1) = 0\,, \tag{4.15}$$

where the non-dimensional flow port inertance and resistance can be calculated as,

$$\hat{I} = \frac{\pi^2 a_i}{\rho} I = \frac{\pi^2 a_i}{\rho}\frac{\rho l_f}{\pi a_f^2} = \frac{\pi l_f a_i}{a_f^2}\,, \tag{4.16}$$

$$\hat{R} = \frac{\pi^{3/2} a_i^2}{\sqrt{\rho E_2}} R \,, \tag{4.17}$$

where a_f and l_f are the radius and length of the flow port inertance tube, respectively.

Finally, one can combine the non-dimensional F^{2}MC cellular model, compatibility conditions as well as the two dynamic equations to derive the dimensionless system governing equation:

$$\begin{bmatrix} \hat{m} & 0 \\ 0 & \hat{I} \end{bmatrix} \frac{\mathrm{d}^2 \hat{\mathbf{X}}}{\mathrm{d}\tau^2} + \begin{bmatrix} 0 & 0 \\ 0 & \hat{R} \end{bmatrix} \frac{\mathrm{d}\hat{\mathbf{X}}}{\mathrm{d}\tau} + \begin{bmatrix} \hat{\mathbf{K}}_{11} & \hat{\mathbf{K}}_{12} \\ \hat{\mathbf{K}}_{21} & \hat{\mathbf{K}}_{22} \end{bmatrix} \hat{\mathbf{X}} = \begin{bmatrix} \hat{f}_e \\ 0 \end{bmatrix}, \quad \hat{\mathbf{X}} = \begin{bmatrix} \hat{x} \\ \hat{v} \end{bmatrix}, \tag{4.18}$$

where the detailed calculation of $\hat{\mathbf{K}}_{ij}$ will be discussed later. In the following, we will neglect the fluid viscous damping for simplicity; and this will not compromise the purpose of this chapter.

One can already see the benefits of dimensional analysis. The normalized stiffness matrix is now only a function of performance parameters of individual F^{2}MC cells, reducing the number of parameters involved. Furthermore, the definitions of the normalized mass and flow port inertance are combinations of the physical end mass, flow port dimension, and size of the F^{2}MC cells, so they can provide us with a principle of scaling should the F^{2}MC cellular structure need to be scaled for practical applications.

4.1.3 Experimental test

The experiment has two purposes. The first is to test the correlation between the cellular performance parameters and physical design variables as in equations (4.7 to 4.10); the second purpose is to test the derivation of the equivalent stiffness matrix in equation

(4.18). Two new F^{2}MC cell samples, with thicker cell wall than those in chapter 3, are fabricated by filament winding processes (AS4D carbon fiber and Reoflex 20 urethane rubber resin at 57% fiber volume ratio). The two samples have fiber angels of ±40° and ±70° respectively; a wall thickness ratio (a_i / a_o) of 0.78 and elastic anisotropic ratio (E_1 / E_2) of 2300.

To achieve the first purpose of the experiment, the performance parameters are directly measured from each individual F^{2}MC sample according to their physical meanings. For example, $\hat{\beta}$ is related to the internal volume change when the cell is subject to an axial strain, so the F^{2}MC sample, filled with working fluid, is loaded onto a tensile test machine (INSTRON® Model 1331). A graduated tube is attached to the upper end of the cell, and a camera monitors the position of the fluid meniscus inside of the graduated tube while the tensile test machine applies different strain levels (figure 4.3). Another performance parameter $\hat{\delta}$ is related to the longitudinal cell stiffness, so an F^{2}MC sample is attached to the shaker as shown in figure 4.4 (note that the F^{2}MC is kept empty to measure $\hat{\delta}$). A sweeping frequency input is applied to the end mass, and $\hat{\delta}$ can be calculated from the measured natural frequency ω_n as follows (figure 4.4a),

$$\hat{\delta} = \frac{mg\omega_n^2}{\pi a_i E_2}. \tag{4.19}$$

The third performance parameter $\hat{\alpha}$ is measure by the same set up in figure 4.4 but with F^{2}MC and end inertance tube filled with fluid. The system zero obtained from the sweeping frequency test is directly related to $\hat{\alpha}$ as follows (figure 4.4b),

$$\hat{\alpha} = \frac{E_2}{\pi a_i^3 g I_e} \frac{1}{\omega_z^2}. \tag{4.20}$$

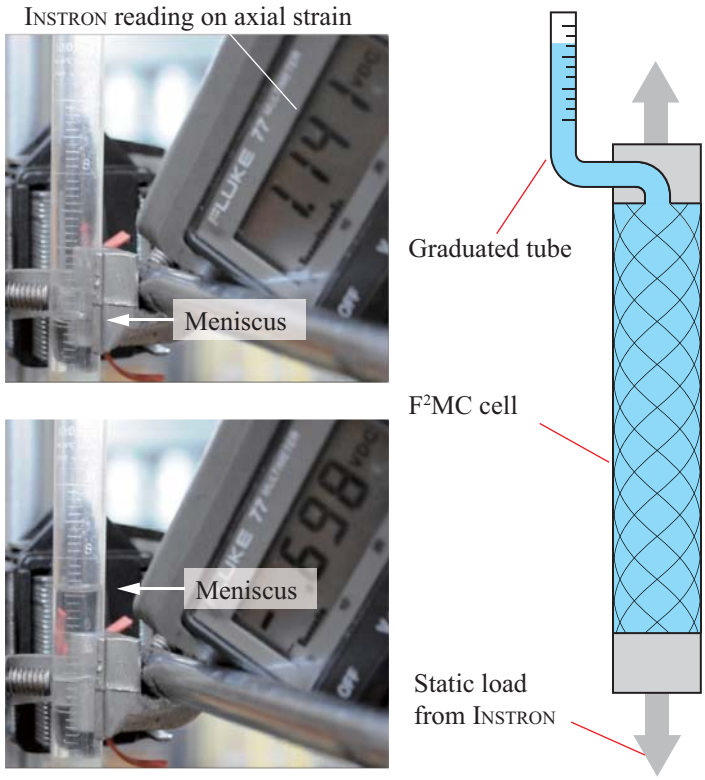

Figure 4.3 Experiment set up to measure the performance parameter β. The F²MC is filled with working fluid, and the camera monitories the change of the meniscus position inside of the graduated tube while Instron machine applies axial strain to the F²MC tube.

The values of the variables on the right hand side of equation (4.19) and (4.20) can be found in table 4.1, interested readers can refer to appendix D for the detailed derivation of these two equations. Table 4.2 summarizes the measured performance parameters and their corresponding theoretical prediction based on physical design variables; the predic-

tion is based on the Lekhnitskii's solution in equations (4.7 to 4.10). The prediction correlates well with the experiment data, so it is viable to utilize performance parameters in the system analysis and synthesis to simplify the mathematics derivation.

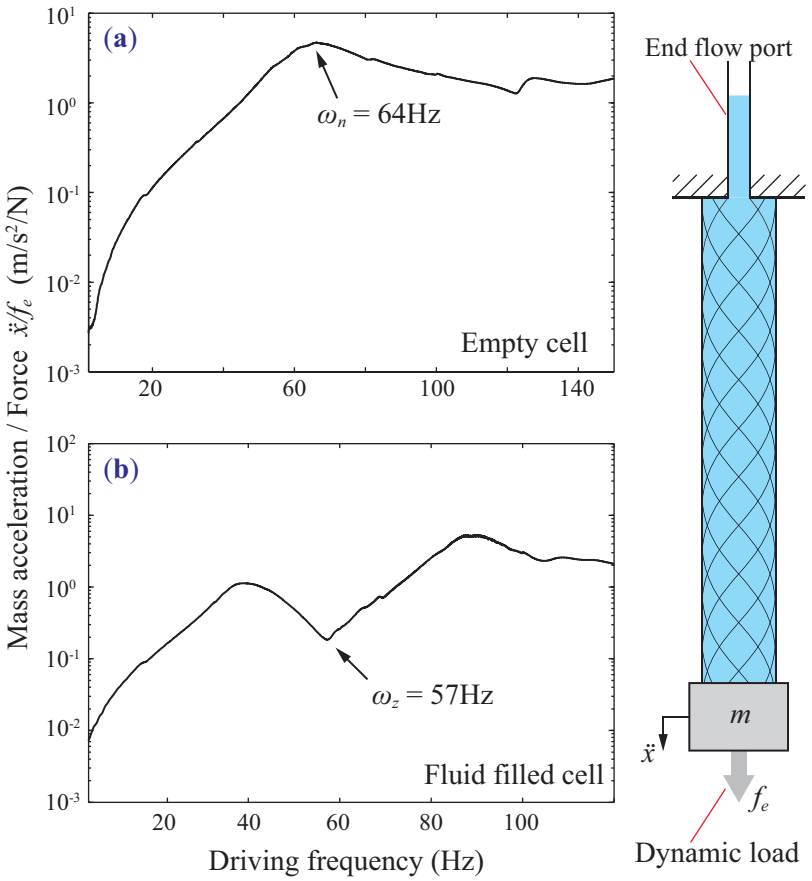

Figure 4.4 Experiment set up to measure δ and α. (**a**) The end mass dynamic response while the F^{2}MC is empty. The natural frequency ω_n is used to calculate δ. (**b**) The dynamic response of the same system except for a fluid filled F^{2}MC and external flow port. The zero ω_z is used to calculate α. The frequency response results are from the ±70°cell. Shaker: Ling Dynamics V408 series; accelerometer: PCB 532C04; force transducer: PCB 208C02.

Table 4.1 Some F^2MC sample design parameters and experiment setup to measure the individual cellular performance parameters.

End mass (m)	0.89kg
Ply modulus (E_2)	50MPa
F^2MC inner radius (a_i)	0.01m
Aspect ratio (g)	20
End port Inertance (I_e) (in kg/m^4)	2.28×10^6 (±40° tube) 4.57×10^6 (±70° tube)

Table 4.2 The measured performance parameters and their corresponding prediction.

	±40° tube		±70° tube	
	Measured	Predicted	Measured	Predicted
$\hat{a}$	1.75	1.47	1.43	1.45
$\ddot{\beta}$	-1.98	-2.20	0.84	0.83
$\hat{\delta}$	6.06	5.96	1.74	1.78

To test the derivation of the system governing equation, the two F^2MC samples are connected through an internal flow port to form a simple dual cellular structure (as shown in figure 3.1). Sweeping frequency test is conducted on this structure, and the measured system poles and zero matches well with the prediction based on the measured performance parameters from individual cells (figure 4.5). It is worth noting that the value of $\hat{\alpha}$, $\hat{\delta}$ is closely related to the elastic modulus of the F^2MC cell wall soft matrix material, which is frequency dependent. Therefore, frequency sweeping is used in $\hat{\alpha}$, $\hat{\delta}$ measurements and the dual cell test, so that the $\hat{\alpha}$, $\hat{\delta}$ values are consistent throughout the experiment results. Overall, the experiment result agree with the analytical modeling in terms of system poles and zero positions so it can be utilized in the synthesis procedure in the following sections.

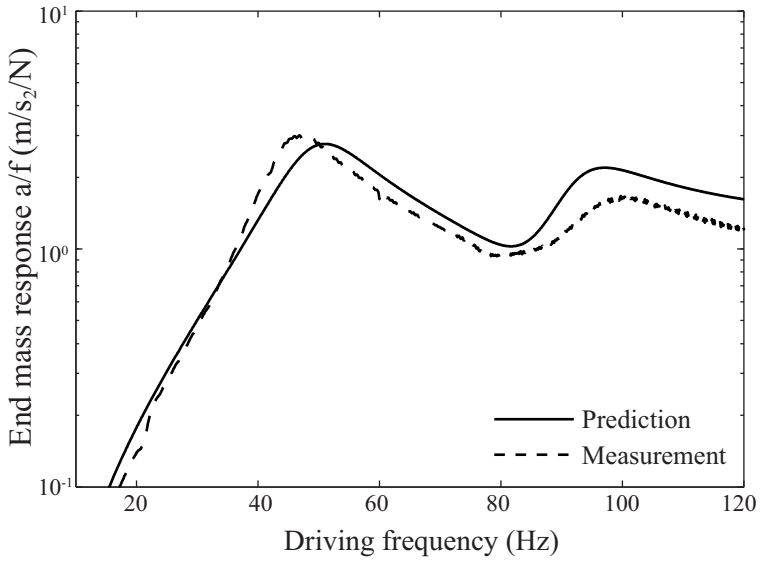

Figure 4.5 Measured dual cellular structure system poles and zero positions matches well with prediction. The inertance of the internal flow port is 3.1×10^6 kg/m^4. The modeling of cell wall damping and flow port resistance is adopted from chapter 3, and the value of the flow port resistance is back calculated from the experiment result.

4.2 Physical insights

In this section, the physical meaning of the elements of the normalized equivalent stiffness matrix $\left[\hat{\mathbf{K}}_{ij}\right]$ is discussed in detail.

4.2.1 Physical meaning of the equivalent stiffness matrix

The elements of the stiffness matrix $\left[\hat{\mathbf{K}}_{ij}\right]$ can be calculated based on the normalized F^{2}MC cellular parameters: $\hat{\alpha}_k$, $\hat{\beta}_k$, $\hat{\gamma}_k$, $\hat{\delta}_k$ and g, which are complicated expressions of the physical variables. A close investigation on the physical meanings of the stiffness matrix element will reveal the principle of how the overall structural dynamics is related to the performance of each individual F^{2}MC cell, as well as the difference between the cellular performances.

The first element of the equivalent stiffness matrix, $\hat{\mathbf{K}}_{11}$, can be calculated as follows,

$$\hat{\mathbf{K}}_{11} = \left(\frac{g\hat{\alpha}_1}{\hat{\alpha}_1\hat{\delta}_1 - \hat{\beta}_1\hat{\gamma}_1} + \frac{g\hat{\alpha}_2}{\hat{\alpha}_2\hat{\delta}_2 - \hat{\beta}_2\hat{\gamma}_2} \right)^{-1} = \left(\frac{1}{\hat{\mathbb{K}}_1} + \frac{1}{\hat{\mathbb{K}}_2} \right)^{-1} = \hat{\mathbb{K}}, \tag{4.21}$$

where $\hat{\mathbb{K}}_k$ is simply the normalized *closed valve stiffness* of the k^{th} F^{2}MC cell. The closed valve stiffness is defined as the individual F^{2}MC cell axial stiffness when the cell is filled with working fluid and the valves at both ends of the cell are closed (figure 2.2c). One can calculate the closed valve stiffness by setting $\hat{v}$ to zero in performance equations (4.5) and (4.6) and $\hat{\mathbb{K}}_k$ is the ratio of $\hat{f}_k$ over $\hat{\varepsilon}_k$. Therefore, $\hat{\mathbf{K}}_{11}$ is the equivalent stiffness of the two F^{2}MC cells connected in series when both are in closed valve state.

This claim of the physical meaning of $\hat{\mathbf{K}}_{11}$ can be validated by the normalized system governing equation as well, if one only considers the static response, the first row of governing equation (4.18) can be simplified to:

$$\hat{\mathbf{K}}_{11}\hat{x} + \hat{\mathbf{K}}_{12}\hat{v} = \hat{f}_e, \tag{4.22}$$

$$\hat{\mathbf{K}}_{21}\hat{x} + \hat{\mathbf{K}}_{22}\hat{v} = 0. \tag{4.23}$$

In these two equations, setting both F^{2}MC cells to the closed valve state is equivalent to setting the flow port flow $\hat{v}$ to zero as if the port is blocked, then the mechanical force balance in (4.22) is reduced to $\hat{\mathbf{K}}_{11}\hat{x} = \hat{f}_e$, which gives $\hat{\mathbf{K}}_{11}$ the same physical meaning as mentioned above.

The element $\hat{\mathbf{K}}_{21}$ in the normalized stiffness matrix can be calculated as,

$$\hat{\mathbf{K}}_{21} = \hat{\mathbf{K}}_{11}\left(\frac{\hat{\beta}_2}{\hat{\beta}_2\hat{\gamma}_2 - \hat{\alpha}_2\hat{\delta}_2} - \frac{\hat{\beta}_1}{\hat{\beta}_1\hat{\gamma}_1 - \hat{\alpha}_1\hat{\delta}_1}\right) = \hat{\mathbf{K}}_{11}\left(\hat{\mathbb{P}}_2 - \hat{\mathbb{P}}_1\right) = \hat{\mathbf{K}}_{11}\hat{\mathbb{P}}, \tag{4.24}$$

where $\hat{\mathbb{P}}_k$ is the correlation between the axial load and internal pressure rise for an individual F^{2}MC cell in the closed valve state, one can calculate $\hat{\mathbb{P}}_k$ by setting $\hat{v}$ to zero in performance equations (4.5) and (4.6), and $\hat{\mathbb{P}}_k = \hat{p}_k / \hat{f}_e$. Substituting in the previous definition of $\hat{\mathbf{K}}_{11}$, $\hat{\mathbf{K}}_{21}$ can be defined as,

$$\hat{\mathbf{K}}_{21} = \frac{\hat{p}_2 - \hat{p}_1}{\hat{x}}, \ (\hat{v} = 0). \tag{4.25}$$

Therefore, the element $\hat{\mathbf{K}}_{21}$ describes the *difference* of pressure rise between the two closed valve F^{2}MC cells when they are connected in series and subjected to the same axial load.

The $\hat{\mathbf{K}}_{12}$ element in the normalized stiffness matrix can be calculate as,

$$\hat{\mathbf{K}}_{12} = \hat{\mathbf{K}}_{11}\left(\frac{\hat{\gamma}_1}{\hat{\beta}_1\hat{\gamma}_1 - \hat{\alpha}_1\hat{\delta}_1} - \frac{\hat{\gamma}_2}{\hat{\beta}_2\hat{\gamma}_2 - \hat{\alpha}_2\hat{\delta}_2}\right). \tag{4.26}$$

Given the fact that $\hat{\beta}$ and $\hat{\gamma}$ are same in amplitude but opposite in sign, $\hat{K}_{12}$ is identical to $\hat{K}_{21}$, making the stiffness matrix symmetric.

With these physical meanings of $\hat{\mathbf{K}}_{12}$ and $\hat{\mathbf{K}}_{21}$, some previous observations by the authors become clear to explain. In chapter 3 the two F^{2}MC cells had the same wall thickness (a_i / a_o) and anisotropic ratio (E_1 / E_2). It was shown that when the two cells have the same fiber angle, $\hat{\mathbf{K}}_{12}$ and $\hat{\mathbf{K}}_{21}$ becomes zero so that the system dynamics is reduced to a single degree of freedom mass spring oscillator. Now it becomes clear that, when the

two cells have the same fiber angle, their internal pressure rise is the same, so no flow can be generated through the flow port. As a result, the fluidic dynamics will not show up in the system response.

The $\hat{\mathbf{K}}_{22}$ element in the normalized stiffness matrix can be calculated as,

$$\hat{\mathbf{K}}_{22} = \hat{\mathbf{K}}_{21} \frac{(\hat{\beta}_1 - \hat{\beta}_2)(\hat{\gamma}_1 - \hat{\gamma}_2) - (\hat{\alpha}_1 + \hat{\alpha}_2)(\hat{\delta}_1 + \hat{\delta}_2)}{\hat{\beta}_1(\hat{\alpha}_2\hat{\delta}_2 - \hat{\beta}_2\hat{\gamma}_2) - \hat{\beta}_2(\hat{\alpha}_1\hat{\delta}_1 - \hat{\beta}_1\hat{\gamma}_1)} = -\hat{\mathbf{K}}_{21}\hat{\mathbb{Q}}\,. \tag{4.27}$$

One can substitute the derivation of $\hat{\mathbf{K}}_{22}$ into (4.23) to show that $\hat{x} = \hat{\mathbb{Q}}\hat{v}$. Therefore $\hat{\mathbf{K}}_{22}$ describes the amount of static fluid flow displacement through the flow port between the two F^{2}MC cells when the cell string is subject to axial strain.

4.2.2 Correlating physical parameters to structural dynamics

With the physical insights on the F^{2}MC cellular structure, one can update the governing equation of motion (4.18) to quantitatively correlate the cellular performance to the system poles and zero position:

$$\begin{bmatrix} \hat{m} & 0 \\ 0 & \hat{I} \end{bmatrix} \frac{\mathrm{d}^2\hat{\mathbf{X}}}{\mathrm{d}\tau^2} + \hat{\mathbb{K}} \begin{bmatrix} 1 & \hat{\mathbb{P}} \\ \hat{\mathbb{P}} & -\hat{\mathbb{P}}\hat{\mathbb{Q}} \end{bmatrix} \hat{\mathbf{X}} = \begin{bmatrix} \hat{f}_e \\ 0 \end{bmatrix}, \tag{4.28}$$

The system poles are the roots of the corresponding characteristic equation:

$$\hat{m}\hat{I}\hat{\omega}^4 + \hat{\mathbb{K}}(\hat{m}\hat{\mathbb{P}}\hat{\mathbb{Q}} - \hat{I})\hat{\omega}^2 - \hat{\mathbb{K}}^2\hat{\mathbb{P}}(\hat{\mathbb{P}} + \hat{\mathbb{Q}}) = 0\,, \tag{4.29}$$

And the zero is square of the natural frequency of the system when the end mass is fixed to the ground:

$$\hat{\omega}_z^2 = -\hat{\mathbb{K}}\hat{\mathbb{P}}\hat{\mathbb{Q}}/\hat{I}\,, \tag{4.30}$$

4.3 Synthesize the cellular structure

Structural system synthesis is, in essence, the inverse problem to analysis. That is, to find the appropriate cellular structure designs based on given poles and zero positions (spectral data). Synthesis is a valuable tool not only because it helps us find appropriate cellular structure design for target performance, but also because it provides us with the limit of achievable spectral data and thus quantitatively demonstrates the potential of the cellular structure. For example, if the cellular structure is used as a vibration absorber, one can use the synthesis tool to find out the achievable range of absorption frequency (zero), and come up with a structure design that precisely place the absorption frequency at the desired location.

In this section, the synthesis tool and process is presented in detail, and several sample results are discussed.

4.3.1 Definition of the synthesis problem

Since dynamic response of a dual cellular F^{2}MC structure features two system poles (ω_{p_1} and ω_{p_2}, $\omega_{p_1} < \omega_{p_2}$) and one system zero ($\omega_z$), one can utilize the physical insights revealed in the previous section to calculate the correlation between the performance parameters for each F^{2}MC cell based on given target,

$$\hat{\alpha}_2 = \frac{S_1[g\hat{\alpha}_1 - (\hat{\alpha}_1\hat{\delta}_1 + \hat{\beta}_1^2)S_1]}{\Delta}, \tag{4.31}$$

$$\hat{\beta}_2 = -\frac{gS_1[\hat{\beta}_1 - (\hat{\alpha}_1\hat{\delta}_1 + \hat{\beta}_1^2)S_2]}{\Delta}, \tag{4.32}$$

$$\hat{\delta}_2 = \frac{g[gS_2(\hat{\beta}_1^2 + \hat{\alpha}_1\hat{\delta}_1)(S_2 + S_3) + \hat{\delta}_1 S_1]}{\Delta}. \tag{4.33}$$

$$\Delta = \hat{\delta}_1 S_1^2 + g^2\hat{\alpha}_1 S_2(S_2 + S_3) + gS_1[2\hat{\beta}_1 S_2 + S_2 S_3(\hat{\beta}_1^2 + \hat{\alpha}_1\hat{\delta}_1) - 1], \tag{4.34}$$

where parameter S_k are: $S_1 = \left[M\left(\omega_{p_1}^2 + \omega_{p_2}^2 - \omega_z^2\right)\right]^{-1}$, $S_2 = S_1\sqrt{\hat{I}\hat{M}(\omega_{p_2}^2 - \omega_z^2)(\omega_z^2 - \omega_{p_1}^2)}$, and $S_3 = \omega_z^2 \hat{I} S_1 / S_2$. Equation (4.31) to (4.33) illustrate the benefit of working with the performance parameters rather than physical variables, because now the relation between the two cells is of much simpler algebraic form. Furthermore, they show that for a given F^{2}MC cell #1 design, there exits only one unique cell #2 design corresponding to the target poles and zero. With these relations, the synthesis problem can be defined as follows:

> Given a target system poles and zero position $\left(\omega_{p_1} < \omega_z < \omega_{p_2}\right)$, find any pairs of performance parameter triples for the two F^{2}MC cells: $\Psi_1 = \left[\hat{\alpha}_1 \;\; \hat{\beta}_1 \;\; \hat{\delta}_1\right]$ and $\Psi_2 = \left[\hat{\alpha}_2 \;\; \hat{\beta}_2 \;\; \hat{\delta}_2\right]$ respectively, such that both $\Psi_1, \Psi_2 \in \Omega$ as in figure 4.2 (so that they are physically feasible), and equations (4.31) to (4.34) hold valid (so that they can provide the target performance).

4.3.2 Synthesis procedure

The synthesis process can be illustrated by a flow chart in figure 4.6. It can be described as a numerical survey. First, a three-dimensional grid mesh of $\Psi_1 = \left[\hat{\alpha}_1 \;\; \hat{\beta}_1 \;\; \hat{\delta}_1\right]$ is constructed to span the parametric space Ω. Secondly, the iteration loop (steps 3-4-5) is executed onto each point in the Ψ_1 mesh, so that for each cell #1 design, the corresponding cell #2 design candidate is calculated based on the target poles and zero position (step 4), and then this cell #2 design candidate is checked for physical feasibility (step 5).

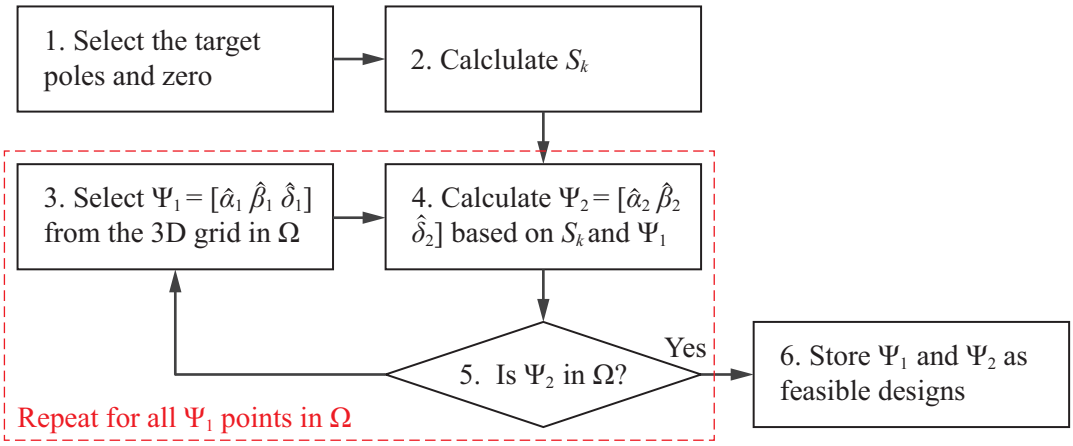

Figure 4.6 Flow chart for the synthesis procedure.

To determine whether the candidate Ψ_2 lies within Ω is not trivial because of its complicated geometry. One can compare the position of candidate Ψ_2 relative to the six boundary surfaces of Ω in the $\hat{\alpha}$ - $\hat{\beta}$ - $\hat{\delta}$ parametric space. Since each boundary surface separates the space into two sides: one side contains Ω and the other side does not. The candidate Ψ_2 can be determined to lie inside of Ω if it locates on the side containing Ω for all 6 boundary-surfaces. To do this in the numerical script, one can first extract the mesh point coordinates of these boundary surfaces (noted as $\partial\Omega_i$, $i = 1...6$, see figure 4.7). Then the surface normal vector of $\partial\Omega_i$ at each mesh point can be calculated numerically (such as using the "`surfnorm`" command in MATLAB®), where the norm vectors are directed into Ω. For a candidate Ψ_2 triple, one can find the mesh point on $\partial\Omega_i$ with the closest distance to Ψ_1 (point O in figure 4.7), and then calculate the scalar product of the norm vector at point O and the position vector $\overrightarrow{O\Psi_2}$. Ψ_2 is considered to be locate on the side containing Ω if the scalar produce is greater than zero.

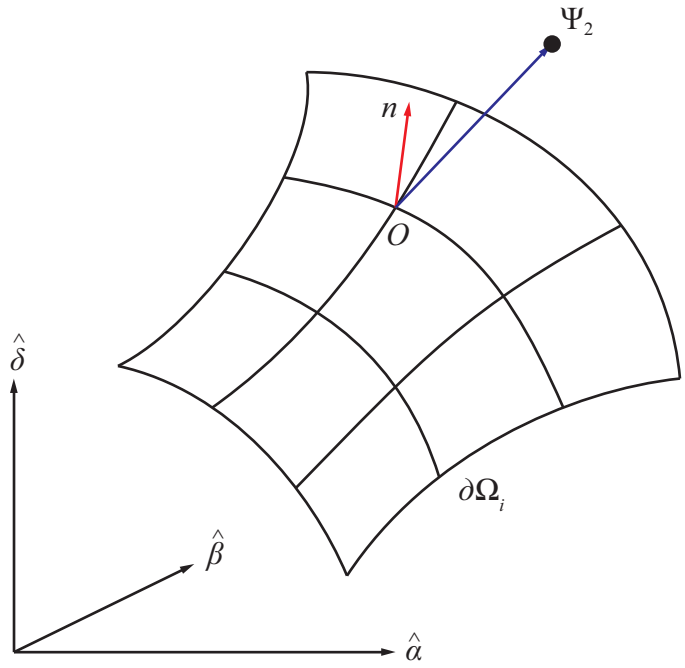

Figure 4.7 Illustration of step 5 in the synthesis flow chart. The boundary surface $\partial\Omega_i$ here is determined by 16 mesh points, and point O is the closest to candidate Ψ_2. n is the surface norm pointing into Ω. In this case, Ψ_2 locates on the side containing Ω.

4.3.3 A synthesis case study

This section presents a synthesis example result for the target poles at 60 and 90Hz, and zero at 70Hz. Figure 4.8 demonstrates the feasible cell #1 design in the performance parametric space, and figure 4.9 demonstrates the corresponding cell #2 designs (several other parameters are listed in table 4.3). The analysis is based on a 50×50×50 mesh grid in Ω for cell #1. Due to the nature of numerical simulation, the feasible designs appear to be groups of discrete points, however, these points reflect the position and boundary of a *continuous* feasible design sub-space in Ω since equations (4.31-4.34) is continuous and invertible. One can translate the feasible designs back into the physical variables by an inverse mapping of equations (4.7) - (4.10).

Table 4.3 Several parameters in the synthesis case study.

Mass (M)	200	F^2MC inner radius (ai)	0.01m
Port Inertance (I)	251.3	Aspect ratio (g)	20
Ply modulus (E_2)	50MPa	Time unit (τ)	2.52×10^{-5}s

Table 4.4 Two sample synthesis results.

Cell # 1 Design			Cell # 2 Design		
Fiber Angle	E_1/E_2 Ratio	Thickness Ratio	Fiber Angle	E_1/E_2 Ratio	Thickness Ratio
46.2°	1976	0.93	45.2°	64	0.67
28.6°	857	0.68	62.5°	103	0.84

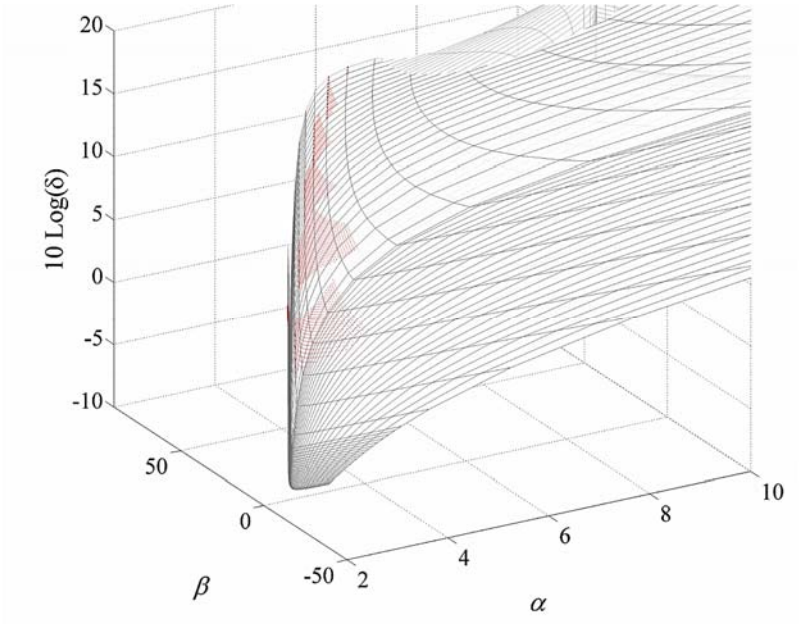

Figure 4.8 Synthesis results for cell #1. The target poles and zero position is at 60Hz, 90Hz, and 70Hz. Each red point represents a feasible design. And the outlining parametric space is the close up view of figure 4.2b.

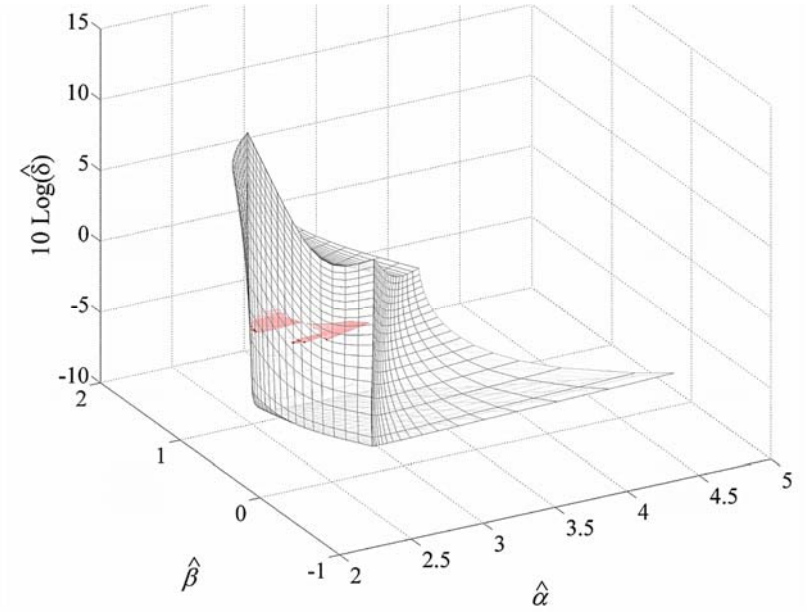

Figure 4.9 Synthesis results for cell #2. The target poles and zero position are 60Hz, 90Hz, and 70Hz. The outlining parametric space is from figure 4.2a.

Figure 4.10 illustrates the design space in figure 4.8 translated into the physical variable domain. In this particular case, there are two separate design spaces: one represented by the red points with cell #1 fiber angle less than 50°, the other represented by the green points with angle larger than 50°. The three dimensional shape of these design spaces provide practical guidelines for mechanical designers. For example, the second design space ($\varphi > 50^{\circ}$) is relatively insensitive to variations in fiber angle, because the shape of this space is almost parallel to the fiber angle axis. Therefore, engineers can choose designs in this space if the fiber angle of the F^2MC cell might be not accurately controlled.

Table 4.4 outlines two sample cellular physical designs from figure 4.8 and 4.9. One point worth noting is that for the first design, the fiber angles of the two F^2MC cells are very close. In chapter 3, the wall thickness and anisotropic ratio is assumed the same between the two F^2MC cells, so the two cells need to have different fiber angles in order

to actuate the internal fluid dynamics to exhibit the two-degrees-of-freedom oscillation response. However, the new synthesis tool shows that the difference of cell wall thickness and anisotropic ratio could also induce a pressure differential effect even with similar fiber orientations.

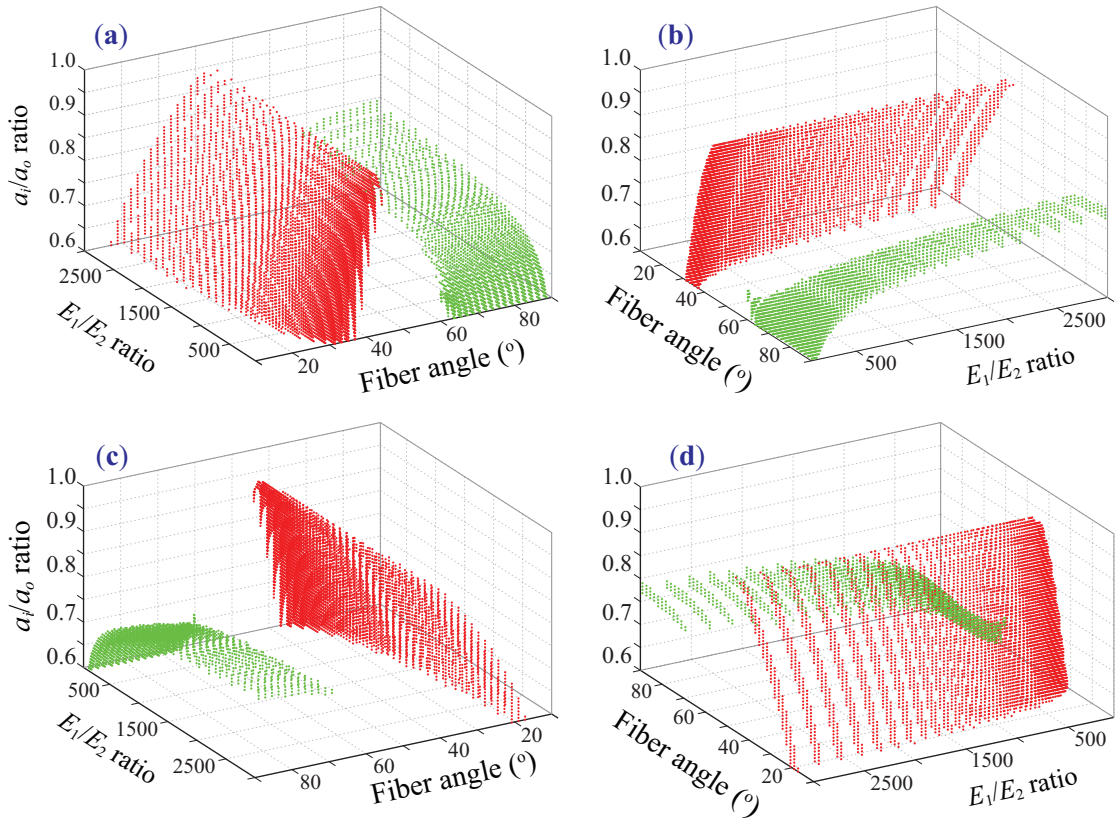

Figure 4.10 Synthesis results for cell #1 in terms of physical design variables. (**a** to **d**) The same plot viewing from four different perspectives with 90° increment. The target poles and zero position are at 60, 90 and 70Hz, respectively. One can see two separate design spaces, one with fiber angle smaller than 50° (red), and one with fiber angle bigger than 50° (green).

Figure 4.11a is a heat map demonstrating the achievable pole positions when the system zero is fixed at 70 Hz. The heat map color represents the number of feasible designs

based on the same 50×50×50 mesh grid in Ω as in the previous case study. In figure 4.11a, there is a 'hot ridge' corresponding to the target poles with a relatively large design space. A similar 'hot spot' can be seen in the heat map corresponding to the system zero fixed at 70 Hz (figure 4.11b). And the transparent region in the heat map corresponds to un-achievable target pole positions.

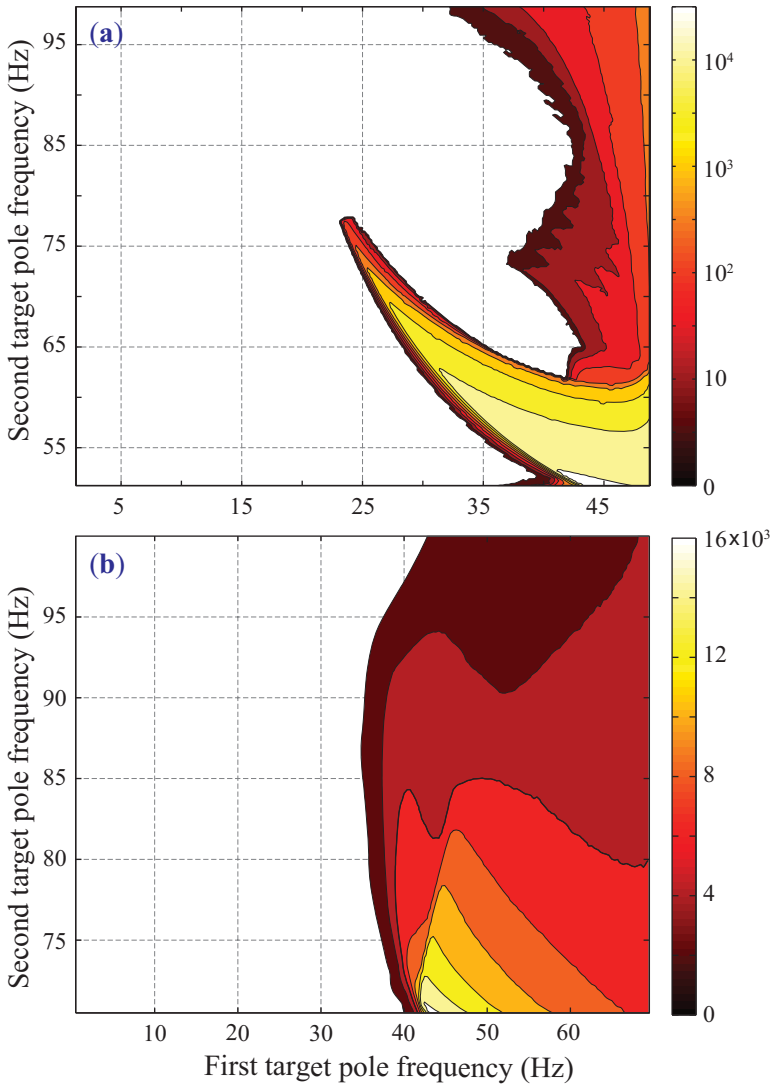

Figure 4.11 The achievable pole positions with different zero target: (**a**) 50Hz and (**b**) 70Hz. The heat map represents the number of feasible designs out of the 50×50×50 mesh grid in Ω.

4.4 Summary

In this chapter, a non-dimensional dynamic model is derived for a dual F^2MC cellular structure. Based on this model, the physical meaning of the equivalent stiffness matrix is investigated to reveal the missing linkage between individual cell performances to the overall structure dynamics. It is concluded that the dynamics of the cellular structure is directly correlated to three factors: the closed valve stiffness of the individual F^2MC cell, the difference of internal pressure rise between the cell, as well as the volume of static fluid displacement through the flow port. Such observations offer the physical insight that are lacking in the preliminary study of chapter 3, they are also valuable to understand more complicated system with larger number of cells and sophisticated architecture layout.

Furthermore, based on the non-dimensional model, three performance parameters are identified for each individual cell. Working with these parameters, rather than a large number of physical variables, can significantly simplify the mathematical derivation. They are investigated and experimentally tested for their physical meanings, value ranges, as well as their correlation to the system spectral data. These non-dimensional performance parameters can be a rigorous analytical tool not only for this thesis research, but also for other F^2MC related engineering development as well.

A synthesis procedure is then developed based on these parameters and the non-dimensional model. Synthesis results revealed that the F^2MC based dual string cellular structure can achieve a wide range of spectral data targets. It is also revealed that for each set of achievable spectral data, there exist multiple F^2MC designs, forming a design space. Such design versatility offers great freedom for the engineers to incorporate other consid-

erations into the structure synthesis, so that the F^2MC based cellular structure can be tailored for a variety of applications. This advantage will be exploited in the more sophisticated synthesis procedure in the following chapters.

While the studies presented in this chapter focus only on a dual F^2MC-cell string structure, the principles and results will become the building blocks for future multiple cellular structure investigations in the following chapter.

Chapter 5
Multi-Cellular String Structure Synthesis

In this chapter, the synthesis effort is extended on a multi-cellular "string" structure with at least three F^2MC cells connected by an internal fluid circuit. The spectral data is again the synthesis target, because they are closely related to the dynamic structural functions. The synthesis procedure from chapter 4 is only tailored towards dual cellular structure, and it does not apply to structures with a larger number of cells. Especially, in the dual cellular system, there exists a closed form analytical relation between the two F^2MC performance parameters (equation 4.31-34), but such closed form relation no longer exists when the cell number exceeds two. Therefore, the mathematical problem behind triple cell synthesis is fundamentally different from the dual cell synthesis and more challenging, requiring a brand new synthesis procedure. This new procedure relies on the generalized dynamic model, which is applicable to a string structure with any number of cells; and it attempts to tackle the complexity of the problem by integrating two ingredients together: one is genetic algorithm with discrete variables, and the other is the Jacobi inverse eigenvalue problem solver (JIEP). Synthesis case studies are presented for a F^2MC based triple cellular structure, and the advantages and limitations of this procedure are discussed.

5.1 Multi-cellular structure analytical model

Figure 5.1 illustrated the proposed multi-cellular string structure for investigation, which is essentially a string of F^{2}MC cells with different properties. All of the cells are connected through internal flow ports (inertance tubes).

5.1.1 Performance of the individual cell

The free body diagram in figure 5.1b shows that each F^{2}MC cell is subjected to two loads: axial force (f_k), and the net fluid flow (v_k^{net}) through flow ports connected to this cell ($v_k^{net} = v_k - v_{k+1}$ where v_k is the volume of fluid flow passing through flow port #*k*). These two load factors will consequently change the two system states: the axial strain (ε_k) and internal fluid pressure (p_k). The correlation between these loads and system states is crucial in the analysis because it describes the anisotropic elasticity of the cell wall as well as the coupling between structural deformation and fluid flow. It can be summarized as follows,

$$v_k - v_{k+1} = g\alpha_k p_k + \beta_k \varepsilon_k, \tag{5.1}$$

$$f_k = -\beta_k p_k + \delta_k \varepsilon_k / g, \tag{5.2}$$

where the aspect ratio $g = l / a_i$ is related to the shape of the F^{2}MC cell, and the variables α_k, β_k, and δ_k are the "performance parameters" of cell #*k* as defined in the previous chapter. Unless specially noted, all of the variables from now on are in their dimensionless form and thus the over hat above the dimensionless variables are dropped for simplicity.

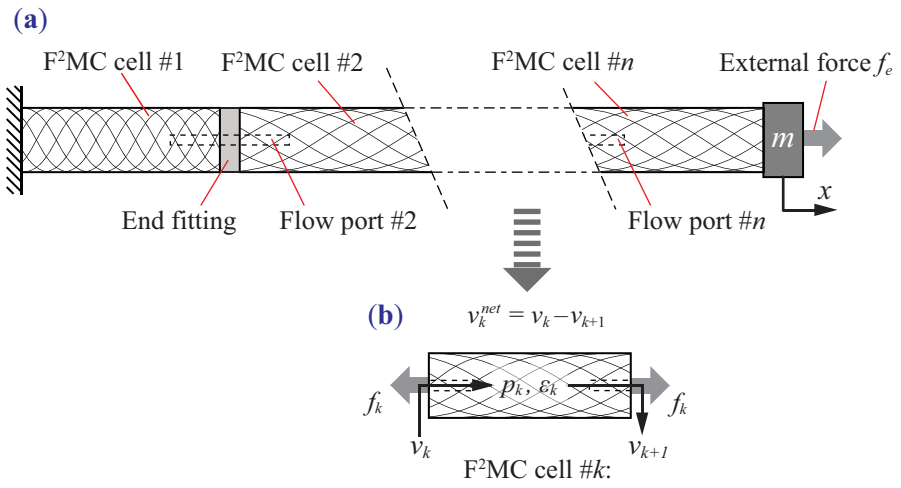

Figure 5.1 Illustration of the multi-cellular string structure. (**a**): The schematic diagram of the whole structure and (**b**) the free body diagram of an individual cell. Positive f_k means tension force, and positive v_k follows the direction shown by its arrow.

5.1.2 Principles of cellular interaction

The F²MC cells are directly connected through end fitting, and the working fluid are allowed to flow from one cell to another through flow ports (inertance tubes). Therefore, the interactions between adjacent cells are based on mechanical and fluidic principles. Out of the mechanical principle there is the physical condition stating the internal force balance between adjacent cells:

$$f_1 = f_2 = \ldots = f_n. \tag{5.3}$$

Out of fluidic principles there is the flow port equation, describing the dynamic fluid flow through flow port due to the pressure difference between adjacent cells:

$$I_k \frac{\partial v_k}{\partial \tau^2} + \left(p_k - p_{k-1}\right) = 0, \quad k = 2...n, \tag{5.4}$$

where I_k is the normalized flow port inertance.

5.1.3 System level derivation

The proposed cellular structure is a closed fluidic system so that the working fluid is only allowed to flow between the cells, but not flow in or out of the whole structure; therefore one can apply the fluidic boundary condition as:

$$v_1 = v_{n+1} = 0. \tag{5.5}$$

One can combine the fluidic equations (5.1 and 5.5) and the structural equations (5.2 and 5.3) as follows:

$$\sum_{k=1}^{n} \left(g\alpha_k p_k + \beta_k \varepsilon_k \right) = 0, \tag{5.6}$$

$$-\beta_k p_k + \delta_k \varepsilon_k / g = -\beta_j p_j + \delta_j \varepsilon_j / g, \quad k \neq j. \tag{5.7}$$

With some mathematical manipulation, equations (5.5-7) can be combined into one equation as follows:

$$p_k = \frac{\delta_k}{\beta_k}\frac{\varepsilon_k}{g} + \frac{1}{\Pi\beta_k}\sum_{j=1}^{n}\left(\beta_j + \frac{\alpha_j}{\beta_j}\delta_j \right)\frac{\varepsilon_j}{g}, \quad \text{where } \Pi = \sum_{j=1}^{n}\left(-\frac{\alpha_j}{\beta_j} \right). \tag{5.8}$$

Denote the strain vector $\mathbf{e} = \left[\varepsilon_1,\ \varepsilon_2,\ \cdots,\ \varepsilon_n \right]^\top$ and the normalized pressure vector $\mathbf{p} = \left[p_1,\ p_2,\ \cdots,\ p_n \right]^\top$, equation (5.8) can be written as a matrix form as,

$$\mathbf{p} = \mathbf{\Phi e}, \quad \text{where } \mathbf{\Phi}_{ij} = \frac{1}{g\Pi\beta_i}\left(\frac{\alpha_j}{\beta_j}\delta_j + \beta_j + \Delta_{ij}\delta_j\Pi \right), \tag{5.9}$$

where Δ_{ij} is the Kronecker delta. Denote the fluid volume vector $\mathbf{v} = \left[v_2,\ v_3,\ \cdots,\ v_n\right]^\top$, one can re-write equations (5.1) and (5.5) into matrix forms as,

$$\begin{aligned}\mathbf{v} &= g\begin{bmatrix} 0 & \alpha_2 & \alpha_3 & \cdots & \alpha_{n-1} & \alpha_n \\ & 0 & \alpha_3 & \cdots & \alpha_{n-1} & \alpha_n \\ & & 0 & \ddots & & \vdots \\ & & & \ddots & \alpha_{n-1} & \alpha_n \\ 0 & & & & 0 & \alpha_n \end{bmatrix}\mathbf{p} + \begin{bmatrix} 0 & \beta_2 & \beta_3 & \cdots & \beta_{n-1} & \beta_n \\ & 0 & \beta_3 & \cdots & \beta_{n-1} & \beta_n \\ & & 0 & \ddots & & \vdots \\ & & & \ddots & \beta_{n-1} & \beta_n \\ 0 & & & & 0 & \beta_n \end{bmatrix}\mathbf{e} \\ &= \mathbf{A}\mathbf{p} + \mathbf{B}\mathbf{e}.\end{aligned} \tag{5.10}$$

Substituting (5.9) into (5.10), one can write $\mathbf{v} = \boldsymbol{\Psi}\mathbf{e}$, where $\boldsymbol{\Psi} = \mathbf{A}\boldsymbol{\Phi} + \mathbf{B}$ is an (n−1)×n matrix, then one can substitute this into the flow port dynamic equation (5.4) as follows,

$$\begin{bmatrix} I_2 & & 0 \\ & \ddots & \\ 0 & & I_n \end{bmatrix}\boldsymbol{\Psi}\ddot{\mathbf{e}} + \begin{bmatrix} \boldsymbol{\Phi}_2 - \boldsymbol{\Phi}_1 \\ \vdots \\ \boldsymbol{\Phi}_n - \boldsymbol{\Phi}_{n-1} \end{bmatrix}\mathbf{e} = \mathbf{0}. \tag{5.11}$$

where $\boldsymbol{\Phi}_i$ is the i^{th} row of the matrix $\boldsymbol{\Phi}$. Finally, the end mass dynamic equation is:

$$m\ddot{x} + f_n = f_e \qquad (x = \varepsilon_1 + \varepsilon_2 + \ldots \varepsilon_n), \tag{5.12}$$

where f_e is the normalized external force on the end mass. Choose $\mathbf{X} = \left[x,\ v_2,\ \cdots,\ v_n\right]^\top$ as the system state vector, the system governing equation can be written as follows,

$$\mathbf{M}\ddot{\mathbf{X}} + \mathbf{K}^*\mathbf{T}^{-1}\mathbf{X} = \mathbf{F}_e, \tag{5.13}$$

where

$$\mathbf{M}=\begin{bmatrix} m & & & 0 \\ & I_2 & & \\ & & \ddots & \\ 0 & & & I_n \end{bmatrix},\ \mathbf{K}^*=\begin{bmatrix} \delta_n\Phi_n+\mathbf{a} \\ \Phi_2-\Phi_1 \\ \vdots \\ \Phi_n-\Phi_{n-1} \end{bmatrix},\ \mathbf{T}=\begin{bmatrix} \mathbf{b} \\ \boldsymbol{\Psi} \end{bmatrix},\ \text{and}\ \mathbf{F}_e=\begin{bmatrix} f_e \\ 0 \\ \vdots \\ 0 \end{bmatrix}, \quad (5.14a,b,c,d)$$

where $\mathbf{a}=\begin{bmatrix}0 & \cdots & 0 & \delta_n/g\end{bmatrix}$ and $\mathbf{b}=\begin{bmatrix}1 & \cdots & 1\end{bmatrix}$ are both $1\times$ n vectors. Based on equation (5.14), the dynamic response of the F^{2}MC based multi-cellular structure can be described as an *n* degrees of freedom mass-spring oscillator, where the inertia elements come from the end mass and the flow port inertance (there is one mass and *n*-1 flow ports), and the spring elements come from the cell wall anisotropic elasticity and fluid bulk modulus. Denote the system equivalent stiffness matrix as $\mathbf{K}=\mathbf{K}^*\mathbf{T}^{-1}$, the set of system poles $\{\lambda_i\}_{i=1}^{n}$ can be calculated as follows,

$$\{\lambda_i\}_{i=1}^{n}=\sigma\left(\mathbf{M}^{-1/2}\mathbf{K}\mathbf{M}^{-1/2}\right), \quad (5.15)$$

where "$\sigma(\cdot)$" is the operation of calculating matrix eigenvalues. The set of system zeros $\{\mu_j\}_{j=1}^{n-1}$ can be calculated as,

$$\{\mu_j\}_{j=1}^{n-1}=\sigma\left(\bar{\mathbf{M}}^{-1/2}\bar{\mathbf{K}}\bar{\mathbf{M}}^{-1/2}\right), \quad (5.16)$$

where $\bar{\mathbf{M}}$ and $\bar{\mathbf{K}}$ are the principal sub-matrix of **M** and **K** without their first column and row. In other words, the zeros of the multi-cellular structure as shown in figure 5.1 is equivalent to the poles of the system when the end mass is grounded.

5.1.4 Physical insight of the stiffness matrix

The system equivalent stiffness matrix $\mathbf{K} = \mathbf{K}^{*}\mathbf{T}^{-1}$ is a dense, symmetric $n \times n$ matrix. It has no trivial elements except when there are identical cells in the structure. The physical meaning of the elements in this matrix reveals the correlation between the individual cell performance and the overall structure spectral data.

The expression for the first element of the stiffness matrix, $\mathbf{K}_{11}$ in equation (5.14) can be re-organized as follows,

$$\mathbf{K}_{11} = \left(\mathbb{K}_1^{-1} + \mathbb{K}_2^{-1} + \ldots + \mathbb{K}_n^{-1} \right)^{-1}, \tag{5.17}$$

where $\mathbb{K}_i$, as defined in equation (4.21) in chapter 4, is related to the close valve stiffness of the corresponding F^{2}MC cell. Therefore, $\mathbf{K}_{11}$ equals to the normalized longitudinal stiffness of the string structure when all of the flow port is closed (no fluid flow allowed between cells). The expression of the other elements in the first row or column, $\mathbf{K}_{1j}$, (j = 2…n) can be re-organized as,

$$\mathbf{K}_{1j} = \mathbf{K}_{11}\left(\mathbb{P}_j - \mathbb{P}_{j-1} \right), \quad j = 2 \ldots n \tag{5.18}$$

where $\mathbb{P}_j$, as defined in equation (4.24) in chapter 4, is related to the closed valve pressure rise of the corresponding F^{2}MC cell. Therefore, $\mathbf{K}_{1j}$ represent the pressure difference between adjacent cell #j and cell #j−1, under the condition that all of the flow ports are closed. The physical meaning of the rest of the stiffness matrix $\mathbf{K}_{ij}$ (i, j = 2…n) can be found through the governing equation at the static state ($\mathbf{KX} = \mathbf{F}_e$) and the 2$^{\text{nd}}$ to n^{th} row of the static governing equations can be written explicitly as,

$$\begin{bmatrix} v_2 \\ \vdots \\ v_n \end{bmatrix} = \begin{bmatrix} \mathbf{K}_{22} & \cdots & \mathbf{K}_{2n} \\ \vdots & \ddots & \vdots \\ \mathbf{K}_{n2} & \cdots & \mathbf{K}_{nn} \end{bmatrix}^{-1} \begin{bmatrix} \mathbf{K}_{21} \\ \vdots \\ \mathbf{K}_{n1} \end{bmatrix} x \tag{5.19}$$

Therefore, the rest of the matrix represents the static fluid displacement through each flow port when the structure is subject to a static end displacement. In summary, the system spectral data is closely related to the individual cell stiffness, pressure rise difference between adjacent cells, as well as the static fluid displacement through each flow port. This observation is consistent with the physical meaning of the stiffness matrix of the dual cell string structure as discussed in section 4.2 of previous chapter.

5.2. Synthesis procedure for a prescribed spectral data

The purpose of the synthesis procedure is to find physically feasible F^{2}MC cellular structure designs to reach the prescribed spectral data. A rigorous mathematical definition of the procedure can be described as follows:

The design of the F^{2}MC based multi-cellular structure is defined by a set of cellular performance parameters $\{\Psi\} = \{\alpha_k,\ \beta_k,\ \delta_k\}_{k=1}^{n} \in \Omega$, because the equivalent stiffness matrix **K** is a function of $\{\Psi\}$ as in equation (5.14). Given a set of target poles and zeros $\{\lambda_i^*\}_{i=1}^{n}$ and $\{\mu_j^*\}_{j=1}^{n-1}$ such that $\lambda_i^* < \mu_i^* < \lambda_{i+1}^*,\ i = 1 \cdots n-1$. Find a set $\{\Psi^*\}$ such that

$$\begin{cases} \sigma\left(\mathbf{M}^{-1/2}\mathbf{K}\mathbf{M}^{-1/2}\right)_{\{\Psi^*\}} = \{\lambda_i^*\}_{i=1}^{n} \\ \sigma\left(\bar{\mathbf{M}}^{-1/2}\bar{\mathbf{K}}\bar{\mathbf{M}}^{-1/2}\right)_{\{\Psi^*\}} = \{\mu_j^*\}_{j=1}^{n-1} \end{cases} \tag{5.20}$$

The problem defined in equations (5.20) is a group of constrained nonlinear algebraic equations. There are $2n$-1 equations (n system poles plus n-1 zeros) and $3n$ unknowns in $\{\Psi\}$, so the number of unknowns is always greater than the number of equations, making the problem mathematically under-determinant. As a result, there might be multiple synthesis results for a single target. The nonlinear relations in equations (5.14 and 5.20) and the complex constraint from Ω onto $\{\Psi\}$ make the synthesis problem challenging to solve. In this chapter, we propose adopting inverse eigenvalue problem (IEP) solvers. The IEP concerns the reconstruction of a system stiffness matrix from a set of prescribed spectral data, so instead of searching for $\{\Psi\}$ directly from the target, one can first construct a matrix **K** that can reach the target, then find a set of $\{\Psi\}$ that gives such **K** matrix. In this way, the characteristics of matrix **K** can be exploited to simplify the overall synthesis procedure.

There are different categories of IEP based on the characteristics of the matrix, and each category requires a specific technique to be solved (Joseph 1992, Chu and Golub 2005, and Gladwell 2006). For the F^2MC cellular structure synthesis problem, the **K** matrix is real, symmetric, and more importantly, parametric as in equation (5.14). Deriving an original IEP solver specifically for the type of stiffness matrix in the F^2MC problem is beyond the scope of this thesis research, instead, a hybrid method is proposed to incorporate the well-developed *Jacobi inverse eigenvalue problem* (JIEP) solver and a genetic algorithm with discrete variables. The logic flow of the proposed hybrid synthesis procedure is summarized in figure 5.2. Once the target spectral data (poles and zeros position) are chosen, a generic algorithm with discrete variables are first employed to generate a population of design candidates. Each of the design candidate can achieve poles and zeros close

to the target but not accurately. Then JIEP is applied to update each of these candidate so that the updated design can accurately reach the target. In the final step, these updated design are checked against the physical requirement of Ω, and the physical unfeasible designs are discarded. The following sections of this chapter shall discuss the technical details of this hybrid procedure.

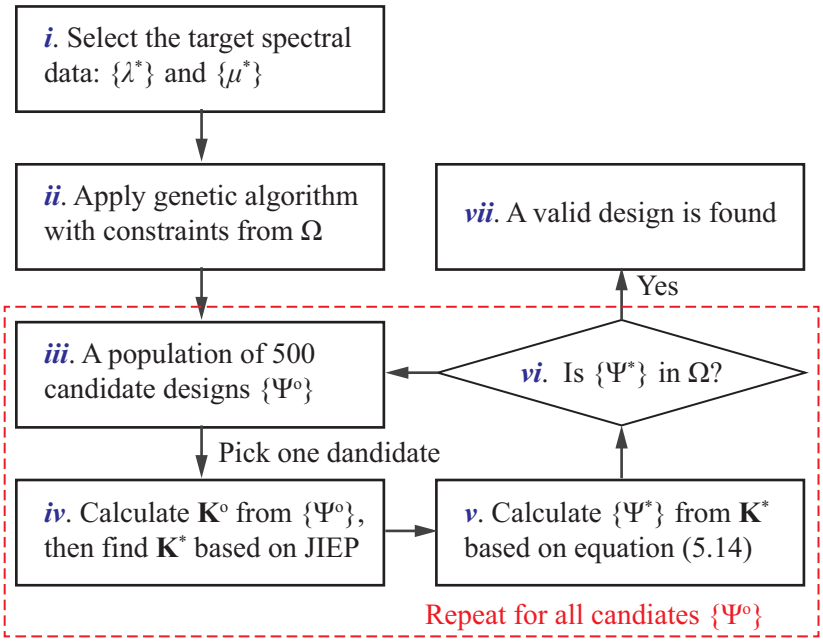

Figure 5.2 Logic flows of the proposed hybrid synthesis procedure. The two major ingredients are genetic algorithm with discrete variables (step *ii*) and a JIEP solver (step *iv*). The detail of step *iv* is in figure 5.4.

5.2.2 Implementing genetic algorithm.

The purpose of implementing genetic algorithm is to generate a population of cellular structure candidate designs, each denoted as $\{\Psi^\circ\}$, so that $\{\Psi^\circ\}$ satisfies the constraints from Ω and gives a spectral data close to the target. Since Ω has a very complicated

geometry, a three dimensional grid is constructed to span the space of Ω as reflected in figure 4.2, in this chapter, the size of the grid is set at 150×50×50, which is denser than the mesh grid in the previous chapter. And the genetic algorithm can be applied based on the discretized performance parameters as follows,

Assume $\left\{\Psi^{\circ}\right\}$ consists of *n* points from the three-dimensional grid in Ω, and denote $\left\{\lambda_i^{\circ}\right\}_{i=1}^{n}$ and $\left\{\mu_j^{\circ}\right\}_{j=1}^{n-1}$ as the poles and zeros based on $\left\{\Psi^{\circ}\right\}$.

Find $\left\{\Psi^{\circ}\right\}$ to minimize the vector norm objective function:

$$S = \left\| \lambda_1^{\circ} - \lambda_1^{*}, ..., \lambda_n^{\circ} - \lambda_n^{*}, \mu_1^{\circ} - \mu_1^{*}, ..., \mu_{n-1}^{\circ} - \mu_{n-1}^{*} \right\|. \tag{5.21}$$

By restricting $\left\{\Psi^{\circ}\right\}$ to the grid, the constraints from Ω are automatically satisfied. Since the under-determined nature of the synthesis problem allows multiple solutions, the genetic algorithm can be repeated from random initial points to generate a population of different candidate designs. Two sample results of $\left\{\Psi^{\circ}\right\}$ are summarized in table 5.1 with their achieved spectral data. The genetic algorithm in this chapter comes from the global optimization toolbox of MATLAB® (version R2011a or above).

5.2.3 Implementing JIEP Solver

The purpose of implementing JIEP solver is to adjust $\left\{\Psi^{\circ}\right\}$ to $\left\{\Psi^{*}\right\}$ so that the target spectral data can be accurately achieved. JIEP solver is originally intended to construct a symmetric, tri-diagonal matrix (Jacobi matrix) from prescribed spectral data. For example, JIEP solver can be used to assign the spring and mass values of an oscillator series in figure 5.3. There are two advantages of adopting the JIEP solvers. The first advantage is that the system intended for JIEP shares some physical similarities with the

F^2MC based structure. The second advantage is that JIEP solver is mathematically well posed: the theories for the existence and uniqueness of solution are well developed, and it can guarantee that the target poles and zeros can be reached simultaneously (Chu and Golub. 2005, and Hald 1976).

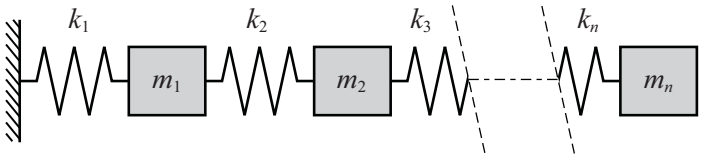

Figure 5.3 Illustration of a mass spring-oscillator series. The JIEP technique can solve the spring mass assignment problem for an oscillator like this for a set of prescribed spectral data, as long as the system stiffness matrix is a symmetric, tri-diagonal matrix (Jacobi matrix).

On the other hand, there are two crucial differences between the oscillator series in figure 5.3 and the F^2MC based cellular structure. The first difference is that the matrix $\mathbf{K}$ of the cellular structure in equation (5.14) is not a Jacobi matrix. The second difference is that the elements in $\mathbf{K}$ must satisfy the restriction from Ω so they cannot take arbitrary values. To address the differences, the JIEP solver is implemented together with House-holder tri-diagonalization. Define $\mathbf{S}^\circ = \mathbf{M}^{-1/2}\mathbf{K}^\circ\mathbf{M}^{-1/2}$, where $\mathbf{K}^\circ$ is based on a structural design candidate $\left\{\Psi^\circ\right\}$ from the genetic algorithm. The Householder transforms $\mathbf{S}^\circ$ into a Jacobi matrix $\mathbf{J}^\circ$ while preserving its spectral data (figure 5.4).

Once the Jacobi matrix $\mathbf{J}^\circ$ is calculated, its elements can be updated with JIEP solver to $\mathbf{J}^*$ so that it gives the exact target poles and zeros. In this paper, the Lanczos Method in Chu and Golub (2005) is adopted as follows. Define $\mathbf{q}_n = \left[c_1,\ c_2,\ \cdots,\ c_n\right]^\top$ such that

$$c_i^2 = \frac{\prod_{k=1}^{n-1}\left(\lambda_i^* - \mu_k^*\right)}{\prod_{\substack{k=1 \\ k\neq i}}^{n}\left(\lambda_i^* - \lambda_k^*\right)}. \tag{5.22}$$

Then one can calculate the first set of elements in $\mathbf{J}^*$ as follows,

$$a_n^* = \mathbf{q}_n^\top \Lambda \mathbf{q}_n,\ b_{n-1}^* = \left\| \Lambda \mathbf{q}_n - a_n^* \mathbf{q}_n \right\|, \text{ and } \mathbf{q}_{n-1} = \left(\Lambda \mathbf{q}_n - a_n^* \mathbf{q}_n \right) \Big/ b_{n-1}^*. \tag{5.23}$$

For $i = 1 \cdots n-2$, one can compute recursively the following elements,

$$\begin{aligned} a_{n-i}^* &= \mathbf{q}_{n-i}^{\mathrm{T}} \Lambda \mathbf{q}_{n-i} \\ b_{n-i-1}^* &= \left\| \Lambda \mathbf{q}_{n-i} - a_{n-i}^* \mathbf{q}_{n-i} - b_{n-i}^* \mathbf{q}_{n-i+1} \right\| \\ \mathbf{q}_{n-i-1} &= \left(\Lambda \mathbf{q}_{n-i} - a_{n-i}^* \mathbf{q}_{n-i} - b_{n-i}^* \mathbf{q}_{n-i+1} \right) \Big/ b_{n-i-1}^* \end{aligned} \tag{5.24}$$

where $\Lambda = \mathrm{diag}\left(\lambda_1^*, \lambda_2^* \ldots \lambda_n^*\right)$, and finally $a_1^* = \mathbf{q}_1^\top \Lambda \mathbf{q}_1$, the final Jacobi matrix $\mathbf{J}^*$ can be written as,

$$\mathbf{J}^* = \begin{bmatrix} a_n^* & b_{n-1}^* & & 0 \\ b_{n-1}^* & \ddots & \ddots & \\ & \ddots & a_2^* & b_1^* \\ 0 & & b_1^* & a_1^* \end{bmatrix}. \tag{5.25}$$

Then an inverse Householder transformation is applied to $\mathbf{J}^*$ to calculate the updated cellular structure equivalent stiffness matrix $\mathbf{K}^*$ (figure 5.4). And finally, the final solution of cellular performance parameters $\left\{\Psi^*\right\}$ can be calculated based on equation (5.14), which can be done by commercial numeric nonlinear algebraic equation solver, such as "`fsolve`" in the MATLAB®. Two synthesis sample results are listed in table 5.1,

and their corresponding physical cellular design parameters are also listed. In these two sample results, even though the genetic algorithm produces results with some error, the JIEP solver manages to correct the candidate designs to reach the target accurately.

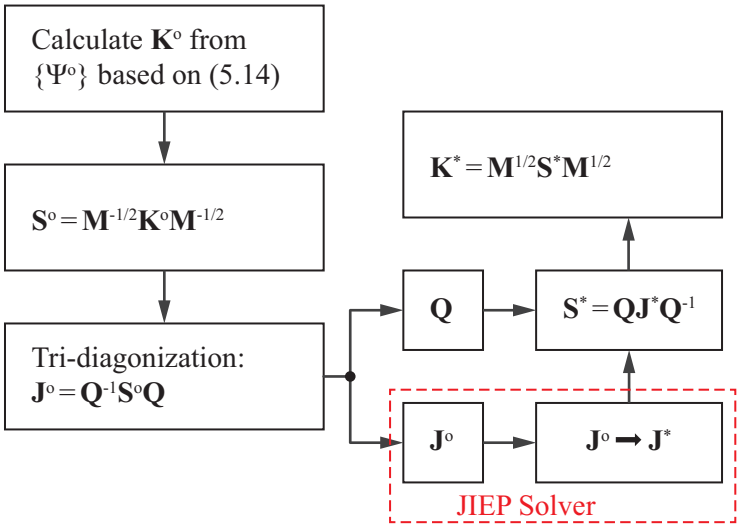

Figure 5.4 JIEP solver integrated with Householder tri-diagonalization. These steps combined represent the step *iv* in figure. 5.2.

Note that, the JIEP solver does not enforce the constraint from Ω, however, if $\{\Psi^\circ\}$ gives a spectral data close to the target, $\{\Psi^*\}$ is not far away from $\{\Psi^\circ\}$, so there is a good chance that $\{\Psi^*\}$ still lies within Ω. Interested readers are encouraged to refer chapter 4 to review how to decide whether $\{\Psi^*\}$ satisfies the constraint from Ω. The intention of the proposed hybrid synthesis procedure is not to mathematically prove the existence of the synthesis solution for a target spectral data, instead, Step *iii*-*vi* in figure 5.2 are repeated for all of the candidate designs from the genetic algorithm, which is computationally inexpensive, and if the JIEP solver could not produce any final valid designs out

of the candidates, the corresponding target spectral data is probably not achievable. The complete MATLAB™ script for the hybrid synthesis procedure is attached in appendix E.

5.2.3 Synthesis results case study

This sub-section will present some synthesis case studies on a F^2MC based triple cellular structure. Figure 5.5 is a pair of "heat map" that demonstrate the results of a numerical survey on the achievable spectral data from the F^2MC based triple cellular structure. In figure 5.5a, the target poles are fixed at 40, 60 and 80Hz and the two zeros can vary between the two adjacent poles. For each set of target zeros (a square "pixel" in the heat map), the genetic algorithm will first generate 500 candidate designs $\{\Psi^{\circ}\}$, then the hybrid JIEP solver will search for valid designs $\{\Psi^{*}\}$ out of this candidate pool. The temperature of the corresponding "pixel" in the heat map represents the number of final designs found. This process is then repeated for every set of target zeros. Since the genetic algorithm starts searching for solution from random initial designs, a "hotter" pixel indicates a wider distribution of feasible cellular designs from the corresponding target. There is also the transparent regions indicating the probably un-achievable set of spectral data. Figure 5.5b is a similar survey results with the target poles fixed at 35, 65, and 95Hz.

The histograms in figure 5.6 demonstrate the distribution of the synthesis results for a single set of achievable spectral data. These results are distributed by the physical design variables. Two sets of structure designs are represented and compared, the first set (solid lines) are synthesis results for target poles at 40, 60, and 80Hz and zeros at 50 and 70Hz, the second set (dashed lines) are for the same target except for the second zero changed to 65Hz. These histograms are based on 300 final valid designs (not candidate

design) for each target, which is sufficiently large because adding more designs will not significantly alter the histogram distribution. Based on these histograms, one can observe some narrow distributions of the final designs, such as fiber angle of cell #1 and cell wall thickness of cell #3, and the small change in target spectral data could bring up some significant changes in some cellular designs as well (such as the wall thickness of cell #2). Among the three major physical design variables, the elastic anisotropy ratio of the cell wall material seems to be the least sensitive to the change of spectra data targets. This is advantageous because in the F^2MC fabrication process (filament winding), elastic anisotropy is the most difficult design variable to tailor.

The case studies highlight the advantages of the proposed synthesis procedure: computationally efficient, accurate, and capable of quickly providing a large number of valid designs for a target spectral data. On the other hand, further case studies revealed that the proposed procedure is no longer accurate for structure with more than three cells, that step *v* in figure 5.4 couldn't produce $\{\Psi^*\}$ that both satisfy the constraint from Ω and reach target accurately. This is probably due to two factors. The first factor is the mathematical complexity of the system stiffness matrix **K** in equation (5.14). As the number of F^2MC cell increases, **K** becomes an extremely complex function of all of the performance parameters. The second factor is the narrow distribution of some final valid designs as mentioned earlier. It is possible that there are more of these kind of narrow distributions in the synthesis problems with more F^2MC cells, so it is more challenging for the synthesis procedure to locate any valid designs. Therefore the synthesis procedure might need to be revised to be more mathematically rigorous. Nonetheless, the general dynamic model and the triple cell synthesis study in this paper are significant advancements that provide us

with valuable tools on designing and investigating the functionalities of the F^2MC based multi-cellular structure.

Table 5.1 Sample synthesis results. Set A has target poles at 40, 60, 80Hz and zeros at 50, 70Hz. Set B has target poles at 35, 65, 95Hz and zeros at 50, 80Hz. The candidate design from GA are restricted to the 150×50×50 grid, here the actual values of α, β, and δ are shown.

		Candidate from GA $\{\Psi^o\}$			Final design from JIEP $\{\Psi^*\}$			Physical cellular designs		
		α	β	δ	α	β	δ	φ (^{o})	a_i/a_o	E_1/E_2
Set A	Cell #1	2.54	1.01	0.48	2.55	0.97	0.36	76.2	0.89	498
	Cell #2	7.91	-14.39	75.17	7.10	-12.02	99.44	14.0	0.67	125
	Cell #3	2.62	0.30	1.05	2.54	0.31	0.98	58.7	0.79	788
	Achieved ω_p, ω_z	ω_p= 41.9, 59.4, 81.0Hz, ω_z=50.2, 67.1Hz			ω_p= 40, 60, 80Hz, ω_z=50, 70Hz					
Set B	Cell #1	2.93	-2.13	2.78	3.00	-2.00	2.66	40.2	0.80	120
	Cell #2	2.70	-2.97	5.08	2.59	-2.88	4.91	37.5	0.80	1073
	Cell #3	2.64	1.01	0.47	2.61	0.99	0.33	77.0	0.89	206
	Achieved ω_p, ω_z	ω_p= 37.5, 66.4, 97.5Hz, ω_z=49.9, 78.9Hz			ω_p= 35, 65, 95Hz, ω_z=50, 80Hz					

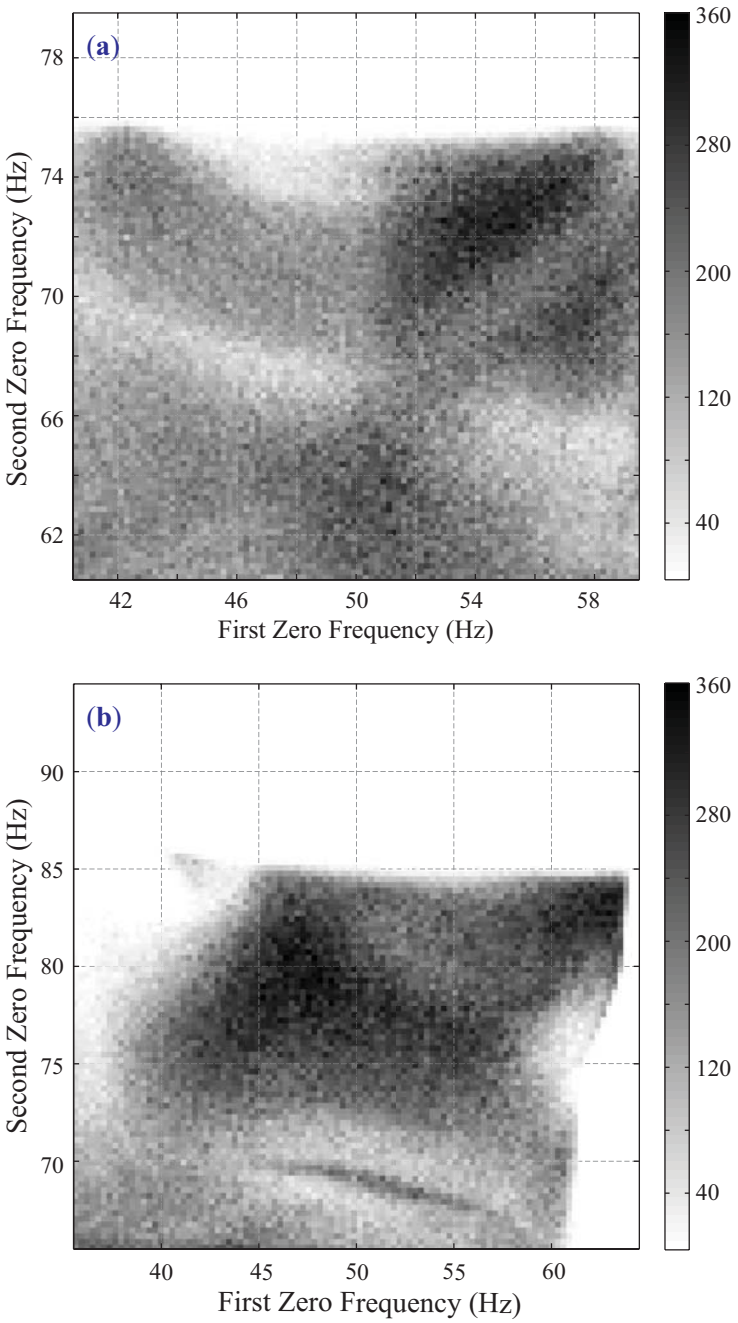

Figure 5.5 Achievable poles and zeros from a triple cell string structure. The heat map represents the number of valid designs found from the 500 candidate designs from the genetic algorithm for each set of target zero. The plot (a) has poles fixed at 40, 60, and 80Hz, plot (b) has poles fixed at 35, 65, and 95Hz.

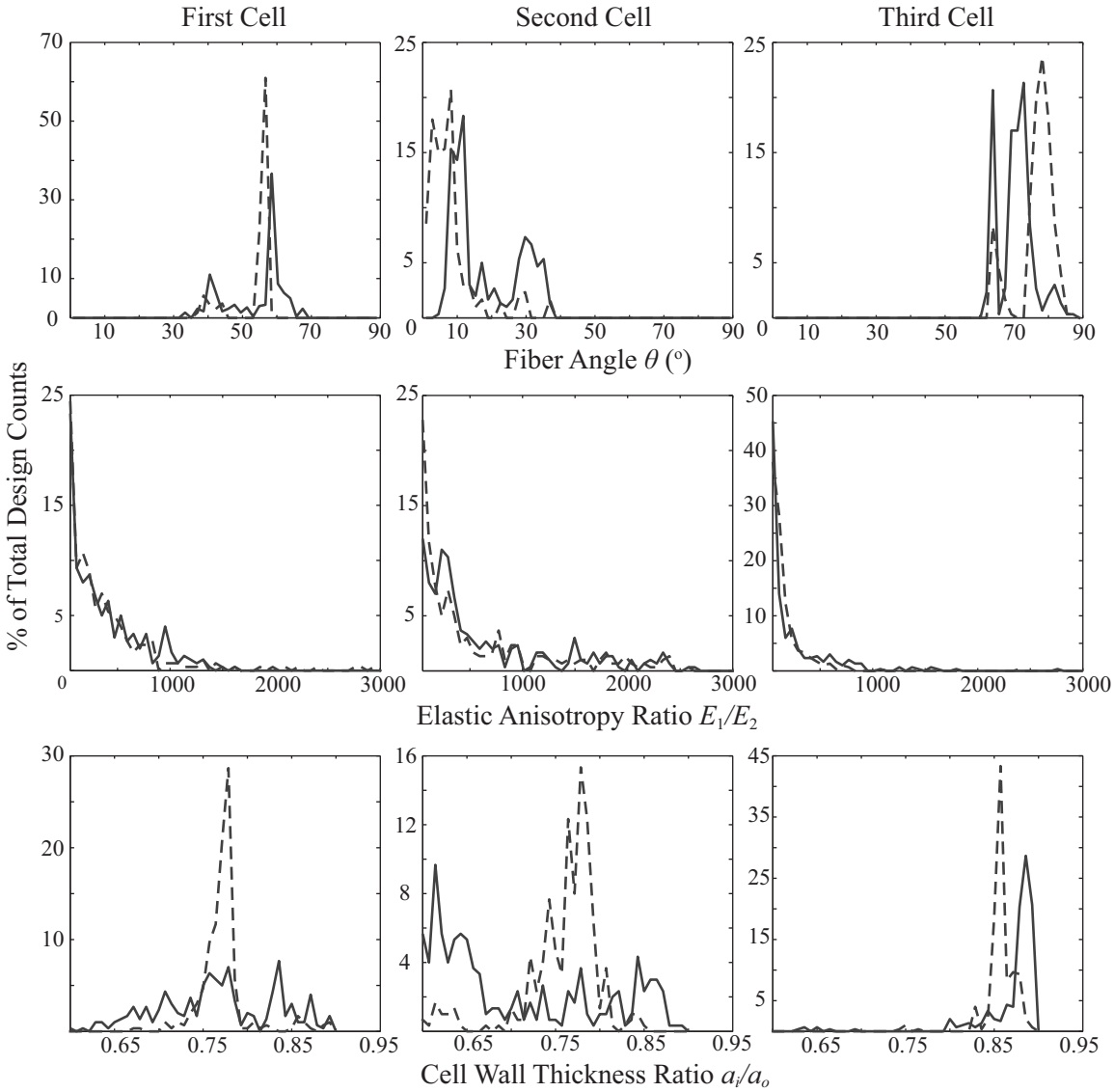

Figure 5.6 The histogram plot of the cellular synthesis results for a specific set of prescribed spectral data. The solid lines represent the target poles at 40, 60 and 80Hz and zeros at 50 and 70 Hz, the dashed lines represent the same target except for the second zero changed to 65Hz.

5.3 Summary

The research presented in this chapter aims at developing systematic synthesis procedure for the F^2MC based multi-cellular structure for a prescribed set of spectral data. This is the first systematic attempt to design a multiple cellular structure where different F^2MC are allowed to be different from each other. As the first step toward this goal, a non-dimensional dynamic model is developed based on the F^2MC performance parameters that are defined in the previous chapter. This model reveals some physical insights that the system spectral data is closely related to three factors: 1) the individual cell stiffness, 2) pressure rise difference between adjacent cells, as well as 3) the static fluid displacement through each flow port. The derivation process of this generalized dynamic model clearly demonstrates the benefits from the abstract performance parameters. Without them, the mathematics derivation will be simply too complicated for engineers to reveal any physical insights.

A synthesis procedure for the F^2MC based multi-cellular structure is then developed. This procedure combines Jacobi inverse eigenvalue problem (JIEP) solver and the genetic algorithm with discrete variables. This hybrid procedure is computationally more efficient compared to brute-force optimization iteration, because it exploit the characteristics of the system equivalent stiffness matrix, and produce multiple designs in one single simulation. For a cellular string structure with three cells, it successfully overcomes the two mathematical challenges in the problem: 1) the complicated nonlinear, under-determined relationship between cellular performance parameters and system spectral data, and 2) the physical constraints on F^2MC cell designs. The synthesis case studies demonstrate that the proposed procedure can effectively select triple F^2MC cellular design parameters

to accurately achieve the target spectral data. And numerical survey illustrates the large range of achievable spectral data targets as well.

On the other hand, further case studies reveal that the proposed procedure is no longer accurate for structure with more than three cells. Although probable causes of this inaccuracy are discussed, connecting more than three cells directly by one internal fluidic circuit seems to make the system too complex to be analyzed and synthesized efficiently based on the knowledge and tools developed in this chapter. Therefore, it is suggested to focus on the design and synthesis of dual or triple cell system as a structural *unit*, and then assemble these units mechanically into a large-scale cellular structure. By this hierarchical approach, the rich list of adaptive functions from F^2MC based system can still be achieved with great versatility, while the complexity in synthesis can be maintained at a manageable level. This approach is advanced in the following chapter, where the architecture design and performance range of a dual cell unit are extensively investigated.

Chapter 6
Architectural Design and Comprehensive Synthesis

This chapter strives to consolidate the lessons and experiences from the last three chapters, and to mature our knowledge base and synthesis methodologies in order to fully address the problem statements as laid out at the beginning of this thesis. The previous analysis and synthesis results have demonstrated two outstanding advantages of the F^2MC based cellular structure. The first advantage is its rich functionality, including actuation with an enhanced authority, vibration isolation, as well as variable stiffness. The second advantage is the versatile design space, especially regarding to the dynamic functions (spectral data). Extensive synthesis case studies revealed that 1) the dual and triple cell string structures can reach a wide range of spectral data, so it can be tailored to satisfy various dynamic application requirements; and 2) for a set of achievable spectral data, multiple cell designs are available, forming a design space, and this gives engineers the freedom to implement other design considerations and optimize the overall structural performance.

On the other hand, there are still two crucial limitations in the previous work that prevent us from fully addressing the thesis problem statements. The first limitation is the simple structural layout: all previous works assume the F^2MC cells connected in a simple series with a closed internal flow circuit, yet there might be other unique configurations to fluidically and kinematically connect them. A comprehensive list of such configuration is

especially important for efficiently distributing and connecting many of F^2MC cells in a large-scale structure. The second limitation is the simple synthesis target: previous synthesis procedures only employ spectral data as the performance target, which is related to the dynamic functions; while other F^2MC functions such as variable stiffness are not yet considered. Incorporating multiple function targets in one integrated synthesis procedure is crucial for our original research vision of achieving multi-functionalities concurrently.

Therefore, the research objective of this chapter is to address the aforementioned two limitations in order to fulfill the potential of the F^2MC based cellular structures. To achieve this objective, this chapter will first survey the unique configurations of fluidically and kinematically connecting F^2MC cells, and these configurations will be named "architectures of the cellular structure", or simply architecture. Following the lessons from the end of last chapter, this chapter will focus on a dual F^2MC system. Dynamic system governing equations will be derived and experimentally tested for these architectures. In the second part of this chapter, the research focus will then turn to developing synthesis procedures with multiple performance targets, where the actuation authority, variable stiffness, and spectral data are considered concurrently. This synthesis procedure will be generic and applicable to the different architectures. Case studies will be presented to compare the performance differences between architectures to offer design insights. The outcome of this chapter will provide a more comprehensive and rigorous knowledge base and design tools to foster the adaptation of F^2MC based cellular structure concept to a wide range of engineering applications, such as soft robotics, morphing structures, and advanced civil infrastructures.

6.1 Architecture of the F^2MC based cellular structural unit

In this chapter, the "architecture" of the cellular structure is defined as the unique configurations by which different F^2MC cells are fluidically and kinematically connected to each other. The F^2MC based dual and triple cell series structures discussed in the previous two chapters belong to a specific architecture example, where 1) all cells are kinematically connected in series so that their internal axial force are equal; and 2) their fluid circuit is closed without external connections; the working fluid can thus only flow between the adjacent cells but not in or out of the system. A complete list of the unique architectures is a crucial knowledge once the number of cells in the structure becomes large, because it provides guidelines for an efficient F^2MC distribution and connection. The research work in this chapter will focus on a dual F^2MC cell system because 1) two are the smallest cell number by which all of the aforementioned structural functions can be achieved; and 2) the mathematical principle that defines the unique architectures of the dual cell system is essentially the same for systems with a larger number of cells, and 3) the synthesis problem for dual cell system is better posted mathematically as compared to system with more cells. Therefore, focusing on the dual cell system will offer us in-depth knowledge on architectural design without unnecessary complexity.

6.1.1 Mathematically defining the architectures

This section will lay down the mathematical framework behind the architectures of a dual cellular structural unit; with a complete list of architectures generated at the end.

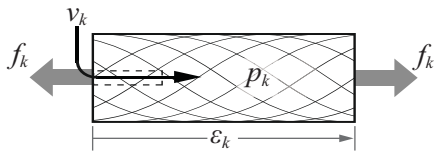

Figure 6.1 Free body diagram of an individual F^{2}MC cell within the structure. There are four types of state variables describing a single cell: the internal fluid pressure (p_k); the fluid flow volume (v_k); the axial force (f_k); and the axial strain (ε_k). k is the id of the F^{2}MC cell, so in the dual cell system it will take the value of either 1 or 2. Positive v_k corresponds to the flow direction as indicated by the arrow, and positive F_k corresponds to a tension force.

Based on the free body diagram of an individual F^{2}MC cell (figure 6.1), there are eight state variables describing the dual cell system: the internal working fluid pressure (p_1, p_2); axial strain (ε_1, ε_2); axial internal force (f_1, f_2); and the net flow volume into the cell (v_1^{net} , v_2^{net}). For simplicity, v_k^{net} will be denoted as v_k in the following derivations. These eight state variables are the eight "unknowns" of the system. Note that all of these variables are in their dimensionless form as defined in chapter 3 and thus their over hats are emitted for simplicity. There are four performance equations (two for each cell) to correlate these state variables defined in equation (5.1-2). There are two more dynamic equations: the flow port equation (5.4) and external inertia dynamics. In the previous work, this eternal inertia is simply an end mass. Therefore, performance relationships and the system dynamics give six equations in total. In order to make the dual cell system mathematically determined, two extra equations (or constraints) are necessary, and it is the selection of these two constraints that defines the unique cellular structure architecture. The constraints are closely related to the eight state variables, because each type of state variables has its own physically admissible constraints as listed below (figure 6.2).

Constraint A on the fluid flow volume (v_k): one can apply $v_1 + v_2 = 0$, meaning that the working fluid is free to flow between the two cells through the flow port, but could not flow in or out of the whole system. This leads to a closed fluidic circuit.

Constraint B on the fluid pressure (p_k): one can apply $p_1 = p_e$ or $p_2 = p_e$, where p_e is the external pressure. This leads to an open fluid circuit where one F^2MC cell can be connected to a pressure supply (pumping).

Constraint C on the axial internal force (f_k): one can apply $f_1 = f_2$, meaning that the two cells are connected in series so that their internal axial force is balanced.

Constraint D on the axial cell wall strain (ε_k): one can apply $\varepsilon_1 = q\varepsilon_2$ where q is a real constant, meaning that the two cells are connected with some kinematic constraints onto their axial deformation. For example, q equals to -1 in figure 6.2d if the two cells have equal length.

Constraint A and B are fluidic, while the constraint C and D are kinematic. One can thus choose two out of the list of four constraints to make the system mathematically determined, so that the number of unknowns (eight state variables) equals to the number of equations. It turns out that each unique combination of two constraints corresponds to a unique architecture of the cellular structural unit as illustrated in figure 6.3, where the simple dual cell series structure studied in the previous chapter belongs to the (AC) type of architectures.

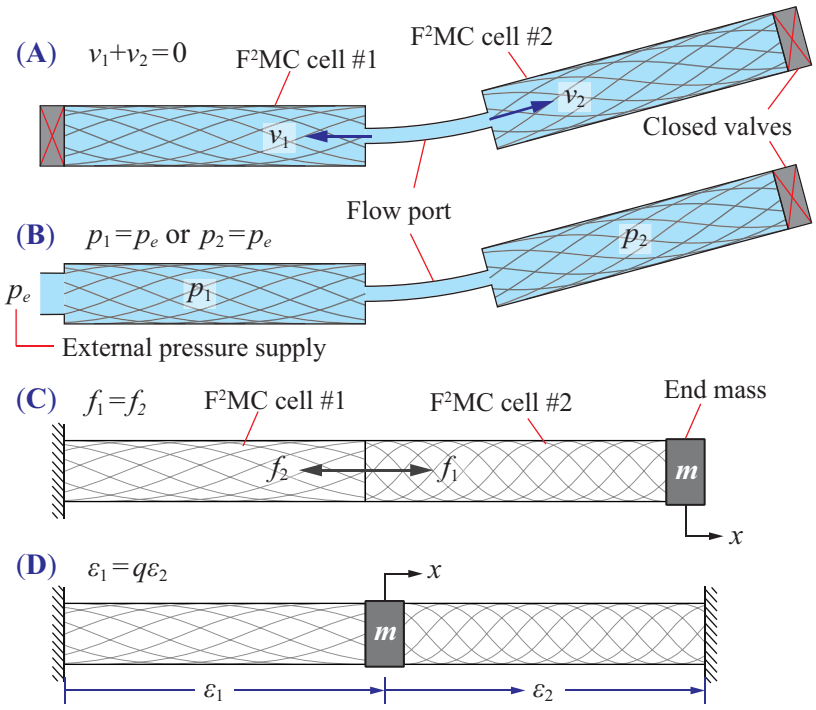

Figure 6.2 Admissible constraints onto each type of state variables. (**A**) Closed fluidic circuit; (**B**) open fluidic circuit connected to external pressure supply; (**C**) F²MC cells connected in series with balanced internal force and (**D**) F²MC cells connected with some kinematic constraint onto its axial deformation.

The schematic diagrams in figure 6.3 are the simplest possible designs to demonstrate these four unique architectures. In practical applications, there can be numerous designs that essentially belong to the same architecture type. For example, three apparently very different dual cellular structure designs are illustrated in figure 6.4. The first design is a simple dual cell string, grounded at both ends, with an external mass attached between the cells. In this set up the F²MC can be used to control the dynamic movement of the mass along their axial direction. The second design is an antagonist pair similar to the human upper limb, where the two cells in parallel are connected to an external rotational inertia to provide some rotating or flapping motion. The third design is a lattice unit, where

the ends of the two cells are connected to the pin joints of a rigid four-bar linkage mechanism, so that the F^{2}MC can actively control the deformation and dynamic characteristics of the lattice structure. This type of lattice design is particularly interesting because it can be easily extended to multiple cellular designs with more sophisticated performance. Yet despite the apparent differences among these three sample designs, they all belong to the (AD) type of architecture, where the kinematic constraint constant q is related to their specific designs. Therefore, any generic synthesis procedure developed for the (AD) type of architectures can be applied to all of these three sample designs with minimal alteration.

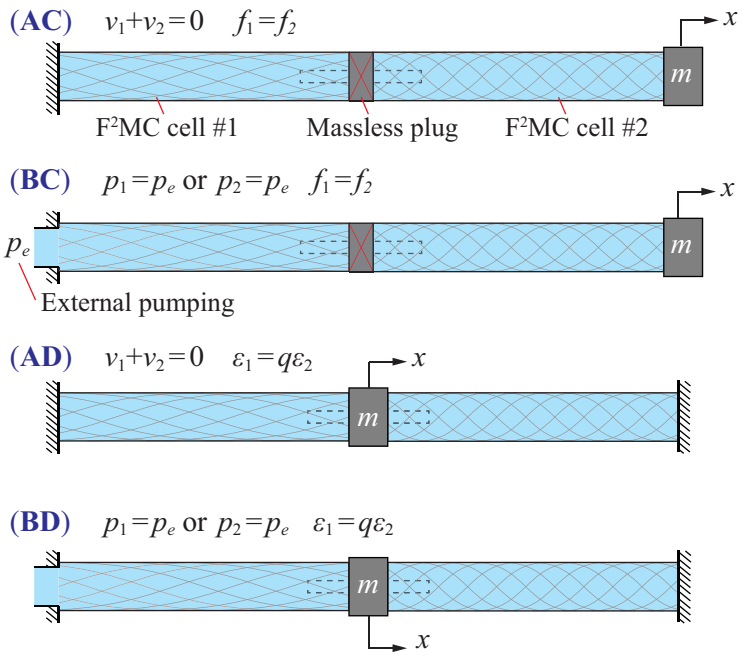

Figure 6.3 Architectures of the cellular structure. Every unique combination of two constraints from figure 6.2 corresponds to a unique architecture of the dual cellular structural unit. (**AC**): two cells connected with a balanced internal force and a closed fluidic circuit. (**BC**): two cells with balanced internal force but with an open circuit. (**AD**): two cells connected with kinematic constraint on their strain and a closed fluidic circuit. (**BD**): two cells with kinematic constraint but an open fluid circuit.

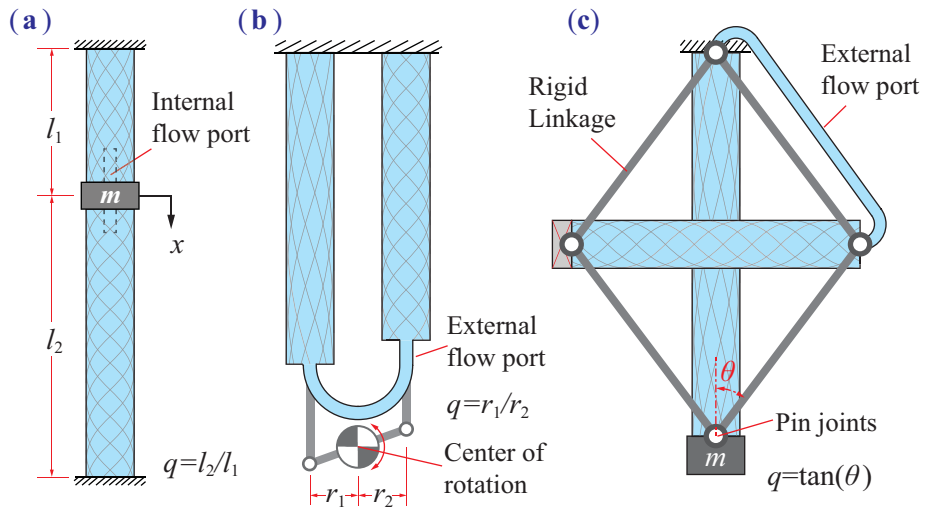

Figure 6.4 Three different designs based on (AD) type of architrave. (**a**) two F^2MC cells connected in a string; (**b**) an antagonist pair connected to an end rotational inertia, and (**c**) a lattice unit.

6.1.2 Governing equations and physical insight

Deriving the governing equations for the four unique architectures as in figure 6.3 is necessary to understand their differences and similarities in dynamic characteristics; it is also necessary for deriving synthesis procedures later in this chapter. Similar to the derivations in the previous chapters, the system governing equations can be obtained by combining the four performance equations, the two dynamic equations, and the two constraints related to the architecture design. The dynamic response of the dual cell system can all be described with an analogy to a two-degrees of freedom mass-spring oscillator:

$$\begin{bmatrix} m & 0 \\ 0 & I \end{bmatrix} \frac{\mathrm{d}^2\mathbf{X}}{\mathrm{d}\tau^2} + \begin{bmatrix} 0 & 0 \\ 0 & R \end{bmatrix} \frac{\mathrm{d}\mathbf{X}}{\mathrm{d}\tau} + \begin{bmatrix} \mathbf{K}_{11} & \mathbf{K}_{12} \\ \mathbf{K}_{12} & \mathbf{K}_{22} \end{bmatrix} \mathbf{X} = \begin{bmatrix} 1 \\ 0 \end{bmatrix} f_e + \begin{bmatrix} \mathbf{G}_1 \\ \mathbf{G}_2 \end{bmatrix} p_e, \quad \mathbf{X} = \begin{bmatrix} x \\ v \end{bmatrix}, \tag{6.1}$$

where x is the normalized external mass displacement, and v is the normalized flow volume though the flow port, R is the flow port resistance, and the derivation of the $\mathbf{K}_{ij}$ term are summarized in table 6.1. The terms related to external pressure supply (p_e) are only applicable to (BC) and (BD) architecture; and the kinematic constraint constant q ($= \varepsilon_1 / \varepsilon_2$) in (AD) and (BD) takes the value of -1. Since there are two external loads (f_e and p_e), the system response can be characterized by two transfer functions: x / f_e and x / p_e. The poles for both transfer functions are the same:

$$\left[\omega_{p_1}, \omega_{p_2}\right] = \sigma\left(\begin{bmatrix} m & 0 \\ 0 & I \end{bmatrix}^{-1/2} \begin{bmatrix} \mathbf{K}_{11} & \mathbf{K}_{12} \\ \mathbf{K}_{12} & \mathbf{K}_{22} \end{bmatrix} \begin{bmatrix} m & 0 \\ 0 & I \end{bmatrix}^{-1/2}\right), \tag{6.2}$$

where $\sigma(\cdot)$ is the operator of calculating eigenvalues, and the zero of the two transfer functions (x / f_e and x / p_e) can be calculated respectively as follows:

$$\begin{cases} \omega_{z_f}^2 = \dfrac{\mathbf{K}_{22}}{I} \\ \omega_{z_p}^2 = \dfrac{\mathbf{K}_{22}\mathbf{G}_1 - \mathbf{K}_{12}\mathbf{G}_2}{\mathbf{K}_{11} I} \end{cases}, \tag{6.3}$$

where the $\mathbf{G}_1$, $\mathbf{G}_2$ term for (BC) type of architecture can be calculate as

$$\begin{bmatrix} \mathbf{G}_1 \\ \mathbf{G}_2 \end{bmatrix} = \begin{bmatrix} 1 - \dfrac{g_1\beta_1\beta_2}{g_2\alpha_2\delta_1 + g_1\left(\beta_2^2 + \alpha_2\delta_2\right)} \\ \dfrac{g_1\beta_1\left(\beta_2^2 + \alpha_2\delta_2\right)}{g_2\alpha_2\delta_1 + g_1\left(\beta_2^2 + \alpha_2\delta_2\right)} \end{bmatrix}, \tag{6.4}$$

and the two terms for (BD) type of architecture are:

$$\begin{bmatrix} \mathbf{G}_1 \\ \mathbf{G}_2 \end{bmatrix} = \begin{bmatrix} 1 \\ \beta_1 \end{bmatrix}, \tag{6.5}$$

where α_k, β_k, and δ_k ($k = 1, 2$) are the performance parameters of the F^{2}MC cell, and $g_k = l_k / a_i$ are the geometric aspect ratio. In equations (6.4-5), the F^{2}MC cell #1 is assumed to be open and connected to external environment, if the cell #2 is open instead, the number 1 and 2 in the variable sub-index needs to swap. The same rule also applies to the list of $\mathbf{K}_{ij}$ terms in table 6.1.

Table 6.1 Derivation of $\mathbf{K}_{ij}$ in the system governing equations.

Architecture	$\mathbf{K}_{11}$ =	$\mathbf{K}_{12}$ =	$\mathbf{K}_{22}$ =
(AC)	$\left(\mathbb{K}_{C_1}^{-1} + \mathbb{K}_{C_2}^{-1}\right)^{-1}$	$\mathbb{P}_{S_2} - \mathbb{P}_{S_1}$	$\mathbf{K}_{21}\mathbb{Q}_{AC}$
(AD)	$\mathbb{K}_{C_1} + \mathbb{K}_{C_2}$	$\mathbb{P}_{P_2} - \mathbb{P}_{P_1}$	$\mathbf{K}_{21}\mathbb{Q}_{AD}$
(BC)	$\left(\mathbb{K}_{O_1}^{-1} + \mathbb{K}_{C_2}^{-1}\right)^{-1}$	$\mathbb{P}_{S_2}$	$\mathbf{K}_{21}\mathbb{Q}_{BC}$
(BD)	$\mathbb{K}_{O_1} + \mathbb{K}_{C_2}$	$\mathbb{P}_{P_2}$	$\mathbf{K}_{21}\mathbb{Q}_{BD}$

In table 6.1, $\mathbb{K}_{C_k}$ ($k = 1, 2$) is the normalized longitudinal stiffness of the F^{2}MC cell #k in the closed valve state, which can be calculated by setting v_k to zero in the performance equations (5.1,2):

$$\mathbb{K}_{C_k} = \frac{f_k}{\varepsilon_k} = \frac{\alpha_k \delta_k + \beta_k^2}{g_k \alpha_k} \tag{6.6}$$

while $\mathbb{K}_{O_k}$ is the open valve stiffness, which can be calculated by setting p_k to zero as,

$$\mathbb{K}_{O_k} = \frac{\delta_k}{g_k} \tag{6.7}$$

Therefore, $\mathbf{K}_{11}$ in the system governing equation is the equivalent stiffness of the two cells connected either "in series" as by constraint C or "in parallel" as by constraint D. The $\mathbb{P}_{S_k}$ ($k = 1, 2$) is the internal rise of pressure in F^{2}MC cell #k against external mass displacement under constraint C; while $\mathbb{P}_{P_k}$ is the pressure rise under constraint D.

$$\mathbb{P}_{S_k} = \frac{p_k}{x} = \mathbf{K}_{11} \frac{-\beta_k}{\alpha_k \delta_k + \beta_k^2} \tag{6.8}$$

$$\mathbb{P}_{P_k} = \zeta \frac{\beta_k}{g_k \alpha_k} \tag{6.9}$$

where $\zeta = -1$ for $k = 1$ and $\zeta = 1$ for $k = 2$ (figure 6.3). Therefore, the $\mathbf{K}_{12}$ terms in the governing equation relate to the pressure difference between the two F^{2}MC cells. In the open fluidic circuit architectures (BC and BD), it is assumed that cell #1 is open to external environment so that their internal pressure rise is zero.

Finally, $\mathbf{K}_{22}$ in the governing equation relates to the static fluid volume displacement through the flow port when the external mass is subject to static displacement:

$$\mathbb{Q}_{AC} = \frac{g_1 g_2 (\beta_1 - \beta_2)^2 + (g_1 \alpha_1 + g_2 \alpha_2)(g_2 \delta_1 + g_1 \delta_2)}{g_1 g_2 \left[\beta_1 \left(\alpha_2 \delta_2 + \beta_2^2 \right) - \beta_2 \left(\alpha_1 \delta_1 + \beta_1^2 \right) \right]} \tag{6.10}$$

$$\mathbb{Q}_{AD} = \frac{g_1 \alpha_1 + g_2 \alpha_2}{g_2 \alpha_2 \beta_1 + g_1 \alpha_1 \beta_2} \tag{6.11}$$

$$\mathbb{Q}_{BC} = -\frac{g_2 \delta_1 + g_1 \delta_2}{g_2 \beta_2 \delta_1} \tag{6.12}$$

$$\mathbb{Q}_{\mathrm{BD}} = \frac{1}{\beta_2} \tag{6.13}$$

6.1.3 Experiment test

The purpose of this experiment is to test the governing equation of motions as derived in the previous section. Since the (AC) type of architecture has been extensively tested in the previous chapters, the experiment efforts in this chapter will focus on the other three types of architectures as listed in figure 6.3. To fulfill the experiment purpose, three new F^{2}MC cell samples are fabricated using the filament-winding process: two cells have ±70° fiber orientation, while the third cell has ±42° orientation. The carbon fiber strips are AS4D-GP 12K manufactured by HEXCEL™; the soft resin is shore hardness 10A polyurethane from the Industrial Polymers; and the fiber volume ratio is about 50%. To test the (AD) and (BD) architectures, the two F^{2}MC cells with ±70° fiber orientation are integrated into the lattice four-bar linkage mechanisms as illustrated in Fig. 6.4(*iii*). This linkage mechanism has one degree of freedom, and applies a kinematic constraint onto the axial deflection of the two F^{2}MC cells so that $\varepsilon_1 = -\varepsilon_2$ ($\theta = 45°$). The two F^{2}MC cells are fluidically connected through an external flow port, which is essentially a long plastic tube with a uniform circular cross-section. Several end mass plates are attached to the end of the linkage mechanism, with a shaker (LDS V400 series) attached to it to provide frequency sweeping external force (figure 6.5). The dynamic system responses transfer equation (x / f_e) are measured by the ratio of the end mass acceleration over the input shaker force. To test the (BC) architecture, two F^{2}MC cells with ±70° and ±42° fiber orientations are simply connected in series according to figure 6.4. Frequency-sweeping shaker force is also applied to the end mass to obtain the system frequency response. The test setup for

(BC) architecture is very similar to the (AC) test setup from the previous chapters; therefore, interested reader can refer the previous works for technical details.

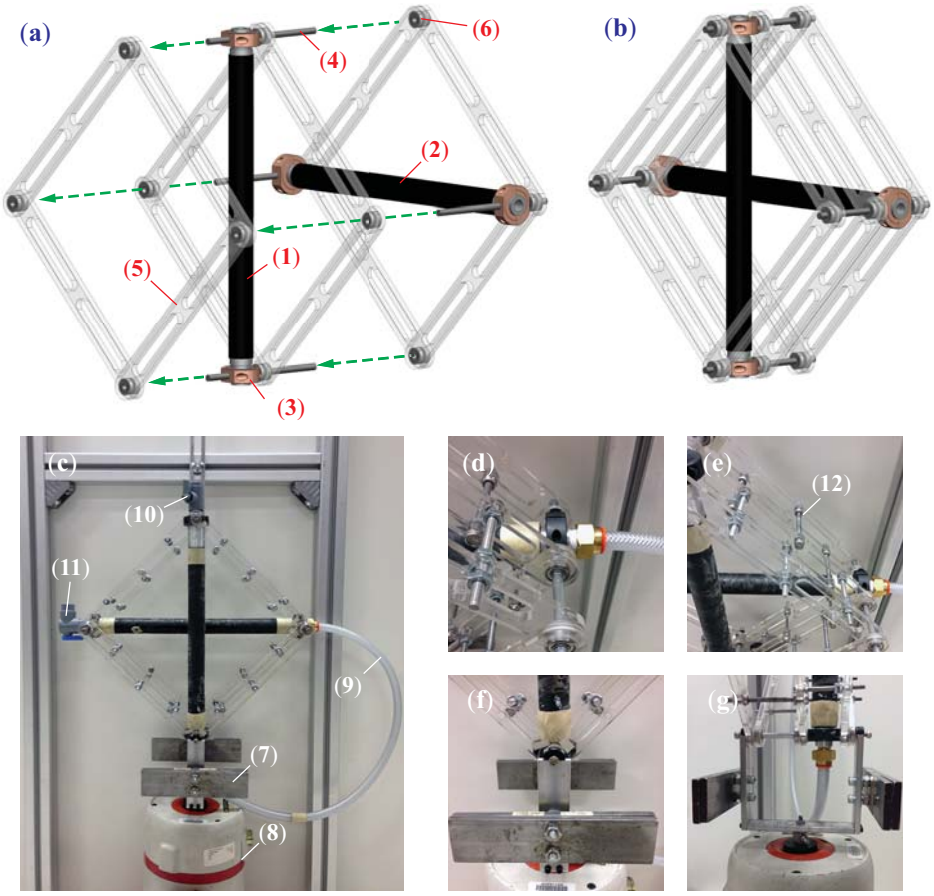

Figure 6.5 (AD) and (BD) linkage mechanism set up. (**a**) The CAD model of the linkage design, and (**b**) fully assembled linkages. The two F^{2}MC tubes are sandwiched between three sets of identical four-bar linkages to guarantee a centered axial loading onto the tubes. The physical prototype is shown in (**c**), where the detailed blown up views are shown in (**d**-**g**). When the end valve (10) is closed, the system is of (AD) architecture with a closed fluidic circuit, when the valve is open, the system becomes (BD) architecture ($p_e = 0$).

Legend: (1) F^{2}MC tube #1; (2) F^{2}MC tube #2; (3) mount collar; (4) shafts; (5) acrylic linkage; (6) ball bearing; (7) end mass plates; (8) shaker; (9) external flow port (10-11) end valves (12) screw rods for extra rigidity.

The α, β, and δ values of the F^{2}MC samples are estimated based on both experiment testing and analytical calculation. For example, to estimate the δ value, which is essentially the normalized stiffness of the empty cell in its axial direction, each individual F^{2}MC sample is connected to the end mass plates to form a spring-mass oscillator. Frequency-sweeping external force is applied to the end mass so that the δ value can be estimated based on the measured natural frequency. Interested reader can refer to appendix D for details. Once the δ value is estimated, the fiber ply transverse elastic modulus (E_2) can be back-calculated based on Lekhniski's solution, so that this E_2 value can be used to calculate α and β values (interested reader can refer to chapter 3 and 4 for details of the Lekhniski's solution). The properties of the three F^{2}MC cell samples are summarized in table 6.2. The test results for (AD), (BD), and (BC) types of architecture agree well to the theoretical prediction in terms pole and zero position, with error of no more than 5Hz (figures. 6.6-6.8).

The working fluid apparent bulk modulus is estimated by fitting the dual cell system frequency response (see the discussion in Chapter 3); it is lower than the ideal 2 GPa value, probably due to the entrapped air bubbles at the low-pressure operation condition as well as other source of unconsidered compliance such as the external flow port wall elasticity. The estimated apparent bulk modulus values varies between different architectures as well, and this is probably related to the different levels of internal pressure rises between different architecture. There are some discrepancies in terms of pole and zero frequency response magnitude as well, especially for the tests with external fluidic port, indicating that the analytical prediction underestimates the flow port resistance. The extra fluid damping is probably from the turbulent nature of the pulsate fluid flow, as well as the transferring

of fluid kinematic energy into the vibration of external flow port near the zero frequency. If the F^{2}MC based cellular structure is to be implemented in practical engineering applications, more careful fluid circuit design is necessary to stabilize and monitor the effective working fluid bulk modulus, as well as to reduce the extra fluid damping. Nonetheless, the reported experiment results agree with the governing equations of motion in terms of poles and zero position, so that they can be utilized in the following synthesis procedures.

Table 6.2 The properties of the F^{2}MC cell samples. The E_2 values are back calculated from the frequency sweeping tests on each individual cell sample. And then this value is used to calculate α and β. The δ values are complex to characterize the structural damping from the composite cell wall. C_f is the normalized apprent fluid compliance ($C_f = E_2/B_k$, where E_2 is the value of cell #2)

	F^{2}MC cell #1	F^{2}MC cell #2	F^{2}MC cell #2
Fiber orientation (φ)	±70°	±70°	±42°
Inner radius (a_i)	11 mm	11 mm	11 mm
Wall thickness (h)	1.6 mm	1.6 mm	0.7 mm
Length (l)	0.23 m	0.26 m	0.22 m
Filament modulus (E_2)	8 MPa	13.5 MPa[2]	23 MPa
α	0.009+C_f	0.012+C_f	0.022+C_f
β	0.77	0.78	-1.55
δ	0.61+0.19i	0.93+0.29i	1.04+0.36i

[2] E_2 value is also a characteristic unit to normalize the system variables, and the value for cell #2 is selected for such purpose.

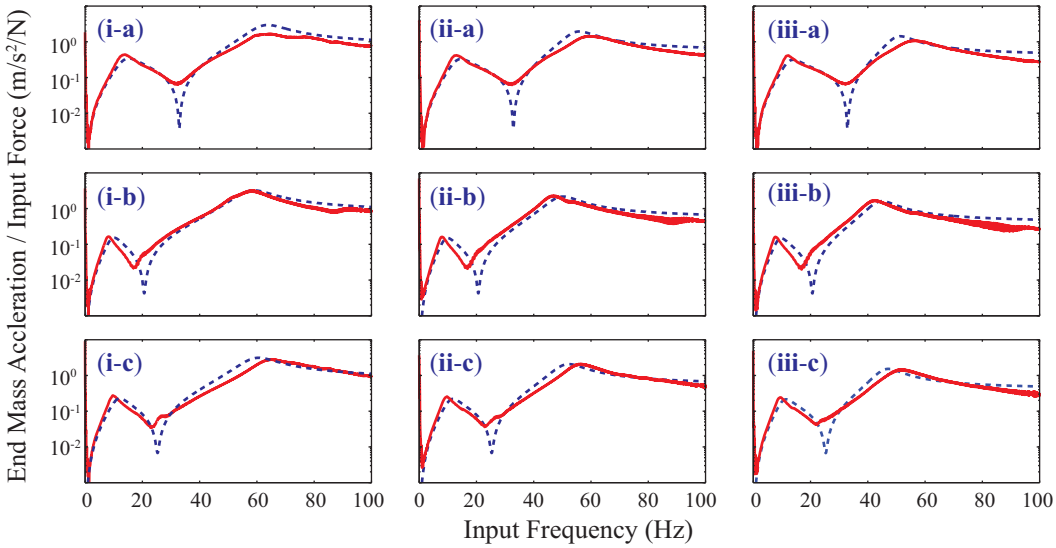

Figure 6.6 Test results for (AD) architecture. The test results are the solid line and analytical predictions are the dashed line. Each plot is the result from a different end mass and flow port combination. The normalized values of the end mass are **i)** 0.97×10^3, **ii)** 1.40×10^3, and **iii)** 1.83×10^3. The normalized port inertance values are **a)** 3.46×10^3, **b)** 8.79×10^3, and **c)** 5.85×10^3. The bulk modulus is estimated to be 65 MPa ($C_f = 0.21$).

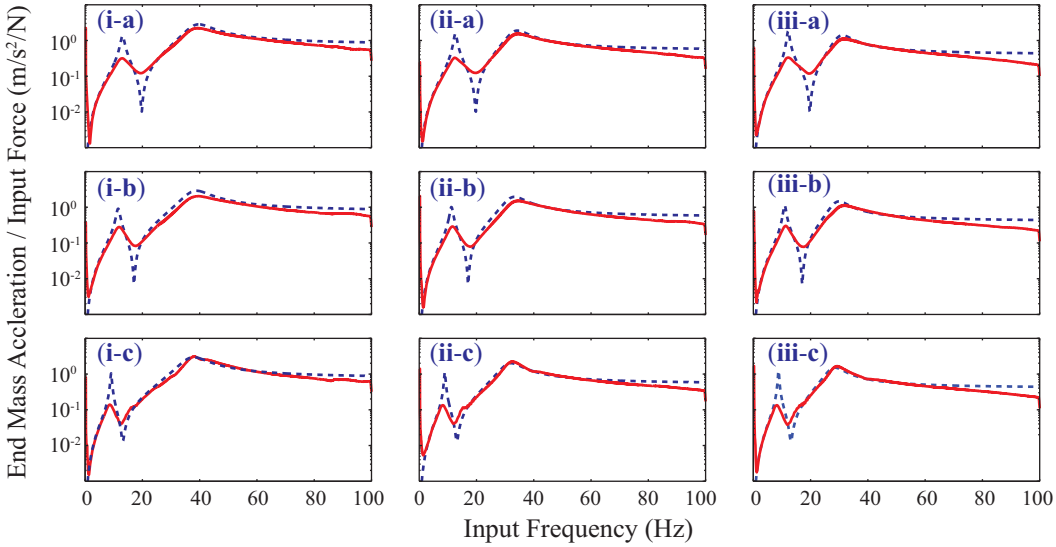

Figure 6.7 Test results for (BD) architecture. The normalized values of the end mass are **i)** 0.97×10^3, **ii)** 1.40×10^3, and **iii)** 1.83×10^3. The normalized values of the port inertance are **a)** 2.59×10^3, **b)** 3.46×10^3, and **c)** 5.85×10^3. The bulk modulus is estimates to be 32 MPa ($C_f = 0.42$).

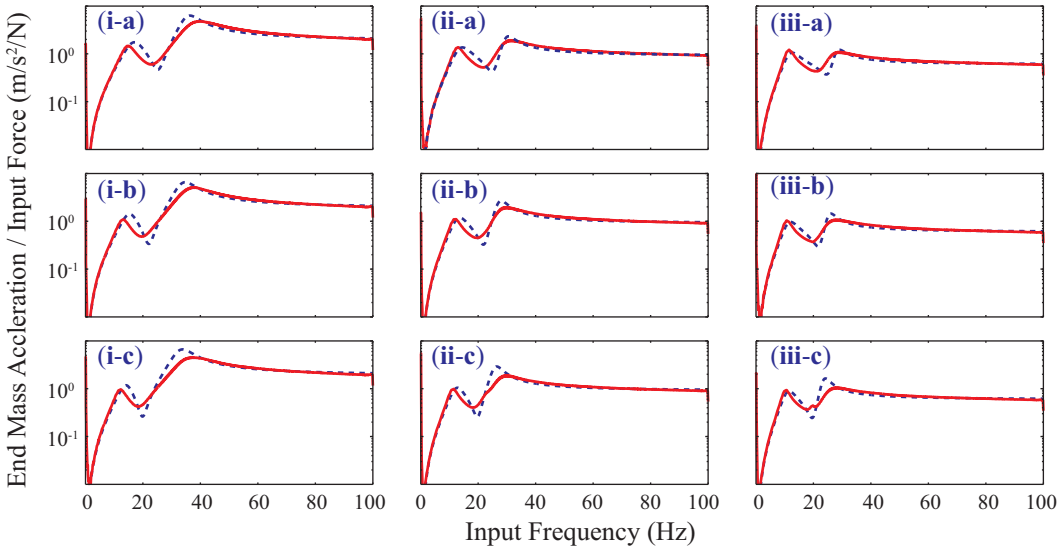

Figure 6.8 Test results for (BC) architecture. The normalized values of the end mass are **i**) 390, **ii**) 820, and **iii**) 1250. The normalized values of the port inertance are **a**) 1.08×10^3, **b**) 1.41×10^3, and **c**) 1.74×10^3. The bulk modulus is estimates to be 50 MPa ($C_f = 0.27$).

6.2 Structure synthesis with multiple target functions

The following section shall address the second part of the problem statement: a synthesis procedure considering multiple performance targets. More specifically, this procedure should be able to select appropriate F^{2}MC designs so that the dual cellular structure can satisfy the requirements from the prescribed spectral data, and then calculate the achievable performance range of other type of structural functions. It should also be applicable to all four unique architectures. This comprehensive and generic synthesis procedure would directly help the engineers fulfill the mission of making F^{2}MC based cellular structure concurrently multi-functional.

6.2.1 Derivation of the synthesis procedure

In chapter 4, a synthesis procedure was successfully derived for a single set of performance target based on a single type of architecture: that is, synthesis for a set of desired ω_{p_1}, ω_{p_2}, and ω_{z_f} ($\omega_{p_1} < \omega_{z_f} < \omega_{p_2}$) on the (AC) type of architecture. Synthesis case studies based on this procedure revealed that for a set of achievable spectral data, the corresponding F^{2}MC pair designs are not unique. It is this non-uniqueness that gives us the freedom to further incorporate more performance targets, because different F^{2}MC pair designs could exhibit different structural performance even if they achieve the same poles and zero. Therefore, the proposed synthesis procedure in this chapter would be a direct extension of chapter 4. To demonstrate the derivation without unnecessary complexity, the flow port resistance (*R* in equation 6.1) and the cell wall structural damping (complex part of δ_k) are neglected, since they have a relatively small effect on spectral data compared to the other design parameters.

There are six independent unknowns to be determined in the synthesis problem, which are the performance parameters (α_k, β_k, and δ_k) for each F^{2}MC cell. To avoid mathematically over-determining the problem, the number of performance targets or constraints should not exceed six. Since the previous synthesis procedure in chapter 4 incorporates three targets already (ω_{p_1}, ω_{p_2}, and ω_{z_f}), up to three additional targets can be incorporated. In this chapter, the performance targets cover both of the static and dynamic functionalities of the F^{2}MC based cellular structure, and they can be categorized in the following four groups.

Target group (I): *Spectral data* ω_{p_1},, ω_{p_2},, *and* ω_{z_f} : which describes the dynamic characteristics of the structure in response to the external load on the end mass. This target

is related to functions such as vibration isolation. Once the positions of these poles and zeros are chosen, the equivalent stiffness matrix in equation (6.1) can be uniquely determined:

$$\mathbf{K}_{11} = m\left(\omega_{p_1}^2 + \omega_{p_2}^2 - \omega_{z_f}^2\right) \tag{6.14}$$

$$\mathbf{K}_{12} = \left[mI\left(\omega_{p_2}^2 - \omega_{z_f}^2\right)\left(\omega_{z_f}^2 - \omega_{p_1}^2\right)\right]^{1/2} \tag{6.15}$$

$$\mathbf{K}_{22} = I\omega_{z_f}^2 \tag{6.16}$$

Based on the equivalent stiffness matrix, a closed form correlation between the performance parameters of the two F^{2}MC cells can be specified for all four types of architectures (the completed derivations of these correlation are listed in appendix F). Therefore, for a given F^{2}MC cell #1 design, there only exist one unique corresponding cell #2 design to reach this group of target spectral data.

Target (II): *System zero* ω_{z_p} which corresponds to the external dynamic pressure supply, shall neither exist nor positions between the two system poles (to be specific, $\omega_{z_p}^2 < 0$ or $\omega_{z_p} > \omega_{p_2} + 5\text{Hz}$ in equation (6.3). Satisfying this target could lead to a high authority resonance actuation with a designated frequency band (interested readers can refer to chapter 3 for related work). However, this requirement on ω_{z_p} is not a rigorous and sufficient condition for the existence of the high authority frequency band, but rather it serves as an intuitive demonstration on how extra requirement can be imposed on the synthesis procedure. This target is only applicable to (BC) and (BD) architecture because the external dynamic pressure supply requires an open fluidic circuit; therefore, in (AC) and (AD) synthesis, this target is not applied.

Target (III): *Static variable stiffness ratio* which characterize the increase of equivalent structural stiffness when both cells changes from open valve state to closed valve state. The ratio of these two stiffness values (R_{K}), is used as the performance index:

$$R_{\mathrm{K}} = \frac{K_{\mathrm{C}}}{K_{\mathrm{O}}} = \frac{\mathbf{K}_{11}}{K_{\mathrm{O}}}, \text{ where } K_{\mathrm{O}} = \begin{cases} \dfrac{\delta_1 \delta_2}{g\left(\delta_1 + \delta_2\right)} & \text{for (AC) (BC)} \\ \dfrac{\delta_1 + \delta_2}{g} & \text{for (AD) (BD)} \end{cases} \tag{6.17}$$

Target (IV): *Static actuation authority*, which characterize the performance of the actuation related applications, can be defined as the ratio of structural deformation (free stroke) over static internal pressure increases as follows,

$$R_{\mathrm{A}} = \left.\frac{x}{p_e}\right|_{f=0\mathrm{Hz}} = \begin{cases} g\left(\dfrac{\beta_1}{\delta_1} + \dfrac{\beta_2}{\delta_2}\right) & \text{for (AC) (BC)} \\ g\dfrac{\beta_1 - \beta_2}{\delta_1 + \delta_2} & \text{for (AD) (BD)} \end{cases} \tag{6.18}$$

Different functionalities can be achieved by integrating the cellular structure with some compact devices that can provide both valve control and pressure supply. Interested readers can refer Kim et al. (2010) for an example, where a piezoelectric-hydraulic pump was connected to an F^2MC based sandwich structure. The variable stiffness ratio and static actuation authority shall be calculated for all of the F^2MC pair designs that satisfies the targets (I) and (II). This set up can offer more valuable information because the range of performance from different type of architectures can be directly compared for better design

insights. It is also worth noting that the purpose of this work is to demonstrate the derivation process of the multi-target synthesis procedure and illustrate the design versatility of the F^{2}MC based cellular structure. Therefore, the aforementioned four targets are by no means comprehensive, because practical applications may require a more sophisticated target definition. However, the proposed synthesis procedure could be easily adapted for other targets as long as they are defined based on the performance parameters of the F^{2}MC cells.

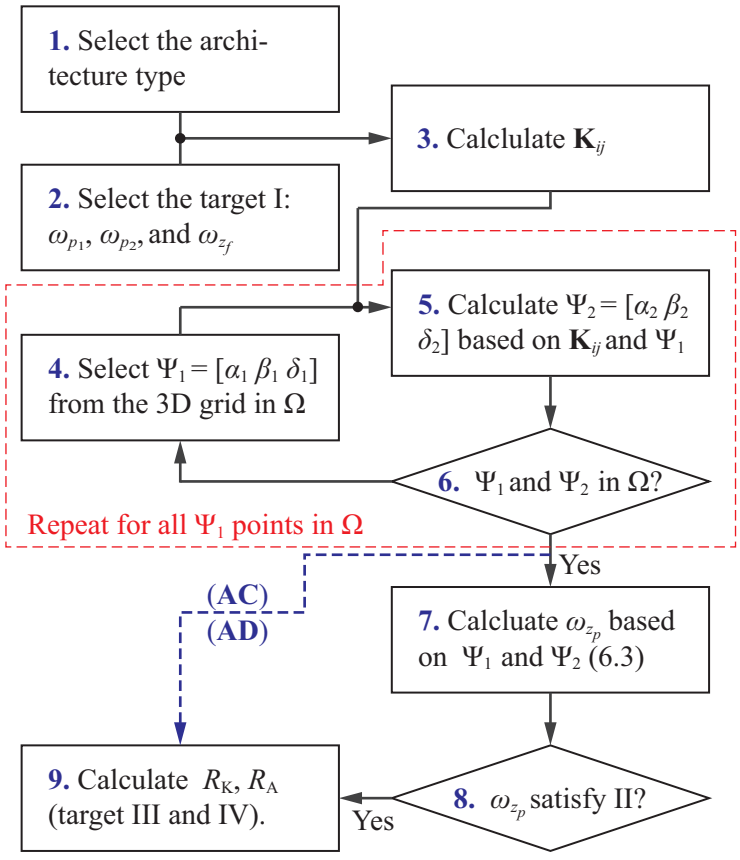

Figure 6.9 The logic flow of the comprehensive synthesis procedure. It can be described as a numerical survey because each grid point in Ω. Note that step 7 and 8 is skipped if the architecture is of (AC) or (AD) type.

The logic flow of the synthesis can be summarized in figure 6.9; it can be best described as a numerical survey. First of all, a three dimensional grid is constructed to span the parametric space Ω; in this particular work, the gird size is set at 50×50×50, and each point in this grid is denoted as Ψ_1 ($=[\alpha_1\ \beta_1\ \delta_1]$). Then an iteration loop (step 4-5-6) is executed on every Ψ_1 point in this mesh, so that for each cell #1 design, the corresponding cell #2 design $\Psi_2=[\alpha_2\ \beta_2\ \delta_2]$ is calculated based on target (I) and the architecture type. Then this cell #2 design candidate is checked for physical feasibility (step 6). To determine whether $\Psi_2 \in \Omega$ is not trivial; and interested readers can refer to chapter 4 for a detailed discussion. If the cell #2 design is physical feasible (that is, $\Psi_2 \in \Omega$), and the architecture is of (BC) or (BD) type, ω_{z_p} is calculated to check whether the Ψ_1, Ψ_2 pair satisfies the requirement from target (II) (step 7-8). If target (II) are satisfied, the variable stiffness ratio (target III), and static actuation authority (target IV) corresponding to the Ψ_1, Ψ_2 pair are calculated and stored. Based on the derivation of the performance parameters (chapter 4), Ψ_1 and Ψ_2 can be translated into physical design variables, which are fiber orientation, cell wall thickness, and cell wall anisotropic elasticity. The complete MATLAB™ script of this multi-target synthesis procedure is attached in appendix G.

6.2.2 Synthesis case studies

This section shall present several synthesis case studies on the F^2MC based dual cellular structural unit. Especially, it will compare the synthesis results from different architectures based on the same targets set. Such comparison can offer design insights for a variety of practical engineering applications. Some required parameters for synthesis is listed in table 6.3.

Table 6.3 Parameters for the synthesis case study. If the values have no unit, they are in the normalized form (refer Chapter 4 for details).

End mass (M)	1500	F^{2}MC inner radius (a_i)	0.01 m
Flow port inertia (I)	1000	Aspect ratio (g_1,g_2)	20
Ply modulus (E_2)	15 MPa	Time unit (τ)	4.61×10^{-5} sec
Effective fluid modulus (B_f)	40 MPa		

Figure 6.10 presents a sample synthesis result. Among the four sub-plots in this figure, two are synthesis results of (BC) type of architecture and two are of (BD) type. Each point in these plots represent a feasible physical design for cell #1 that satisfy the spectral data requirements from target group (I) and (II). In this particular case, ω_{p_1} is set at 25 Hz, ω_{p_2} = 50 Hz, ω_{z_f} =35 Hz, and ω_{z_p} is higher than 55 Hz or non-exist. The color of on each point represents the variable stiffness ratio or static actuation authority corresponding to this particular design. Due to the nature of the numerical simulation, these feasible designs appear to be groups of discrete points; however, they span the domain of a continuous design subspace in Ω, since the closed form correlation between the performance parameters and the spectral data targets are continuous and invertible. The synthesis results in figure 6.10 clearly demonstrate the wide physical design space of the F^{2}MC based cellular structure for a given set of target spectral data. And each design gives a unique combination of variable stiffness and static actuation authority even though they achieve the same spectral data. Such versatility can be a great advantage from a system designer point of view.

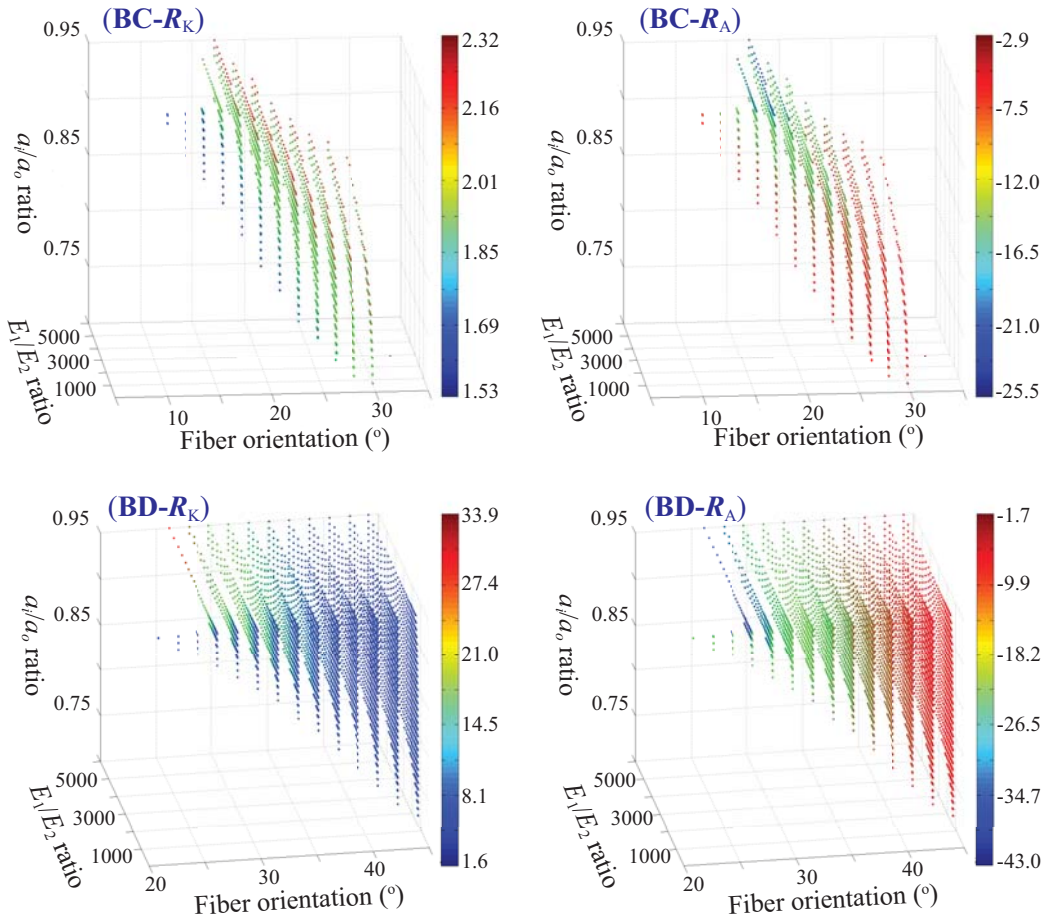

Figure 6.10 A sample synthesis result for cell #1. Each point represents a feasible F^{2}MC design in terms of its physical design parameters and reaches the same spectral data target. The top two sub plots are of (BC) type of architecture, while the lower two are of (BD) type. The colors of left two plots demonstrate the variable stiffness ratio, while the colors of the right two demonstrate the static actuation authority. One unit in R_A is equivalent to 1.17×10^{-4} inch of end mass displacement per psi of internal pressure, and positive and negative value of R_A corresponds to the direction of end mass displacement as defined in figure 6.3.

Such unique combination of variable stiffness and static actuation performance can be better illustrated by plotting the same design points in figure 6.10 in a different set up as shown in figure 6.11. In this figure, the synthesis results of the (AC) and (AD) are also

included. Different architecture designs demonstrate quite different combination of variable stiffness and actuation performance, even though they satisfy the same requirements on spectral data. Again, due to the nature of this discrete numerical survey, all of the design points are actually spanning a continuous performance space, which is estimated by the gray area. This plot also revealed a great advantage that, based on this particular set of spectral data target, higher variable stiffness ratio and larger magnitude actuation authority usually comes together.

The difference of performance range between the four architectures is best illustrated in a heat map in figure 6.12. In each heat map, the target zero ω_{z_f} is fixed at 35Hz, while the two target poles are allowed to vary, therefore, each pixel in the heat map corresponds to a unique combination of target (I) pole and zeros. Then the synthesis procedure laid out in figure 6.9 is applied at each pixel, and the results of the synthesis are represented by the pixel color. In the first row of heat maps, the color maps represents the number of physically feasible $\left[\Psi_1, \Psi_2\right]$ designs that can satisfy target (I) and (II). The number of feasible designs could be interpreted as the size of the physical design space for the F^2MC cells as shown in figure 6.10. The higher the number of designs, the larger the design space becomes. The white region in the heat maps represents the target spectral data combinations that cannot be achieved. The pixel color in the second row of heat maps represents the maximum variable stiffness ratio while satisfying the spectral data requirement; while the third row represent the maximum static actuation authority.

Among the four types of architectures, (BD) stands out regarding to the variable stiffness performance, while a subset of (AC) designs stands out in static deformation. The (BC) type of architecture is the least performing one. It is worth emphasizing that these

results are based on 35Hz of target zero ω_{z_f}, so setting the target zero at different value could lead to a different conclusion. Nonetheless, a heat map like this demonstrate the rich design versatility offered by the F^{2}MC based dual cellular structure, as well as the capability of the proposed synthesis procedure.

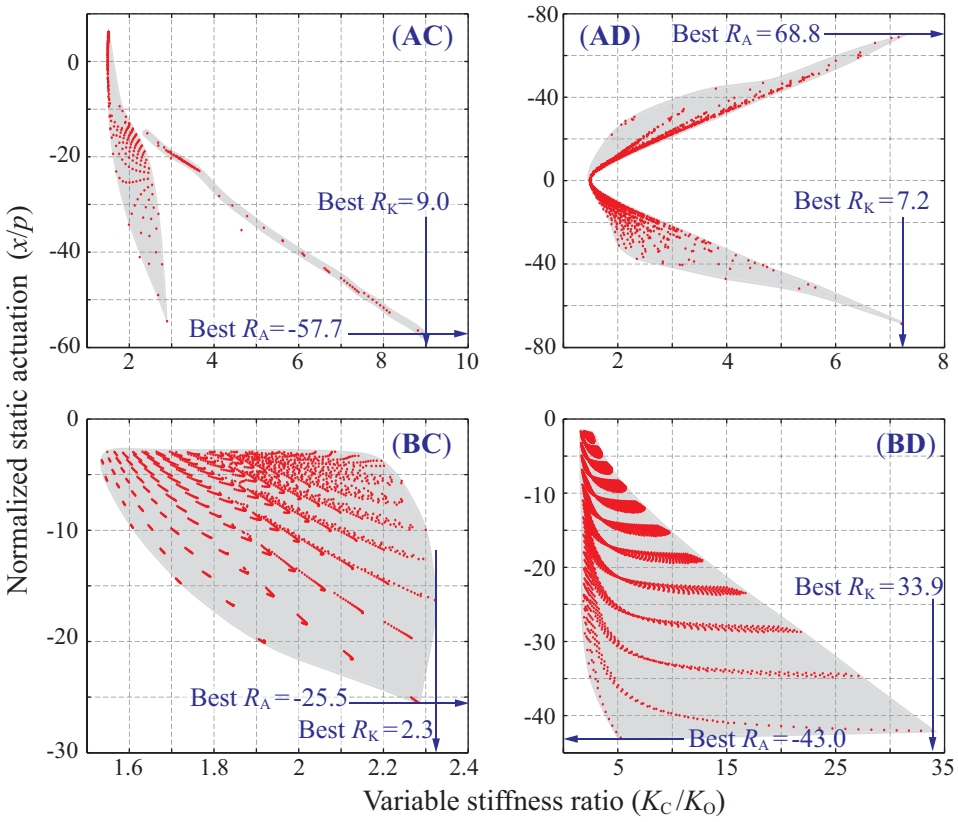

Figure 6.11 Combination of variable stiffness and actuation authority based on the same spectral data target. This figure includes the same results as in figure 6.10, but presents them in a different setup. The discrete design points are actually spanning a continuous performance range, as estimated by the gray area.

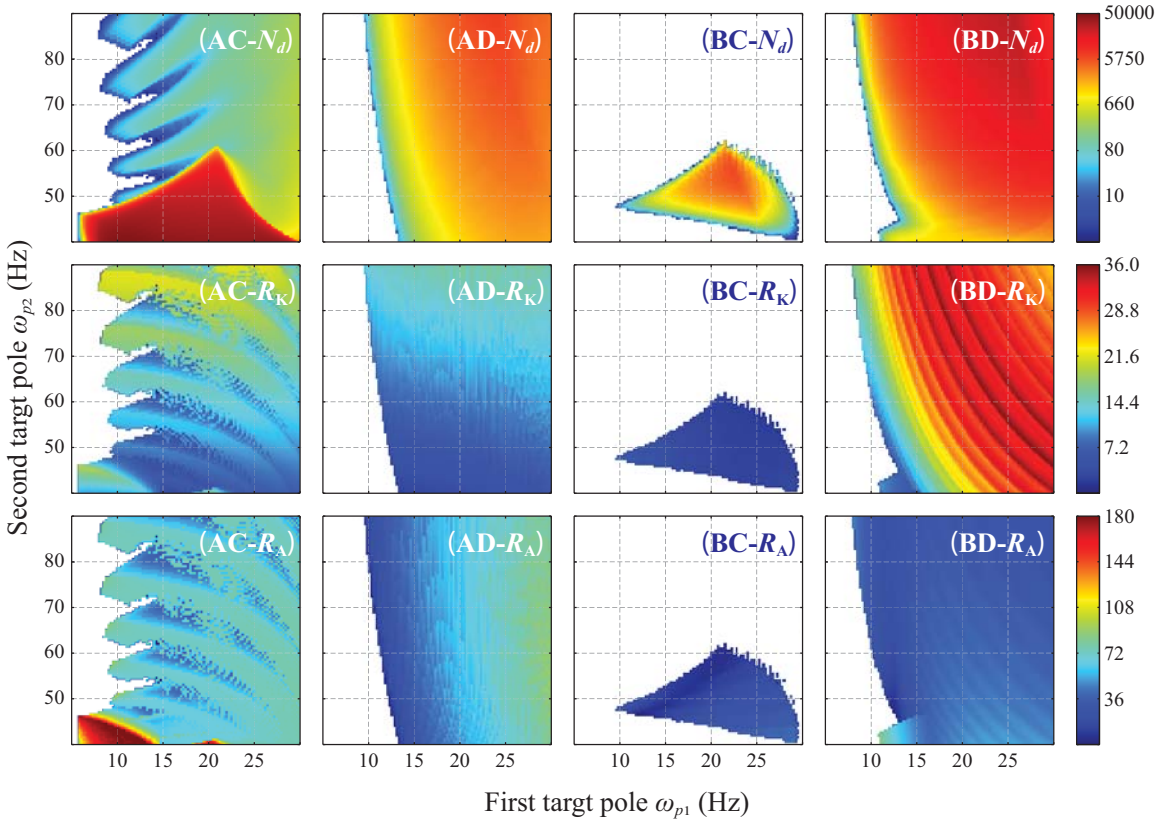

Figure 6.12 Heat map summarizing the results of a performance survey. The target zero ω_{zf} is fixed at 35Hz. In the subplots of the first row, the pixel color represents the size of the design space; the second row represents the maximum variable stiffness ratio; the third row represents the largest static actuation magnitude. The four columns are the results from the four architectures. Note that the color map of the first row results is in logarithm scale.

6.3 Summary

To fulfill the original research vision of developing adaptive structures with multiple and concurrent functionalities, this chapter matures the knowledge base and design tools of the F^{2}MC based cellular structure. Two crucial issues are identified from the efforts presented in the previous chapters: limited cellular structural design and limited synthesis targets. These issues prevent us from fully exploiting the potential of F^{2}MC based cellular structure to satisfy the various demands from different engineering applications.

To address the first issue, four unique types of architectures are identified for a dual cellular structure based on rigorous mathematical principles. These architectures differ from each other based on the type of fluidic and kinematic connection between the two F^2MC cells. A list of unique architectures offers the engineers a comprehensive library to foster unique designs of F^2MC based structure for various applications. The equations of motion of the four architectures are derived and then experimentally tested. To address the second issue, a more comprehensive synthesis procedure is derived, incorporating a variety of the synthesis target that covers the static and dynamic functionalities discussed in the previous chapters. The case studies presented in this chapter demonstrate the strong design versatility of the F^2MC based cellular structure; they also demonstrate the capability of the synthesis procedure to select appropriate F^2MC designs efficiently.

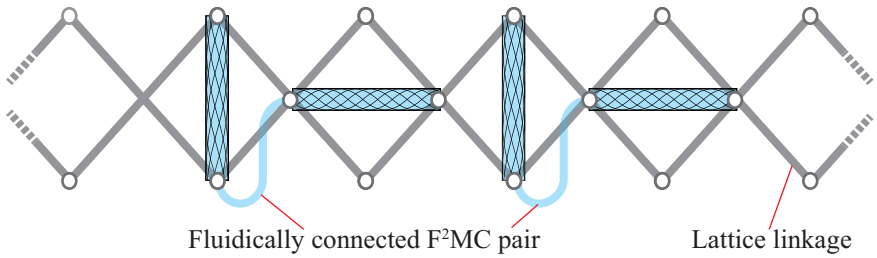

Figure 6.13 Illustration of extending the dual cellular unit into a larger scale structure. In this system, several pairs of fluidically connected, (AD) type of unit is assembled together into an active lattice.

Finally, the outcome of this chapter advances the proposal at the end of previous chapter. The multi-cellular synthesis of last chapter suggests that connecting more than three cells directly through fluidic circuit seems to make the system too complex to be analyzed and synthesized efficiently based on the analysis and synthesis model developed

in this thesis work. Therefore, it is suggested to focus on the design and synthesis of dual or triple cell system as a structural unit, and then incorporate these units mechanically into a larger-scale cellular structure. This is essentially a hierarchical concept: the individual F^2MC cell is the most basic structural level; the fluidically connected pair or triple is the higher level, in this level multiple-functions are achieved; and finally, the assembly of many F^2MC pair is the highest level (an example is illustrated in figure 6.13). The library of architectures from this chapter provides the guideline to integrate dual and triple cellular structure unit together into larger scale. And the comprehensive synthesis procedure can be utilized to design the dynamic characteristics and static functionalities of these pairs individually, so that the overall structural performance can be tailored and optimized for various engineering applications.

By this hierarchical approach focused on pairs or triples of fluidically connected cells, the rich list of adaptive functions from the F^2MC based cellular structure can still be achieved with great versatility, while the complexity regarding to synthesis can be kept at a manageable level. On the other hand, limiting the fluid circuits to every pair or triple of F^2MC cells can increase implementation difficulty in practical applications, because more valves, pressure supplies and control units are needed for such de-centralized and distributed fluidic system, especially when the cellular structure is to be miniaturized. The practical implementation is out of the scope of this thesis research, however it is recommended that the trade-off between performance versatility (the number of F^2MC pairs or triples) and the practical implementation difficulty shall be considered for specific application requirements.

Chapter 7
Concluding Remarks and Recommendation for Future Work

7.1 Concluding remarks

This thesis research takes the inspirations from plants to advance state of art of the F^2MC based multi-cellular structure to achieve multi-functionalities concurrently. It fosters a paradigm shift from individual cell oriented development to multiple-cell based study, where different F^2MC cells can be fluidically connected. This thesis brings major academic contributions with new analysis models, physical insights, and design methodologies that are never discussed before, and they are summarized as follows,

- It develops a dynamic model to characterize the fluidic interaction between different F^2MC cells that involves the cell wall anisotropy and fluid inertia, and discovers new functionalities from the F^2MC based cellular structure.
- By non-dimensionalizing the dynamic model, this thesis identifies critical *performance parameters* for the individual F^2MC cell. Based on these parameters, a performance space is constructed to explore the versatility of the cellular structure, and the analysis and synthesis work is significantly simplified.

- It provides a library of architecture designs of the dual F^2MC cellular structure unit based on rigorous mathematical principles. These architectures could be practical guidelines for developing larger-scale cellular structures with many cells.
- It derives comprehensive synthesis procedures for the F^2MC based cellular structure, so that appropriate designs parameters can be assigned to each cell in order to achieve different types of structural performance targets concurrently.

These contributions are the fruits of four progressive research thrusts, and the potential impact of the F^2MC based cellular structure is being manifested wider and deeper as the work progresses.

In the first thrust (chapter 3), the dynamic characteristics of a dual F^2MC cellular string structure are investigated, where the two cells differ from each other in fiber orientation and they are connected through a simple internal flow port. An analytical model is developed, analyzed, and experimentally tested in order to describe the dynamic characteristics of the cellular structure, especially the interaction between different F^2MC cells through fluidics. Based on the analysis, two new dynamic functionalities are investigated: vibration absorber in a passive operation condition and in active operation, resonance actuation with an enhanced actuation authority within a designated frequency band. This first thrust of research focuses on the parameter modeling and function analysis, it expands the list of feasible adaptive functions for the F^2MC based structure; it also extends the study from static to dynamic regime.

The second thrust of the thesis research deepens our understanding of the physics behind the F^2MC based dual-cellular structure, and it also brings the first attempt on synthesis procedure (chapter 4). A non-dimensional dynamic model is derived for the same dual cellular structure as in the first thrust. Based on this model, it is learned that the overall dynamics of the cellular structure is directly correlated to three factors: the closed valve stiffness of the individual F^2MC cell, the internal pressure difference between the cell, as well as the volume of static fluid displacement through the flow port. Furthermore, based on the new model, three *performance parameters* are identified and experimentally verified for the individual F^2MC cell. The definition of these parameters reveals the most significant design variable groups. Utilizing these parameters can significantly simplify the mathematical derivation so that a synthesis problem can be developed. This procedure can select appropriate F^2MC design to reach a desired system pole and zero position (spectral data), which is closely related to the dynamic functionalities discussed in the first thrust. Case studies illustrate that for a set of desired spectral data, the corresponding F^2MC designs are not unique, forming a design space. This non-uniqueness demonstrates the versatility in the design of the F^2MC cellular structure, and it also offers engineers the freedom to incorporate more design considerations for more sophisticated performance optimization.

In the third research thrust (chapter 5), the quest of deriving rigorous synthesis procedure is extended to the string cellular structure with more cells. The non-dimensional dynamic model is extended based on the performance parameters of individual F^2MC cells. This model is applicable to any number of F^2MC cells and it helps reveal the linkage between the individual cell performance and the overall structural dynamics. Based on this

model, a hybrid synthesis procedure for a multi-cellular structure is then developed. This procedure combines Jacobi inverse eigenvalue problem (JIEP) solver and the genetic algorithm with discrete variable in order to address the two technical challenges: 1) the complicated nonlinear and under-determined relationship between cellular parameters and system spectral data, and 2) the difficulty of implementing physical constraints onto F^2MC designs. The synthesis case studies demonstrate that the proposed procedure can effectively select triple F^2MC cellular design parameters to accurately achieve the target spectral data. On the other hand, further case studies revealed that the proposed procedure is no longer accurate for structure with more than three cells. This suggests that connecting more than three cells directly by an internal fluidic circuit may make the system too complex to be analyzed and synthesized efficiently.

Following the conclusion from thrust 3, the last thrust of this research returns the focus to dual cellular structure to mature our knowledge base and synthesis methodologies in order to fulfill the original research vision of achieving multi-functionality concurrently (chapter 6). This thrust of research consolidates the lessons and experiences from the previous thrusts, and identifies two crucial issues to be addressed: limited cellular structural design and limited synthesis targets. To address the first issue, four unique types of architectures are identified for a dual cellular structure based on rigorous mathematical principles. These architectures differ from each other based on the selection of fluidic and kinematic connections between the two F^2MC cells. A list of unique architectures offers the engineers a comprehensive library to foster unique design of F^2MC based structure for a variety of applications. The equations of motion of the four architectures are derived and

experimentally tested. To address the second issue, a more comprehensive synthesis procedure is developed, incorporating a variety of the synthesis target that covers the static and dynamic functionalities discussed in the previous thrusts. Case studies demonstrate the strong design versatility of the F^2MC based cellular structure; they also demonstrate the capability of the synthesis procedure to select appropriate F^2MC designs efficiently.

Many of the analysis on the dual cellular structures are experimentally tested, and during these experimental efforts, the variation of effective bulk modulus of the working fluid has significant effects on the system characteristics. It is usually much lower than the 2GPa ideal value, probably due to the entrapped air bubble in the fluid circuit as well as some un-modeled structure compliance, such as the elasticity of the flow port wall or dead fluid volume in the fluid circuit. Since the effective bulk modulus has a significant influence of the system response, and the modulus values fluctuates among different test set ups thought out the thesis research, it is recommended to further investigate the root cause of the lower than ideal fluid modulus. For this purpose, more sophisticated study in fluid mechanics within each cell, such as acoustic wave propagation, as well as the fluid-structure interaction might be necessary. The simple flow port resistance model employed in the thesis also under-estimates the actual energy dissipation in the pulsating fluid flow between cells. To ensure a consistent performance, careful fluidic circuit design is necessary. This is not the core focus of the thesis research, but is recommended for practical applications.

The analysis and synthesis results of this thesis research suggest a viable approach to develop larger-scale cellular structure with many F^2MC cells for a more sophisticated functionality. Instead of fluidically connecting many F^2MC cells all together, it is more

efficient to assemble many pairs or triples of fluidically connected F^2MC cells mechanically into a larger scale structure, and utilize the synthesis tools from this thesis to design the structural performance based on the unit pairs or triples. The static and dynamic functionalities of these units can be tailored separately to fine-tune the performance of the overall structure.

Therefore, in final conclusion, the deep physical knowledge, architectural design methodologies, and the comprehensive synthesis tools developed from this thesis research have successfully addressed the problem statements and advanced the state of art. They fully manifested the rich functionality and designs versatility of the F^2MC based cellular structure, and laid down a solid foundation for the bio-inspired, bottom-up, and hierarchical approach towards the larger-scale adaptive cellular structures. The results of this thesis could foster the adoption of F^2MC based structure to a variety of engineering applications with unique performance requirements, such as morphing air vehicles, soft robotics, as well as intelligent civil infrastructure. Furthermore, the plant inspired cellular design principles in this thesis can be applied to other types of adaptive structure disciplines, such as piezoelectric, shape memory alloy, or active honeycomb structures, creating broader impact to the discipline.

7.2 Recommendation for future work

At the end of chapter 6, a viable approach to develop a larger-scale F^2MC based cellular structure is proposed, such structure consists of many pairs and triples of fluidically connected F^2MC cells. Therefore, it is recommended that future research effort can focus onto the higher-level design methodology and synthesis tool development on such large-

scale cellular structure. It is essentially a hierarchical approach: the previous research on F^2MC before this thesis was mainly on the most basic individual cell level; the current thesis work is mainly on the level of dual and triple cellular structural unit, where multi-functionality can be achieved; and the future work can move to an even higher level. There are two potential topics worthy investing. The first topic is the topology layout. When a large number of F^2MC pairs, each with their own unique architectures, are assembled, it will be challenging to efficiently distribute and connect them. A mathematical robust synthesis procedure is necessary. The second topic is to explore new functionalities from the large-scale structural layout. There is a recent rise of research attention to the "meta-structure" or "meta-material" concept that can exhibit unique properties unseen from nature, such as negative stiffness or wave cloaking. These unique properties are achieved by distributing "modules", or basic structural elements, in a periodic pattern at a designated length scale. The dual F^2MC cellular unit, with its design versatility and rich functionality, could be a good candidate as a base module. Brand new types of functionalities, other than those reported in this thesis, can be achieved by the large-scale cellular structure.

This thesis research identified several design principles from the plant world to advance the state of art of the F^2MC based structure. Some of these principles are not limited to F^2MC. For example, the advantage of multi-cell layout can be exploited for other forms of cellular structure such as active honeycomb core; and the principle of fibrillar organization and its differentiation can be applied to the shape memory alloy wire based structures. Therefore, it is recommended to extend the inspirations from plants to advance the development of other types of adaptive structures.

Collaborative research is also recommended for future work, especially with material scientist and biomedical engineering researchers. The F^2MC cell sample utilized in this study is relatively large, and developing robust technique to miniaturize the F^2MC could open up new areas of potential application. Furthermore, the synthesis case studies in this thesis suggest the importance of precision manufacturing, as the success of the synthesis results relies on accurately fabricated F^2MC cells. Miniaturization and precision fabrication are not trivial on F^2MC because of the elastomer based soft matrix material. Pumping and valve control is another essential element for the F^2MC based structure performance. In the thesis, the usually bulky conventional valve and pumping techniques are utilized. Plant inspired pumping and fluid circuit control technologies, such as osmosis, are being developed by the biomedical engineers, and it is recommended to integrate such technologies seamlessly with the F^2MC based cellular structures in the future.

Appendix A
Uniform Pressure Assumption in a Single F^{2}MC Cell

Throughout the analysis of the F^{2}MC cell wall constitutive relationship, the working fluid pressure is always assumed to be uniform inside the cell, so that pressure gradients only exist between the two ends of the thin flow port. This is essentially a low frequency assumption, because at a higher frequency the fluid pressure propagation might form a higher order standing wave within. Therefore, it is necessary to estimate the frequency bandwidth where such uniform pressure assumption is correct. To do this, one can compare the pressure propagation wavelength to the F^{2}MC cell length. And the uniform pressure assumption should be accurate if the cell length is smaller than a quarter of the wavelength, which corresponds to the first fundamental fluidic standing wave mode.

This thesis adopts the work of Kuiken (1984) to estimate the wavelength. In his work the linearly compressible fluid is assumed to be confined in a long, thin-walled, elastically orthotropic circular tube with pre-stress and static internal pressure. This is quite close to the case of F^{2}MC. Denote $\bar{k}$ as the ratio between wave phase velocity c and a reference velocity c_0 $\left(\bar{k} = c_0/c\right)$, the dispersion equation for wave propagation can be written as an algebraic equation of $\bar{k}$ in fourth order:

$$\begin{aligned}&\bar{k}^4\left(1-F\right)B' + \bar{k}^2\left\{F\left[B'_{12}+B'_{21}-0.5\left(B'_{11}+K'_r\right)\right]-\left(2B'_{22}+B'\beta_{0\mathrm{T}}^2\right)\ldots\right.\\&\left.+\left(K'_x/\beta^2\right)\left(B'_{11}+K'_r\right)\left(1-F\right)\right\}+\left[F-2\left(K'_x/\beta^2\right)\right]\left[1+0.5\left(B'_{11}+K'_r\right)\beta_{0\mathrm{T}}^2\right]=0,\end{aligned} \tag{A1}$$

where the various parameters in this equation are defined as

$$F = \frac{2J_1(\mathrm{i}^{3/2}\alpha)}{\mathrm{i}^{3/2}\alpha J_0(\mathrm{i}^{3/2}\alpha)}, \tag{A2}$$

$$B'_{11} = \frac{B_{11}}{\rho a c_0^2}, \tag{A3}$$

$$B'_{12} = B'_{21} = \frac{B_{12} - S_\theta}{\rho a c_0^2}, \tag{A4}$$

$$B'_{22} = \frac{B_{22} + S_x}{\rho a c_0^2}, \tag{A5}$$

$$K'_r = K'_x = -\left(\frac{\rho_w h}{\rho a}\right)^2 \beta^2, \tag{A6}$$

$$B' = B'_{22}\left(B'_{11} + K'_r\right) - B'_{12}B'_{21} + \frac{S_x}{\rho a c_0^2} K'_x, \tag{A7}$$

where $J_n(x)$ in equation (A2) is the n^{th} order Bessel function of type J, and B_{ij} in equation (A2-A7) are related to the cell wall laminate elastic modulus as follows:

$$B_{11} = \frac{E_\theta h}{1 - \nu_x \nu_\theta}, \tag{A8}$$

$$B_{22} = \frac{E_x h}{1 - \nu_x \nu_\theta}, \tag{A9}$$

$$B_{12} = B_{21} = \frac{E_\theta h \nu_x}{1 - \nu_x \nu_\theta}, \tag{A10}$$

where E_x, E_θ, ν_x, and ν_θ are the laminate axial elastic modulus, circumferential modulus, and Poisson's ratio, respectively. These values can be calculated based on the three-dimensional laminate theory proposed by Sun (1998).

K_r' and K_x' are related to the cell well inertia, and S_x and S_θ in equation (A2-A7) are related to the static pre-stress inside of the F^{2}MC cell,

$$S_x = \frac{ap_i}{2} + \frac{N_x}{2\pi a}, \tag{A11}$$

$$S_\theta = p_i a. \tag{A12}$$

Other parameters in equation (A1) are defined as follows,

$$\alpha = a\left(\frac{\omega\rho}{\mu}\right)^{1/2}, \tag{A13}$$

$$\beta = \frac{\omega a}{c_0}, \tag{A14}$$

$$\beta_{0\mathrm{T}} = \frac{c_0}{c_\mathrm{T}}, \tag{A15}$$

where ω is the angular frequency; c_0 and c_T are the reference velocity and thermodynamic speed of sound, respectively:

$$c_0 = \left(\frac{\frac{B_f}{\rho}}{1+2\frac{B_k}{E_\theta}\frac{2a}{h}\frac{1-\nu_x\nu_\theta}{1+K_r/B_{11}}}\right)^{1/2}, \tag{A16}$$

$$c_{\mathrm{T}} = \left(\frac{B_f}{\rho} \right)^{1/2}. \tag{A17}$$

Equation (A1) can then be solved for $\bar{k}$, and the pressure propagation wavelength is simply calculated as

$$\lambda = \frac{1}{f} \frac{c_0}{\bar{k}_1}, \tag{A18}$$

where $\bar{k}_1$ is the real part of the first root of $\bar{k}$ in equation (A1). Note that the wavelength calculation is a low-frequency estimation and is accurate only when $\beta^2 \ll 1$.

The wavelength estimation in this appendix is not intended to be a comprehensive investigation on the fluid-structural interaction inside of the F^{2}MC cell wall, so it serves only to provide a rule-of-thumb estimate on the frequency bandwidth where the uniform-pressure assumption is valid. To assist this analytical estimation, a simple experiment is carried out in parallel. In this experiment, a piezoelectric dynamic pressure transducer (PCB 101A06) is connected to the end of a F^{2}MC cell which is filled with working fluid and attached to an end mass, and the cell is kept at closed valve state. An accelerometer is attached to the end mass with a shaker providing frequency sweep excitation (figure A1). If the uniform pressure assumption holds valid as in equation (3.19 and 20), the acceleration to pressure oscillation relationship ($\ddot{x}/p$) should be simply:

$$\left| \frac{\ddot{x}}{p} \right| = \frac{AD^* - BC^*}{Al} \omega^2, \tag{A19}$$

which would show up as a parabola curve in the $|\ddot{x}/p|$ versus frequency plot.

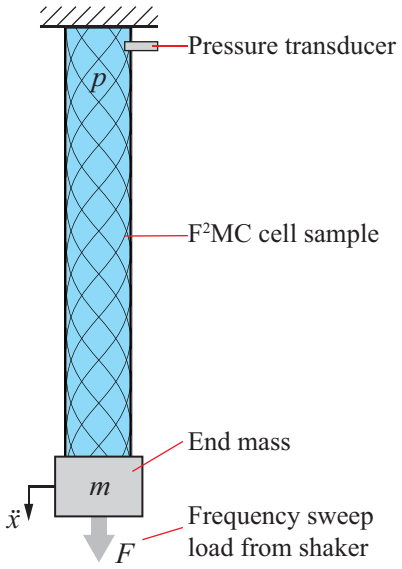

Figure A1 Experiment setup to test the bulk pressure assumption. The purpose of this experiment is to measure the ratio of end mass acceleration to the dynamic internal pressure oscillation at different frequency.

Figure A2 summarize the wavelength calculation based on (A1) and experiment results from two sample F^2MC cells; the material properties of these two sampled are summarized in table A1 (these two F^2MC samples come from the experiment efforts in chapter 4). As can been seen, the bulk-pressure assumption holds valid until the frequency of interest increase to about 70-100Hz. At this frequency range, the quarter wavelength decreases to the sample length, and the acceleration to pressure ratio starts to deviate from the ideal parabola curve defined by equation (A19). While adjusting some system parameters can increase the uniform pressure frequency bandwidth, such as decreasing the F^2MC cell length, it is still recommended, based on the available F^2MC samples, that the frequency of interest throughout this thesis research will be limited below 100Hz, and the analysis in this appendix should be applied to different F^2MC cellular structure set-up to guarantee the accuracy of the uniform pressure assumption.

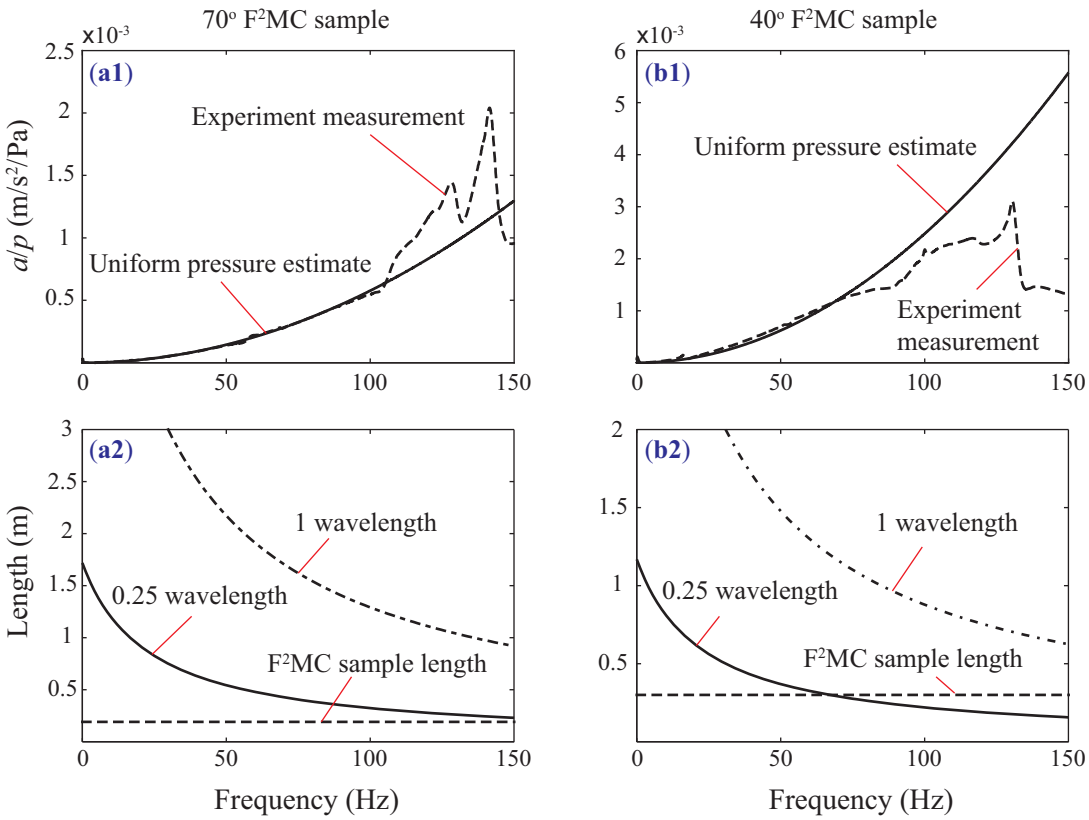

Figure A2 Wave length calculation based on equation (A1), and corresponding experiment verification results. (**a1**): the acceleration to pressure ratio of the ±70° F²MC sample, the measurement data starts to deviate from the uniform pressure estimate at about 100Hz, indicating that some higher order fluid dynamic starts to occur above this frequency. (**a2**): The wavelength calculation inside of the ±70° F²MC sample; the quarter wave length is very close to tube length at 100Hz, which agrees with the experiment. The experiment and analysis on the ±40° F²MC sample in (**b1**) and (**b2**), respectively, give similar observation at about 75Hz.

Table A1 Material parameters for calculating the fluid wave speed.

Properties	Value	Properties	Value
E_1 (figure 2.1)	120 GPa	E_2, E_3 (figure 2.1)	50 MPa
Cell radius (a)	10 mm	Cell wall thickness (h)	2.7 mm
Fluid density (ρ)	1000 kg/m^3	Cell wall density (ρ_w)	1100 kg/m^3
Fluid bulk modulus (B_k)	20 MPa	Dynamic viscosity (μ)	1.002×10^{-3} Pa sec
Internal pre-pressure (p_i)	138 KPa	Axial pre-stress (N_x)	70 N

Appendix B
Derivation of A, B, C, and D in (3.19 and 20)

$$A = \pi a_i^2 l \left[-2\beta_{r\theta} + 2\kappa\beta_{\theta\theta} \frac{1+c^{2\kappa}}{1-c^{2\kappa}} + \frac{1}{B_f} \right] \tag{B1}$$

$$B = \pi a_i^2 l \left[\frac{2h\beta_{\theta\theta}}{a_{xx}} \frac{(\kappa+1) - 2\kappa c^{\kappa-1} + (\kappa-1)c^{2\kappa}}{1-c^{2\kappa}} + 2\frac{a_{\theta x}}{a_{xx}} + 1 \right] \tag{B2}$$

$$C = \frac{2\pi a_i^2}{a_{xx}} \left[\frac{a_{rx} + \kappa a_{\theta x}}{\kappa+1} \frac{c^{2\kappa} - c^{\kappa-1}}{1-c^{2\kappa}} + \frac{a_{rx} - \kappa a_{\theta x}}{\kappa-1} \frac{1-c^{\kappa-1}}{1-c^{2\kappa}} - \frac{a_{xx}}{2} \right] \tag{B3}$$

$$\begin{aligned} D = \quad & \frac{2\pi a_i^2}{a_{xx}^2} \left[h \frac{a_{rx} + \kappa a_{\theta x}}{\kappa+1} \frac{(c^{\kappa} - c^{-1})^2}{1-c^{2\kappa}} + h \frac{a_{rx} - \kappa a_{\theta x}}{\kappa-1} \frac{(1-c^{\kappa-1})^2}{1-c^{2\kappa}} \cdots \right. \\ & \left. - \frac{(a_{xx} - h a_{rx} - h a_{\theta x})(c^{-2} - 1)}{2} \right] \end{aligned} \tag{B4}$$

Appendix C
Effects of Flow Port Intrusion into F^{2}MC Cell

To estimate the effects of flow port intrusions onto the dynamic characteristics of the system, one can derive the transfer function of the proposed dual cell string structure with the flow port transfer matrix in equation (3.24) in Laplace (frequency) domain.

The system transfer function can be obtained by combining the F^{2}MC cellular constitutive relationship equation (3.19 and 20), the flow port equation considering the intrusion (3.21, 24 and 25) and the end mass dynamic equation as follows,

$$-\omega^2 X + f_2 = F_e, \tag{C1}$$

where X is the magnitude of end mass displacement, $X = \left\| l_1\varepsilon_1 + l_2\varepsilon_2 \right\|$ (assuming the two F^{2}MC cell have the same length l). Denote a parameter related to the effects from intrusion as,

$$\kappa_m = \frac{l_{i_m} S_2}{\rho c^2}, \quad m = 1, 2. \tag{C2}$$

The transfer function can be written as polynomial function of ω:

$$\frac{X}{F_e} = \frac{P_0 l + P_2 l I \omega^2}{Q_0 + Q_2\omega^2 + Q_4 m l l \omega^4}. \tag{C3}$$

The constants for the polynomials are as follows:

$$P_0 = -\left(\underline{A_1 - \kappa_1} + \underline{A_2 - \kappa_2}\right)\left(D_1 + D_2\right) - \left(B_1 - B_2\right)\left(C_1 - C_2\right), \tag{C4}$$

$$P_2 = -\left(\underline{A_1 - \kappa_1}\right)\left(\underline{A_2 - \kappa_2}\right)\left(D_1 + D_2\right) - B_1 C_1\left(\underline{A_1 - \kappa_1}\right) - B_2 C_2\left(\underline{A_2 - \kappa_2}\right), \tag{C5}$$

$$Q_0 = -D_1 B_2 C_2 - D_2 B_1 C_1 + D_1 D_2\left(\underline{A_1 - \kappa_1} + \underline{A_2 - \kappa_2}\right), \tag{C6}$$

$$\begin{aligned} Q_2 = \quad & ml\left[\left(B_1 - B_2\right)\left(C_1 - C_2\right) - \left(D_1 + D_2\right)\left(\underline{A_1 - \kappa_1} + \underline{A_2 - \kappa_2}\right)\right] + \ldots \\ & I\left[B_1 C_1 - D_1\left(\underline{A_1 - \kappa_1}\right)\right]\left[B_2 C_2 - D_2\left(\underline{A_2 - \kappa_2}\right)\right] \\ & D_1 D_2 I\left(\underline{A_1 - \kappa_2}\right)\left(\underline{A_1 - \kappa_2}\right), \end{aligned} \tag{C7}$$

$$Q_4 = B_1 C_1\left(\underline{A_2 - \kappa_2}\right) + B_2 C_2\left(\underline{A_2 - \kappa_2}\right) - \left(\underline{A_1 - \kappa_1}\right)\left(\underline{A_2 - \kappa_2}\right)\left(D_1 + D_2\right). \tag{C8}$$

As can be seen from the underlined part of these equations, the intrusion parameter κ_1 and κ_2 always come in pair with A_1 or A_2. Therefore, if the value of κ_1, κ_2 is a magnitude smaller than A_1, A_2, the effects of flow port intrusion is negligible. Similar to the recommendation at the end of appendix A, it is also recommended that this intrusion parameter be estimated for different F^{2}MC based cellular structure design to guarantee that the simple flow port equation employed in the thesis research is valid.

Appendix D
Measure the Constitutive Parameters of F^{2}MC Cell

When the F^{2}MC cell is empty, the internal pressure p is zero, so the experimental set up in figure 4.4 can be treated as a simple spring-mass oscillator, in which the equivalent spring stiffness of the F^{2}MC cell (K_e) is calculated directly from the measured natural frequency:

$$K_e = \omega_n^2 m, \tag{D1}$$

where K_e is related to the dimensionless parameter $\hat{\delta}$ as follows

$$\hat{\delta} = \frac{K_e g}{\pi a_i E_2}, \tag{D2}$$

which gives equation (4.19). When the F^{2}MC cell is filled with working fluid as in figure 4.4, the system equation in (4.5, 6, 13, and 15) can be simplified as:

$$\begin{cases} -\hat{v} = g\hat{\alpha}\hat{p} + \hat{\beta}\hat{\varepsilon} \\ \hat{f} = -\hat{\beta}\hat{p} + \hat{\delta}\hat{\varepsilon}/g \\ 0 = \hat{I}_e \dfrac{\mathrm{d}^2\hat{v}}{\mathrm{d}\tau^2} - \hat{p} \\ \hat{f}_e = \hat{m}\dfrac{\mathrm{d}^2\hat{x}}{\mathrm{d}\tau^2} + \hat{f} \end{cases}. \tag{D3}$$

Then the zero for $\hat{\varepsilon}/\hat{f}_e$ can be calculated as $\hat{\omega}_z^2 = \left(\hat{I}_e g\hat{\alpha}\right)^{-1}$, where the dimensionless frequency $\hat{\omega}_z$ and port inertance $\hat{I}_e$ is related to their full dimensional values as follows,

$$\begin{cases} \hat{\omega}_z^2 = \dfrac{\omega_z^2 \rho a_i^2}{\pi E_2} \\ \hat{I}_e = \dfrac{I_e \pi^2 a_i}{\rho} \end{cases} . \tag{D4}$$

(D3) and (D4) together give (4.20).

Appendix E
MATLAB Script of the Multiple Cellular Structure Synthesis

```
% ================================================================== %
% This is the master synthesis routine for the multi F2MC-cellular   %
% string structure to achieve a prescribed spectral data. This script %
% is applicable to a string structure with any number of cells.  But  %
% case study proved it most accurate for triple cell structure.       %
% ================================================================== %

function [SOL] = TriCellSyn()
% reset the system                                                    %
clear;
clc;
close all;

% ============ Initialize the cellular structural design ============ %
n      = 3;                     % number of cells                     %
ri     = 0.01;                  % F2MC cell inner radius (m)          %
g      = 20;                    % cell geometric shape aspect ratio   %
l      = ri*g;                  % cell length (m)                     %
m      = 0.20;                  % end mass (kg)                       %
rho    = 1000;                  % working fluid density (kg/m^3)      %
lf     = 0.20;                  % flow port length (m)                %
lr     = 0.005;                 % flow port radius (m)                %
E2     = 50e6;                  % fiber ply transverse modulus (Pa)   %
Bk     = 20e6;                  % fluid bulk modulus (Pa)             %

M      = m/rho/ri^3;            % normalized end mass                 %
I      = pi*lf*ri/lr^2;         % normalized flow port inertia        %
tau    = ri*sqrt(rho/pi/E2);    % time unit (s)                       %

Msys   = [M 0 0; 0 I 0; 0 0 I]; % normalized inertia matrix           %

%% ================== Construct the Omega space ===================== %
N      = 50;                    % size of each parametric sub-space   %
id1    = 1:N;
id2    = N+1:2*N;
id3    = 2*N+1:3*N;
[ang,era,wth] = designvar(N);   % the physical variables              %
% max(E1/E2) = 3000; min(E1/E2) =  50;                               %
% max(c1/c2) = 0.95; min(c1/c2) = 0.6;                               %

% prelocate the 148x50x50 grid that will span the Omega space        %
a       = zeros(3*N,N,N);       % alpha value of the 3D grid         %
b       = zeros(3*N,N,N);       % beta value of the 3D grid          %
d       = zeros(3*N,N,N);       % delta value of the 3D grid         %

% Calculate the Omega space based on "ang" "era" and "wth" values    %
[a(id1,:,:),b(id1,:,:),d(id1,:,:)] = ...
    paraspace(ri,l,Bk,E2,ang(1,:),era(1,:),wth(1,:));
[a(id2,:,:),b(id2,:,:),d(id2,:,:)] = ...
```

```
    paraspace(ri,l,Bk,E2,ang(2,:),era(2,:),wth(2,:));
[a(id3,:,:),b(id3,:,:),d(id3,:,:)] = ...
    paraspace(ri,l,Bk,E2,ang(3,:),era(3,:),wth(3,:));

% Note: the data of a, b, d, can be saved for future                    %
% synthesis, so that they don't need to be calculated every time.       %
save('a.mat','a');
save('b.mat','b');
save('d.mat','d');

% Delete the redundant data in a b and d                                %
a(101,:,:) = [];
a(51,:,:)  = [];
b(101,:,:) = [];
b(51,:,:)  = [];
d(101,:,:) = [];
d(51,:,:)  = [];

% ============== Adjust the bulk modulus on alpha  ================== %
a      = a  + E2/Bk;

%% ===================== Genetic Algorithm ========================== %
% Spectral data target, this is specifically for three-cell string     %
pztar   = [40; 60; 80; 50; 70];

ldt     = (pztar(1:3)*2*pi*tau).^2; % normalized pole positions        %
mut     = (pztar(4:5)*2*pi*tau).^2; % normalized zero positions        %

margn   = 2;
lb      = ones(1,3*n) + margn;  % lower index bound for GA code        %
ub      = repmat([148 50 50],[1 n])- margn;  % upper index bound       %
intcon  = 1:3*n;                % define the integer variables         %
popsiz  = 200;                  % define population size for GA        %

% assign the genetic algorithm conditions                               %
gaopt   = gaoptimset('Display','off',...
                     'Populationsize',popsiz,...
                     'Generations',400,...
                     'TolFun',1e-12,...
                     'MigrationFraction',0.2,...
                     'FitnessScalingFcn',@fitscalingtop,...
                     'CrossoverFraction',0.5,...
                     'PopInitRange',[1 1 1 1 1 1 1 1 1;...
                                     148 50 50 148 50 50 148 50 50],...
                     'vectorized','on',...'
                     'UseParallel','always',...
                     'PlotFcns',@gaplotbestf,...
                     'StallGenLimit',100);


% define the object function for the genetic algorithm                 %
G       = @(x)ind2res(x,a,b,d,Msys,tau,g,pztar);
% global optimization toolbox in MATLAB 2011b or above is required     %
disp('Running genetic algorithm...')

ncand   = 500;                  % number of candidate designs          %
elite   = 10;                   % count of the elite individuals       %
gacand  = zeros(100,3*n+1);

for ii = 1:(ncand/elite)
    gapop   = zeros(popsiz,3*n+1);
    % running genetic algorithm                                        %
```

```
    [~, ~, ~,~,gapop(:,2:end),gapop(:,1)] =...
           ga(G,3*n,[],[],[],[],lb,ub,[],intcon,gaopt);
    gapop  = sortrows(gapop,1); % sort the final population by score  %
    gacand((ii-1)*elite+1:ii*elite,:) = gapop(1:elite,:);
end

gacand  = sortrows(gacand,1);

% delete the repeated candidates in the genetic algorithm population  %
ref     = gacand(1,1);
for jj = 2:ncand
    if gacand(jj,1) == ref
        gacand(jj,1) = 0;
    else ref = gacand(jj,1);
    end
end
gacand(gacand(:,1) == 0,:) = [];

%% ============= calculate the final design candidate =============== %
siz    = size(gacand,1);
SOL    = zeros(siz,3*n+2);
chk    = zeros(siz,n);
SOL0   = zeros(siz,3*n);        % initial population for fsolve       %
scl    = [10 10 1];             % scale factor for delta values       %

% Translate the GA results from indecies to constitutive parameters   %
for ii = 1:n
    id     = (ii-1)*3+1;
    SOL0(:,id)   = a(sub2ind(size(a),...
                   gacand(:,id+1),gacand(:,id+2),gacand(:,id+3)));
    SOL0(:,id+1) = b(sub2ind(size(b),...
                   gacand(:,id+1),gacand(:,id+2),gacand(:,id+3)));
    SOL0(:,id+2) = d(sub2ind(size(d),...
                   gacand(:,id+1),gacand(:,id+2),gacand(:,id+3)));
end


for ii = 1:siz
    disp(['lookup ', num2str(ii), 'th candidate...'])
    % the object function to calculate final design candidate.        %
    F      = @(X)Eig2Cell(X,ldt,mut,g,Msys,tau);


    fopt   = optimset('Disp','off',...
                      'Algorithm',{'levenberg-marquardt',.1},...
                      'MaxFunEvals',8000,'TolFun',1e-6,...
                      'FinDiffType','central','FunValCheck','on',...
                      'ScaleProblem','Jacobian');

    % solving for the final solution                                   %
    [SOL(ii,3:end),~,~] = fsolve(F,SOL0(ii,:),fopt);

    % checking for the accuracy of the final solutions                 %
    SOL(ii,2) = sqrt(F(SOL(ii,3:end))'*F(SOL(ii,3:end)));

    % checking if the final design candidate is in Omega               %
    for jj = 1:n
        id          = 3*(jj-1)+3;
        chk(ii,jj) = chkOmega(SOL(ii,id), SOL(ii,id+1), SOL(ii,id+2),...
                     a,b,d,N,scl,n);
    end
```

```
    if sum(chk(ii,:)) == n
        SOL(ii,1) = 1;
    end

end

% take away the results that are not in Omega                          %
SOL(SOL(:,1)==0,:) = [];
SOL(1:2,:) = [];

% ===================================================================== %
% the output SOL is a matrix.  Each row of this matrix are an a-b-d    %
% values of the feasible triple cellular structure designs.            %
% Multiple rows means that multiple designs are found for the target   %
% spectral data.                                                       %
% ===================================================================== %

end % end of main function                                             %
```

```
function [ang,era,wth] = designvar(N)
% ===================================================================== %
% This is the subroutine to construct the F2MC physical variables      %
% ===================================================================== %
erai   = 50;
eraf   = 3000;
wthi   = 0.6;
wthf   = 0.95;

% set up the physical variables                                         %
Q      = (1:N)'-1;
q_ang1 = (30/1)^(1/(N-1));      % ratio of geometric series (angle)    %
ang1   = 1*ones(N,1).*(q_ang1.^(Q)); % array of fiber angle            %
q_ang2 = (50/30)^(1/(N-1));     % ratio of geometric series (angle)    %
ang2   = 30*ones(N,1).*(q_ang2.^(Q));% array of fiber angle            %
q_ang3 = (89/50)^(1/(N-1));     % ratio of geometric series (angle)    %
ang3   = 50*ones(N,1).*(q_ang3.^(Q));% array of fiber angle            %
ang = [ang1';ang2';ang3'];


q_era  = (eraf/erai)^(1/(N-1)); % ratio of geometric series (E1/E2)    %
era    = erai*ones(N,1).*(q_era.^(Q)); % array of E1/E2 ratio          %
era    = [era';era';era'];

wth    = (wthi:(wthf-wthi)/(N-1):wthf);% array of wall thickness ratio%
wth    = [wth;wth;wth];

end % end of subroutine "desinvar"                                     %
```

```
function [a,b,d] = paraspace(ai,len,~,E2,ang,era,wth)
% ========================================================================= %
% This is the subroutine to calculate the parametric (Omega) space        %
% ========================================================================= %
N      = length(ang);           % size of the parametric space             %
% initialize the parametric space                                          %
a      = zeros(N,N,N);
b      = zeros(N,N,N);
d      = zeros(N,N,N);

% populate the whole parametric space                                      %
disp('Populating the parametric space...')
for i = 1:N
    for j = 1:N
        for k = 1:N
            cpara  = cellpa(ang(i),ai,ai/wth(k),len,E2,era(j));
            % dimensionless constitutive parameters                        %
            a(i,j,k) = cpara(1)*E2/(pi*ai^2*len);
            b(i,j,k) = cpara(2)/(pi*ai^2*len);
            d(i,j,k) = cpara(4)/pi/E2/ai^2;
        end
    end
end

end % end of subroutine "paraspace"                                        %
```

```
function [cpara] = cellpa(fang,a1,a2,l,E2,ER21)
%  ================================================================  %
%  This subroutine calculate the constitutive parameters of a single  %
%  F2MC cell based on Lekhniski's solution (chapter 3 and 4)          %
%  V^net_k = alpha_k*p_k+beta_k*e_k                                   %
%  f_k     = gamma_k*(1+ii*etap_k)*p_k+delta_k*(1+ii*etaE_k)*e_k      %
%  ================================================================  %

%    I. ply dynamic modulus                                           %
%  eta2 are back calculated from experiments                          %
eta2   = 0.4;
%  estimating the ply modulus                                         %
E11    = ER21*E2;
E22    = E2;
E33    = E22;
G12    = 0.8*E2;
v12    = 0.33;
v23    = 0.93;
G23    = E22/2/(1+v23);
v13    = 0.33;
%  estimating other loss factors                                      %
eta11  = 0.011;
eta12  = eta2;
eta22  = eta2;
eta33  = eta22;

plyEij = [E11,E22,E33,G12,v12,v13,v23,G23];  % ply level Eij value    %
cellge = [fang,a1,a2,l];                     % cell geometry          %
etaij  = [eta11,eta12,eta22,eta33];          % loss coeffcient in ply %

%    II. laminate elastic modulus                                     %
[lamaij] = FMCini(plyEij,cellge);
%  The output is aij in following format                              %
%  lamaij = [arr ,art ,arx ;                                          %
%            atr ,att ,atx ;                                          %
%            axr ,axt ,axx];                                          %

%    III. internal absolute volume change                             %
%  vk  = ak*pk+bk*ek (a is alpha and b is beta )                      %
%  Fk  = ck*pk+dk*ek (c is gamma and d is delta)                      %
[a,b,c,d]  = F2MC(lamaij,cellge);

%    IV. cell damping coefficient                                     %
[etae, etap] = FMCdam(plyEij,cellge,lamaij,etaij);
cpara  = [a,b,c,d,etap,etae];
end % end of subroutine "cellpa"                                      %
```

```
% "FMCini" are adapted and optimized from the work of Shan (2006)     %
function [C]    = FMCini(plyEij,cellge)
% Initiate the FMC tube elastic properties w.r.t global coordinates   %
E11     = plyEij(1);
E22     = plyEij(2);
G12     = plyEij(4);
v12     = plyEij(5);
v23     = plyEij(7);
G23     = plyEij(8);
angle   = cellge(1);

FiberAngle  = [angle,-angle,-angle,+angle];
PlyNum      = length(FiberAngle);
Layer_Thickness     = [1,1,1,1];
Total_Thickness     = sum(Layer_Thickness);

V       = ((1+v23)*(1-v23-2*v12^2*E22/E11));
c11     = (1-v23^2)*E11/V;
c12     = v12*(1+v23)*E22/V;
c13     = c12;
c23     = (v23+v12^2*E22/E11)*E22/V;
c22     = (1-v12^2*E22/E11)*E22/V;
c33     = c22;
c44     = G23;
c55     = G12;
c66     = c55;

C0=[c11,c12,c13,0  ,0  ,0  ;
    c12,c22,c23,0  ,0  ,0  ;
    c13,c23,c33,0  ,0  ,0  ;
    0  ,0  ,0  ,c44,0  ,0  ;
    0  ,0  ,0  ,0  ,c55,0  ;
    0  ,0  ,0  ,0  ,0  ,c66];

a = 0;
b = 0;
c = 0;

for k=1:PlyNum

    theta = FiberAngle(k)*pi/180;
    vk    = Layer_Thickness(k)/Total_Thickness;

    m     = cos(theta);
    n     = sin(theta);

    T_s   = [m^2 ,n^2 ,0  ,0  ,0  ,2*m*n ;
             n^2 ,m^2 ,0  ,0  ,0  ,-2*m*n;
             0   ,0   ,1  ,0  ,0  ,0     ;
             0   ,0   ,0  ,m  ,-n ,0     ;
             0   ,0   ,0  ,n  ,m  ,0     ;
            -m*n ,m*n ,0  ,0  ,0  ,(m^2-n^2)];




    T_e   = [m^2 ,n^2 ,0  ,0  ,0  ,m*n   ;  % w.r.t. engineering strain
             n^2 ,m^2 ,0  ,0  ,0  ,-m*n  ;
             0   ,0   ,1  ,0  ,0  ,0     ;
             0   ,0   ,0  ,m  ,-n ,0     ;
             0   ,0   ,0  ,n  ,m  ,0     ;
            -2*m*n,2*m*n,0,0  ,0  ,(m^2-n^2)];
```

```
    C     = T_s\C0*T_e;

    delta_k = C(4,4)*C(5,5)-(C(4,5))^2;
    a = a+vk*C(4,4)/delta_k;
    b = b+vk*C(5,5)/delta_k;
    c = c+vk*C(4,5)/delta_k;

end

delta   = a*b-c^2;

% the following is for the calculation of Cij %

C_bar   = zeros(6,6);

for k=1:PlyNum

    theta   = FiberAngle(k)*pi/180;
    vk      = Layer_Thickness(k)/Total_Thickness;

    m       = cos(theta);
    n       = sin(theta);

    T_s   = [m^2 ,n^2 ,0  ,0  ,0  ,2*m*n ;
             n^2 ,m^2 ,0  ,0  ,0  ,-2*m*n;
             0   ,0   ,1  ,0  ,0  ,0     ;
             0   ,0   ,0  ,m  ,-n ,0     ;
             0   ,0   ,0  ,n  ,m  ,0     ;
             -m*n ,m*n ,0  ,0  ,0  ,(m^2-n^2)];

    T_e   = [m^2 ,n^2 ,0  ,0  ,0  ,m*n   ;
             n^2 ,m^2 ,0  ,0  ,0  ,-m*n  ;
             0   ,0   ,1  ,0  ,0  ,0     ;
             0   ,0   ,0  ,m  ,-n ,0     ;
             0   ,0   ,0  ,n  ,m  ,0     ;
             -2*m*n,2*m*n,0,0  ,0  ,(m^2-n^2)];

    C = T_s\C0*T_e;

    delta_k = C(4,4)*C(5,5)-(C(4,5))^2;

    C_bar(1,1)  = C_bar(1,1)+vk*C(1,1);
    C_bar(1,2)  = C_bar(1,2)+vk*C(1,2);
    C_bar(1,3)  = C_bar(1,3)+vk*C(1,3);
    C_bar(1,6)  = C_bar(1,6)+vk*C(1,6);

    C_bar(2,1)  = C_bar(1,2);
    C_bar(2,2)  = C_bar(2,2)+vk*C(2,2);
    C_bar(2,3)  = C_bar(2,3)+vk*C(2,3);
    C_bar(2,6)  = C_bar(2,6)+vk*C(2,6);

    C_bar(3,1)  = C_bar(1,3);
    C_bar(3,2)  = C_bar(2,3);
    C_bar(3,3)  = C_bar(3,3)+vk*C(3,3);
    C_bar(3,6)  = C_bar(3,6)+vk*C(3,6);

    C_bar(6,1)  = C_bar(1,6);
    C_bar(6,2)  = C_bar(2,6);
    C_bar(6,3)  = C_bar(3,6);
    C_bar(6,6)  = C_bar(6,6)+vk*C(6,6);
```

```
    C_bar(4,4)   = C_bar(4,4)+vk*C(4,4)/delta_k/delta;
    C_bar(4,5)   = C_bar(4,5)+vk*C(4,5)/delta_k/delta;
    C_bar(5,4)   = C_bar(4,5);
    C_bar(5,5)   = C_bar(5,5)+vk*C(5,5)/delta_k/delta;
end

S_bar   = inv(C_bar);       % compliance matrixn %

Ex  = 1/S_bar(1,1);
Ey  = 1/S_bar(2,2);
Ez  = 1/S_bar(3,3);
Vyz = -S_bar(2,3)/S_bar(2,2);
Vxz = -S_bar(3,1)/S_bar(1,1);
Vxy = -S_bar(2,1)/S_bar(1,1);

EE1 = Ez;
EE2 = Ey;
EE3 = Ex;

nu12 = Vyz*Ez/Ey;
nu13 = Vxz*Ez/Ex;
nu23 = Vxy*Ey/Ex;

a11 = 1/EE1;
a12 = -nu12/EE1;
a13 = -nu13/EE1;
a22 = 1/EE2;
a23 = -nu23/EE2;
a33 = 1/EE3;

C   = [a11 ,a12 ,a13 ;
       a12 ,a22 ,a23 ;
       a13 ,a23 ,a33];
end % end of subroutine "F2MCini"                                    %
```

```
% "FMC" are adapted and optimized from the work of Shan (2006)        %
function [a,b,c,d] = F2MC(lamaij,cellge)
arr    = lamaij(1,1);
art    = lamaij(1,2);
arx    = lamaij(1,3);
att    = lamaij(2,2);
atx    = lamaij(2,3);
axx    = lamaij(3,3);

betarr = arr-arx^2/axx;
betatt = att-atx^2/axx;
betart = art-arx*atx/axx;
k      = sqrt(betarr/betatt);
h      = (atx-arx)/(betarr-betatt);

a1     = cellge(2);
a2     = cellge(3);
l      = cellge(4);
C      = a1/a2;
Vo     = pi*a1^2*l;


%  a, b, c, and d are calculated in full dimension                    %
a = (-2*betart+2*k*betatt*(1+C^(2*k))/(1-C^(2*k)))*Vo;
b = (2*h/axx*betatt*((k+1)-2*k*C^(k-1)+C^(2*k)*(k-1))/(1-C^(2*k))...
        +2*atx/axx+1)*Vo;
c = 2*a1^2*pi/axx*((-arx-k*atx)/(k+1)*(C^(k-1)-C^(2*k))/(1-C^(2*k))+...
        (arx-k*atx)/(k-1)*(1-C^(k-1))/(1-C^(2*k))-axx/2);
d = 2*a1^2*pi/axx^2*(h*(arx+atx*k)/(k+1)*(C^k-1/C)^2/(1-C^(2*k))+...
        h*(arx-atx*k)/(k-1)*(1-C^(k-1))^2/(1-C^(2*k))+...
        (axx-h*(arx+atx))*(C^(-2)-1)/2);

end % end of subroutine F2MC                                          %
```

```
% "FMCdam" are adapted and optimized from the work of Shan (2006)     %
function [etae,etap] = FMCdam(plyEij,cellge,lamaij,etaij)
E11    = plyEij(1);
E22    = plyEij(2);
G12    = plyEij(4);
v12    = plyEij(5);
fang   = cellge(1);

eta11  = etaij(1);
eta12  = etaij(2);
eta22  = etaij(3);
eta33  = etaij(4);

m      = cos(fang/180*pi);
n      = sin(fang/180*pi);

v21    = E22*v12/E11;
Q11    = E11/(1-v12*v21);
Q12    = v21*E11/(1-v12*v21);
Q22    = E22/(1-v12*v21);
Q66    = G12;

Q11bar = Q11*m^4+2*(Q12+2*Q66)*n^2*m^2+Q22*n^4;
Q12bar = (Q11+Q22-4*Q66)*n^2*m^2+Q12*(n^4+m^4);
Q22bar = Q11*n^4+2*(Q12+2*Q66)*n^2*m^2+Q22*m^4;
Q16bar = (Q11-Q12-2*Q66)*m^3*n-(Q22-Q12-2*Q66)*m*n^3;
Q26bar = (Q11-Q12-2*Q66)*m*n^3-(Q22-Q12-2*Q66)*m^3*n;
Q66bar = (Q11+Q22-2*Q12-2*Q66)*n^2*m^2+Q66*(n^4+m^4);

Qbar   = [ Q11bar Q12bar Q16bar;
           Q12bar Q22bar Q26bar;
           Q16bar Q26bar Q66bar];

arr    = lamaij(1,1);
art    = lamaij(1,2);
arx    = lamaij(1,3);
att    = lamaij(2,2);
atx    = lamaij(2,3);
axx    = lamaij(3,3);
betarr = arr-arx^2/axx;
betatt = att-atx^2/axx;
k      = sqrt(betarr/betatt);
h      = (atx-arx)/(betarr-betatt);

a1     = cellge(2);
a2     = cellge(3);
C      = a1/a2;

Qs     = [ m^2  n^2    2*m*n;
           n^2  m^2   -2*m*n;
          -m*n  m*n  m^2-n^2];

Qe     = [    m^2    n^2  0;
              n^2    m^2  0;
            -2*m*n  2*m*n  0];

no     = 100;
t      = (1-C)/no;
r      = (C+t/2):t:(1-t/2);

A1     = C^(k+1)/(1-C^(2*k))*r.^(k-1);
A2     = C^(k+1)/(1-C^(2*k))*r.^(-k-1);
```

```
A3      = (1-C^(k+1))/(1-C^(2*k))*r.^(k-1);
A4      = (1-C^(k-1))/(1-C^(2*k))*C^(k+1)*r.^(-k-1);
Pr      = A1-A2;
Qr      = (1-A3-A4)*h/axx;
Rt      = (-arx*atx+art*axx-atx^2*k+att*axx*k)/axx*A1+...
          (arx*atx-art*axx-atx^2*k+att*axx*k)/axx*A2;
Rr      = -(arx^2+arx*atx*k-axx*(arr+art*k))/axx*A1+...
          (arx^2-arr*axx-arx*atx*k+art*axx*k)/axx*A2;
Sr      = h*(arx^2+arx*atx*k-axx*(arr+art*k))/axx^2*A3+...
          h*(arx^2-arr*axx-arx*atx*k+art*axx*k)/axx^2*A4+...
          (-arx^2*h+(arr+art)*axx*h+arx*(axx-atx*h))/axx^2;
St      = h*(arx*atx-art*axx+(atx^2-att*axx)*k)/axx^2*A3+...
          h*(arx*atx-art*axx-atx*atx*k+att*axx*k)/axx^2*A4+...
          (-atx^2*h+(art+att)*axx*h+atx*(axx-arx*h))/axx^2;

Pr      = reshape(Pr,[1,1,no]);
Qr      = reshape(Qr,[1,1,no]);
Rr      = reshape(Rr,[1,1,no]);
Rt      = reshape(Rt,[1,1,no]);
Sr      = reshape(Sr,[1,1,no]);
St      = reshape(St,[1,1,no]);
Sx      = ones([1,1,no]);
S1      = [Sx;St;zeros(1,1,no);Sr];
S2      = [Sx;St;zeros(1,1,no);Qr];
S3      = [zeros(1,1,no);Rt;zeros(1,1,no);Rr];
S4      = [zeros(1,1,no);Rt;zeros(1,1,no);Pr];
QE      = [Qe zeros(3,1); zeros(1,3) 1];
QS      = [Qs*Qbar zeros(3,1); zeros(1,3) 1];
Ue      = zeros(4,1,no);
dUe     = zeros(4,1,no);
Up      = zeros(4,1,no);
dUp     = zeros(4,1,no);

Eta     = [eta11     0     0     0;
                0 eta22     0     0;
                0     0 eta12     0;
                0     0     0 eta33];

for i = 1:length(r)
       Ue(:,:,i) = pi*abs((QE*S1(:,:,i)).*(QS*S2(:,:,i)))*r(i)*t;
      dUe(:,:,i) = Eta*Ue(:,:,i);
Up(:,:,i) = pi*abs((QE*S3(:,:,i)).*(QS*S4(:,:,i)))*r(i)*t;
      dUp(:,:,i) = Eta*Up(:,:,i);
end
etae = sum(sum(dUe))/sum(sum(Ue));
etap = sum(sum(dUp))/sum(sum(Up));

end % end of subroutine "FMCdam"                                          %

function [pzres] = ind2res(X,A,B,D,Msys,tau,g,pztar)
% ========================================================================= %
% This is a subroutine that calculates the error towards target           %
% spectral data set based on equation (5.21)                              %
% ========================================================================= %
n       = size(X,2)/3;
Y       = zeros(size(X));

for ii = 1:n
% translating the grid idex to actual values                              %
    id      = (ii-1)*3+1;
    Y(:,id)   = A(sub2ind(size(A),X(:,id),X(:,id+1),X(:,id+2)));
    Y(:,id+1) = B(sub2ind(size(B),X(:,id),X(:,id+1),X(:,id+2)));
    Y(:,id+2) = D(sub2ind(size(D),X(:,id),X(:,id+1),X(:,id+2)));
```

```
end

% calculating the stiffness matrix                                        %
K      = Cell2K(Y,g);

% constructing the Jacobi matrix array                                    %
sizK   = size(K);
J1     = reshape((Msys^-.5)*K(:,:),[n sizK(2:end)]);
dJ     = ndims(J1);
Jt     = reshape(permute(J1, [1 3:dJ 2]),[prod(sizK)/sizK(2) sizK(2)]);
J      = Jt*(Msys^-.5);
J      = permute(reshape(J, [sizK([1 3:dJ]) n]), [1 dJ 2:dJ-1]);

% calculating the residue pole and zeros error                            %
pz     = zeros(2*n-1,length(X(:,1)));

for ii = 1:length(X(:,1))

    po     = sort((eig(J(:,:,ii))).^.5/2/pi/tau);
    ze     = sort(eig(J(2:end,2:end,ii)).^.5/2/pi/tau);
    pz(:,ii) = [po;ze]-pztar;

end

pzres  = sqrt(dot(pz,pz,1))';

end % end of the subfunction "ind2res"                                   %
```

```
function [K,J] = Cell2K(X,g)
% ================================================================== %
% This vectored subroutine calculates the stiffness matrix of k      %
% cellular string structures, concurrently. Each string has n cells. %
% Input X is a 3n by k matrix                                        %
% Output K is a n by n by k matrix                                   %
% ================================================================== %

n      = size(X,2)/3;           % number of cells in each string      %
k      = size(X,1);             % number of cell strings              %

K      = zeros(n,n,k);
J      = zeros(n*(n+1)/2,3*n);

for zz = 1:k

    % extract and re-structure the input data matrix                  %
    a      = X(zz,1:3:end)';
    b      = X(zz,2:3:end)';
    d      = X(zz,3:3:end)';
    % construct the matrix relating pressure and strain               %
    W      = sum(-a./b);
    p2e    = (repmat((-a./b.*d-b)',[n,1])-diag(d)*W)...
             .*(repmat(-1./b,[1,n])/W/g);
    % construct the matrix relating flow port flow to strain          %
    A      = repmat(g*a',[n-1,1]);
    B      = repmat(b',[n-1,1]);
    ind    = find((repmat(1:n,[n-1,1])-repmat((1:n-1)',[1,n]))<=0);
    A(ind) = 0;
    B(ind) = 0;
    v2e    = A*p2e+B;
    % construct the system K matrix                                   %
    Q      = [ones(1,n); v2e];
    Ki     = [-b(n)*p2e(n,:);
              p2e(2:n,:)-p2e(1:n-1,:)];
    Ki(1,n) = Ki(1,n)+d(n)/g;
    % assign to the stiffness matrix corresponding to kth string      %
    K(:,:,zz) = Ki/Q;
end

end % end of subroutine of "Cell2K"                                   %
```

```
function y = Eig2Cell(X,ldt,mut,g,Msys,tau)
% ========================================================================= %
% This subroutine defines the object function to calculate the final  %
% design candidate                                                          %
% ========================================================================= %
K      = Cell2K(X,g);

Vi     = (Msys^-.5)*K*(Msys^-.5);
Vi     = (Vi+Vi')/2;                    % conditioning the Vi         %
ldi    = sort(eig(Vi));
mui    = sort(eig(Vi(2:end,2:end)));

y      = [ldi-ldt;mui-mut]/2/pi/tau;

end % end of subroutine of "Eig2Cell"                                     %
```

```
function [SOL] = chkOmega(u,v,w,a,b,d,N,scl,n)
% ================================================================== %
% This subroutine checks if u,v,w is in Omega                        %
% ================================================================== %
chk    = zeros(n,1);

% the omega space is split into three subspace, and the a-b-d        %
% values for the three F2MC cells are checked against the boundaries %
% of these three subspaces                                           %
for zz = 1:3

    if zz == 1
        idz = 1:50;
    elseif zz==2
        idz = 50:99;
    else
        idz = 99:148;
    end

    % the boundary surfaces and their normal for parametric subspace %
    [A,B,D,NA,NB,ND] = ...
        bdsur(a(idz,:,:),b(idz,:,:),scl(zz)*log10(d(idz,:,:)),N);

    % check if u,v,w are in the subspaces of omega                   %
    chk(zz) = inOmega(u,v,scl(zz)*log10(w),A,B,D,NA,NB,ND);

end
SOL = sum(chk);

end % end of subroutine of "chkOmega"                                %
```

```
function [A,B,D,NA,NB,ND] = bdsur(a,b,d,N)
% ================================================================== %
% This is a subroutine to extract the boundary surface of Omega space %
% ================================================================== %

[U,V]   = meshgrid(1:N,1:N);
W       = N*ones(N,N);
I       = ones(N,N,6);
J       = ones(N,N,6);
K       = ones(N,N,6);

% subindex corresponding to the six boundary surface %
J(:,:,1) = U;
K(:,:,1) = V;

I(:,:,2) = W;
J(:,:,2) = U;
K(:,:,2) = V;

I(:,:,3) = U;
K(:,:,3) = V;

I(:,:,4) = U;
J(:,:,4) = W;
K(:,:,4) = V;

I(:,:,5) = U;
J(:,:,5) = V;

I(:,:,6) = U;
J(:,:,6) = V;
K(:,:,6) = W;

% constructing the boundary surface %
A       = ones(N,N,6);
B       = ones(N,N,6);
D       = ones(N,N,6);

for x = 1:N
    for y = 1:N
        for z = 1:6
            A(x,y,z) = a(I(x,y,z),J(x,y,z),K(x,y,z));
            B(x,y,z) = b(I(x,y,z),J(x,y,z),K(x,y,z));
            D(x,y,z) = d(I(x,y,z),J(x,y,z),K(x,y,z));
        end
    end
end

% ========== Construct the normal vector of bd surface ============ %
NA      = zeros(size(A));
NB      = zeros(size(B));
ND      = zeros(size(D));




% "path" like construction for surface norm vector %
for I = 1:10
    xspan = (5*(I-1)+1):(5*I);
    for J = 1:10
        yspan = (5*(J-1)+1):(5*J);
        for z = 1:6
```

```
            if z==1 || z==4 || z==5
% reverse the surfnorm to make sure it points inward to the space %

[NA(xspan,yspan,z),NB(xspan,yspan,z),ND(xspan,yspan,z)]...
                    = surfnorm(A(xspan,yspan,z),B(xspan,yspan,z),...
                    D(xspan,yspan,z));
                NA(xspan,yspan,z)=-NA(xspan,yspan,z);
                NB(xspan,yspan,z)=-NB(xspan,yspan,z);
                ND(xspan,yspan,z)=-ND(xspan,yspan,z);
            else

[NA(xspan,yspan,z),NB(xspan,yspan,z),ND(xspan,yspan,z)]...
                    = surfnorm(A(xspan,yspan,z),B(xspan,yspan,z),...
                    D(xspan,yspan,z));
            end
        end
    end
end

end % end of subfunction "bdsur"                                        %
```

```
function [Sol,p] = inOmega(u,v,w,A,B,D,NA,NB,ND)
%  ================================================================  %
%  This subroutine check whether the cell #2 design point [u,v,w] is  %
%  in the subspace of Omega (chapter 4)                               %
%  ================================================================  %
Libmin  = zeros(6,3);

for z = 1:6
    dist   = sqrt((A(:,:,z)-u).^2+(B(:,:,z)-v).^2+(D(:,:,z)-w).^2);
    [minx, Idx] = min(dist);
    [mdist,idy] = min(minx);
    idx    = Idx(idy);
    Libmin(z,:) = [idx idy round(mdist)];
end

Mdist  = min(Libmin(:,3));
surid  = find(Libmin(:,3) == Mdist);

chk    = zeros(size(surid));

for s = 1:length(surid)
    p      = [A(Libmin(surid(s),1),Libmin(surid(s),2),surid(s))...
              B(Libmin(surid(s),1),Libmin(surid(s),2),surid(s))...
              D(Libmin(surid(s),1),Libmin(surid(s),2),surid(s))];

    dvec   = [u-p(1) v-p(2) w-p(3)];


    nvec   = [NA(Libmin(surid(s),1),Libmin(surid(s),2),surid(s))...
              NB(Libmin(surid(s),1),Libmin(surid(s),2),surid(s))...
              ND(Libmin(surid(s),1),Libmin(surid(s),2),surid(s))];

    if norm(dvec) > 0.01
        dvec   = dvec/norm(dvec);
        chk(s) = dot(dvec,nvec);
    else
        chk(s) = -1;
    end
    if chk(s) < 0.01
        chk(s) = -1;
    end
end

Sol = sum(chk>0)==length(chk);

end % end of the subroutine "inOmega"                                 %
```

Appendix F
Closed Form Relationships between the Constitutive Parameters of the Two F^{2}MC Cells in Four Unique Architectures

For AC type of architecture

$$\begin{cases} \alpha_2 = \left[\beta_1^2 + \alpha_1\left(\delta_1 - g\mathbf{K}_{11}\right)\right]/\Delta \\ \beta_2 = g\left[-\mathbf{K}_{11}\beta_1 + \mathbf{K}_{12}\left(\alpha_1\delta_1 + \beta_1^2\right)\right]/\Delta \\ \delta_2 = g\left\{-g\mathbf{K}_{12}^2\left(\alpha_1\delta_1 + \beta_1^2\right) + \mathbf{K}_{11}\left[-\delta_1 + gK_{22}\left(\alpha_1\delta_1 + \beta_1^2\right)\right]\right\}/\Delta \\ \Delta = -\delta_1 + g\left[g\mathbf{K}_{12}^2\alpha_1 + S_1\left(1 - gK_{22}\alpha_1\right) - 2\mathbf{K}_{12}\beta_1 + \mathbf{K}_{22}\left(\alpha_1\delta_1 + \beta_1^2\right)\right] \end{cases} \quad \text{(F1)}$$

For AD type of architecture

$$\begin{cases} \alpha_2 = \alpha_1/\Delta \\ \beta_2 = \left(g\mathbf{K}_{12}\alpha_1 - \beta_1\right)/\Delta \\ \delta_2 = g\mathbf{K}_{11} - \delta_1 - g\left(g\mathbf{K}_{12}^2\alpha_1 - 2\mathbf{K}_{12}\beta_1 + \mathbf{K}_{22}\beta_1^2\right)/\Delta \\ \Delta = g\mathbf{K}_{22}\alpha_1 - 1 \end{cases} \quad \text{(F2)}$$

For BC type of architecture

$$\begin{cases} \alpha_2 = \left(\delta_1 - g\mathbf{K}_{11}\right)/\left(g\Delta\right) \\ \beta_2 = -\mathbf{K}_{12}\delta_1/\Delta \\ \delta_2 = g\left(\mathbf{K}_{11}\mathbf{K}_{22} - \mathbf{K}_{12}^2\right)\delta_1/\Delta \\ \Delta = g\left(\mathbf{K}_{12}^2 - \mathbf{K}_{11}\mathbf{K}_{22}\right) + \delta_1\mathbf{K}_{22} \end{cases} \tag{F3}$$

For BD type of architecture

$$\begin{cases} \alpha_2 = \left(g\mathbf{K}_{22}\right)^{-1} \\ \beta_2 = \mathbf{K}_{12}/\mathbf{K}_{22} \\ \delta_2 = \left(g\mathbf{K}_{11}\mathbf{K}_{22} - g\mathbf{K}_{12}^2 - \mathbf{K}_{22}\delta_1\right)/\mathbf{K}_{22} \end{cases} \tag{F4}$$

Appendix G
MATLAB Script of the Comprehensive Synthesis Procedure

```
% ================================================================== %
% This is the master synthesis routine for dual F2MC cellular        %
% structure, all four types of architectures will be considered for  %
% the same target                                                    %
% ================================================================== %

% ================================================================== %
% Some of the required subroutines: “paraspace” “cellpa” “FMCini”    %
% “F2MC” “FMCdam” “bdsur” and “inOmega” can be found in appendix E   %
% ================================================================== %

function [SOL] = DualCellSyn()
% reset the system                                                   %
clc;
clear all;
close all;

%% ==================== Initialize the problem ====================== %
ri     = 0.01;                  % F2MC cell inner radius (m)         %
g      = 20;                    % cell length to radius ratio        %
l      = ri*g;                  % cell length (m)                    %
rho    = 1000;                  % working fluid density (kg/m^3)     %
lf     = 0.30;                  % flow port length (m)               %
rf     = 0.003;                 % flow port radius (m)               %
E2     = 15e6;                  % fiber ply transverse modulus (Pa)  %
Bk     = 40e6;                  % fluid bulk modulus (Pa)            %
m      = 1.5;                   % end mass (kg)                      %

M      = m/rho/ri^3;            % normalized external inertia        %
I      = pi*lf*ri/rf^2;         % normalized flow port inertia       %
tau    = ri*sqrt(rho/pi/E2);    % time unit (s)                      %

%% =========== Assigning pole and zero target I and II ============== %
Wp1    = 25;                    % first pole position (Hz)           %
Wzf    = 35;                    % fe zero position (Hz)              %
Wp2    = 50;                    % second pole position (Hz)          %

wpz    = [Wp1 Wp2 Wzf]*2*pi*tau;% normalized pole and zero frequency %
wpp    = (Wp2+5)*2*pi*tau;      % normalized pressure zero requirement%

%% ================== Construct the Omega space ===================== %
N      = 50;                    % size of each parametric sub-space  %
id1    = 1:N;
id2    = N+1:2*N;
```

```
id3    = 2*N+1:3*N;
[ang,era,wth] = designvar(N);   % the physical variables              %
% max(E1/E2) = 6000; min(E1/E2) =  50;                                 %
% max(c1/c2) = 0.95; min(c1/c2) = 0.6;                                 %

% pre-locate the 150x50x50 grid that will span the Omega space        %
a       = zeros(3*N,N,N);   % alpha value of the 3D grid              %
b       = zeros(3*N,N,N);   % beta value of the 3D grid               %
d       = zeros(3*N,N,N);   % delta value of the 3D grid              %

% Calculate the Omega space based on "ang" "era" and "wth" values     %
[a(id1,:,:),b(id1,:,:),d(id1,:,:)] = ...
    paraspace(ri,l,Bk,E2,ang(1,:),era(1,:),wth(1,:));
[a(id2,:,:),b(id2,:,:),d(id2,:,:)] = ...
    paraspace(ri,l,Bk,E2,ang(2,:),era(2,:),wth(2,:));
[a(id3,:,:),b(id3,:,:),d(id3,:,:)] = ...
    paraspace(ri,l,Bk,E2,ang(3,:),era(3,:),wth(3,:));
% "a" "b" and "d" are used to calculate the boundary surfaces of Omega
% "ai" "bi" and "di" are the candidate designs for cell #1            %
[ai,bi,di] = ...
    paraspace(ri,l,Bk,E2,ang(4,:),era(4,:),wth(4,:));

% Note: the data of a, b, d, ai, bi, di can be saved for future       %
% synthesis, so that they don't need to be calculated every time.     %
save('a.mat','a');
save('b.mat','b');
save('d.mat','d');
save('ai.mat','ai');
save('bi.mat','bi');
save('di.mat','di');

%% ============= Adjust the bulk modulus on alpha  ================== %
Cf     = E2/Bk;                 % normalized fluid bulk compliance    %
a      = a  + Cf;
ai     = ai + Cf;

%% ========== Survey the design space for Target I ================== %
% calculate the a-b-d values for cell #2 (Appendix E)                 %
[afAC,bfAC,dfAC] = pair(ai,bi,di,wpz,M,I,g,'AC'); % AC architecture   %
[afAD,bfAD,dfAD] = pair(ai,bi,di,wpz,M,I,g,'AD'); % AD architecture   %
[afBC,bfBC,dfBC] = pair(ai,bi,di,wpz,M,I,g,'BC'); % BC architecture   %
[afBD,bfBD,dfBD] = pair(ai,bi,di,wpz,M,I,g,'BD'); % BD architecture   %

scl    = [10 10 1];             % scale factor for delta values       %
az     = 330;                   % azimuth viewing angle of 3D plot    %
el     = 5;                     % elevation viewing angle of 3D plot  %

% check if the a-b-d values for cell #2 are in omega                  %
IDAC   = check(afAC,bfAC,dfAC,a,b,d,N,scl);
IDAD   = check(afAD,bfAD,dfAD,a,b,d,N,scl);
IDBC   = check(afBC,bfBC,dfBC,a,b,d,N,scl);
IDBD   = check(afBD,bfBD,dfBD,a,b,d,N,scl);
% "ID~~" means the index position of the solution in the 3D grid      %

%% ============= Find designs that satisfy target II ================ %
if ~isempty(IDBC)
    IDBC   = IDPP(bi,di,afBC,bfBC,dfBC,wpp,IDBC,'BC',g,I);
```

```
end

if ~isempty(IDBD)
    IDBD   = IDPP(bi,di,afBD,bfBD,dfBD,wpp,IDBD,'BD',g,I);
end

%% ======== Calculate the performance of target III and IV ========== %
% Translate the constitutive parameters back into the physical design %
[angAC,eraAC,wthAC] = ind2sub(size(ai),IDAC);
[angAD,eraAD,wthAD] = ind2sub(size(ai),IDAD);
[angBC,eraBC,wthBC] = ind2sub(size(ai),IDBC);
[angBD,eraBD,wthBD] = ind2sub(size(ai),IDBD);

angi = ang(4,:);
wthi = wth(4,:);
erai = era(4,:);

% calculate the variable stiffness of the feasible designs            %
[KRAC,rgbKRAC] = KR(ai,bi,di,afAC,bfAC,dfAC,IDAC,g,'AC');
[KRAD,rgbKRAD] = KR(ai,bi,di,afAD,bfAD,dfAD,IDAD,g,'AD');
[KRBC,rgbKRBC] = KR(ai,bi,di,afBC,bfBC,dfBC,IDBC,g,'BC');
[KRBD,rgbKRBD] = KR(ai,bi,di,afBD,bfBD,dfBD,IDBD,g,'BD');

% calculate the static actuation ratio of the feasible designs        %
[SDAC,rgbSDAC] = SD(bi,di,bfAC,dfAC,IDAC,g,'AC');
[SDAD,rgbSDAD] = SD(bi,di,bfAD,dfAD,IDAD,g,'AD');
[SDBC,rgbSDBC] = SD(bi,di,bfBC,dfBC,IDBC,g,'BC');
[SDBD,rgbSDBD] = SD(bi,di,bfBD,dfBD,IDBD,g,'BD');

%% ================== Plotting the results ======================== %
% the boundary surfaces of the whole parametric design space          %
[Ai,Bi,Di,~,~,~] = bdsur(ai,bi,di,N);

figure(1)
% figure (1) plot the designs of F2MC cells that satisfy target I and
II, in terms of the constitutive parameters                           %
subplot(2,2,1)
hold on;
for z = 1:6
    h      = mesh(Ai(:,:,z),Bi(:,:,z),10*log10(Di(:,:,z)));
    set(h,'facecolor',[1 1 1],'facealpha',0.8,'edgecolor',[0.8 0.8
0.8])
    view([az el]);
end
% the constitutive parameters of cell # 1 is plotted as red dots      %
plot3(ai(IDAC),bi(IDAC),10*log10(di(IDAC)),'r.');
% the constitutive parameters of cell # 1 is plotted as green dots    %
plot3(afAC(IDAC),bfAC(IDAC),10*log10(dfAC(IDAC)),'g.');
title('AC architecture')
xlabel('\alpha')
ylabel('\beta')
zlabel('10log_{10}(\delta)')
grid on;
hold off;

subplot(2,2,2)
hold on;
```

```
for z = 1:6
    h      = mesh(Ai(:,:,z),Bi(:,:,z),10*log10(Di(:,:,z)));
    set(h,'facecolor',[1 1 1],'facealpha',0.8,'edgecolor',[0.8 0.8
0.8])
    view([az el]);
end
plot3(ai(IDAD),bi(IDAD),10*log10(di(IDAD)),'r.');
plot3(afAD(IDAD),bfAD(IDAD),10*log10(dfAD(IDAD)),'g.');
title('AD architecture')
xlabel('\alpha')
ylabel('\beta')
zlabel('10log_{10}(\delta)')
grid on;
hold off;

subplot(2,2,3)
hold on;
for z = 1:6
    h      = mesh(Ai(:,:,z),Bi(:,:,z),10*log10(Di(:,:,z)));
    set(h,'facecolor',[1 1 1],'facealpha',0.8,'edgecolor',[0.8 0.8
0.8])
    view([az el]);
end
plot3(ai(IDBC),bi(IDBC),10*log10(di(IDBC)),'r.');
plot3(afBC(IDBC),bfBC(IDBC),10*log10(dfBC(IDBC)),'g.');
title('BC architecture')
xlabel('\alpha')
ylabel('\beta')
zlabel('10log_{10}(\delta)')
grid on;
hold off;


subplot(2,2,4)
hold on;
for z = 1:6
    h      = mesh(Ai(:,:,z),Bi(:,:,z),10*log10(Di(:,:,z)));
    set(h,'facecolor',[1 1 1],'facealpha',0.8,'edgecolor',[0.8 0.8
0.8])
    view([az el]);
end
plot3(ai(IDBD),bi(IDBD),10*log10(di(IDBD)),'r.');
plot3(afBD(IDBD),bfBD(IDBD),10*log10(dfBD(IDBD)),'g.');
title('BD architecture')
xlabel('\alpha')
ylabel('\beta')
zlabel('10log_{10}(\delta)')
grid on;
hold off;

%%
figure(2)
% figure (2) plot the F2MC cell #1 design in terms of its physical    %
% design variables, and color code is the variable stiffness ratio.   %
% This is the basis of figure 6.10                                    %
subplot(2,2,1)
scatter3(angi(angAC),erai(eraAC),wthi(wthAC),5,rgbKRAC/256,'fill');
```

```
grid on;
view([az el]);
xlabel('fiber orientation (^o)');
ylabel('E_1/E_2 ratio')
zlabel('a_i/a_o ratio')
colorbar('YTickLabel',...
    {round((min(KRAC):(max(KRAC)-min(KRAC))/10:max(KRAC))*10)/10})
ylim([50 6000])
view([az el]);
title('AC architecture')
grid on


subplot(2,2,2)
scatter3(angi(angAD),erai(eraAD),wthi(wthAD),5,rgbKRAD/256,'fill');
grid on;
view([az el]);
xlabel('fiber orientation (^o)');
ylabel('E_1/E_2 ratio')
zlabel('a_i/a_o ratio')
colorbar('YTickLabel',...
    {round((min(KRAD):(max(KRAD)-min(KRAD))/10:max(KRAD))*10)/10})
ylim([50 6000])
view([az el]);
title('AD architecture')
grid on

subplot(2,2,3)
scatter3(angi(angBC),erai(eraBC),wthi(wthBC),5,rgbKRBC/256,'fill');
grid on;
view([az el]);
xlabel('fiber orientation (^o)');
ylabel('E_1/E_2 ratio')
zlabel('a_i/a_o ratio')
colorbar('YTickLabel',...
    {round((min(KRBC):(max(KRBC)-min(KRBC))/10:max(KRBC))*100)/100})
ylim([50 6000])
view([az el]);
title('BC architecture')
grid on

subplot(2,2,4)
scatter3(angi(angBD),erai(eraBD),wthi(wthBD),5,rgbKRBD/256,'fill');
grid on;
view([az el]);
xlabel('fiber orientation (^o)');
ylabel('E_1/E_2 ratio')
zlabel('a_i/a_o ratio')
colorbar('YTickLabel',...
    {round((min(KRBD):(max(KRBD)-min(KRBD))/10:max(KRBD))*10)/10})
ylim([50 6000])
view([az el]);
title('BD architecture')
grid on

%%
figure(3)
```

```
% figure (3) plot the F2MC cell #1 design in terms of its physical    %
% design variables, and color code is the static actuation authority. %
% This is the basis of figure 6.10                                     %
subplot(2,2,1)
scatter3(angi(angAC),erai(eraAC),wthi(wthAC),5,rgbSDAC/256,'fill');
grid on;
view([az el]);
xlabel('fiber orientation (^o)');
ylabel('E_1/E_2 ratio')
zlabel('a_i/a_o ratio')
colorbar('YTickLabel',...
    {round((min(SDAC):(max(SDAC)-min(SDAC))/10:max(SDAC))*10)/10})
ylim([50 6000])
view([az el]);
title('AC architecture')
grid on

subplot(2,2,2)
scatter3(angi(angAD),erai(eraAD),wthi(wthAD),5,rgbSDAD/256,'fill');
grid on;
view([az el]);
xlabel('fiber orientation (^o)');
ylabel('E_1/E_2 ratio')
zlabel('a_i/a_o ratio')
colorbar('YTickLabel',...
    {round((min(SDAD):(max(SDAD)-min(SDAD))/10:max(SDAD))*10)/10})
ylim([50 6000])
view([az el]);
title('AD architecture')
grid on

subplot(2,2,3)
scatter3(angi(angBC),erai(eraBC),wthi(wthBC),5,rgbSDBC/256,'fill');
grid on;
view([az el]);
xlabel('fiber orientation (^o)');
ylabel('E_1/E_2 ratio')
zlabel('a_i/a_o ratio')
colorbar('YTickLabel',...
    {round((min(SDBC):(max(SDBC)-min(SDBC))/10:max(SDBC))*10)/10})
ylim([50 6000])
view([az el]);
title('BC architecture')
grid on

subplot(2,2,4)
scatter3(angi(angBD),erai(eraBD),wthi(wthBD),5,rgbSDBD/256,'fill');
grid on;
view([az el]);
xlabel('fiber orientation (^o)');
ylabel('E_1/E_2 ratio')
zlabel('a_i/a_o ratio')
colorbar('YTickLabel',...
    {round((min(SDBD):(max(SDBD)-min(SDBD))/10:max(SDBD))*10)/10})
ylim([50 6000])
view([az el]);
title('BD architecture')
```

```
grid on

%%
figure(4)
% figure (4) plot the F2MC design in terms of variable stiffness      %
% verses static actuation authority.                                  %
% This is the basis of figure 6.11                                    %
subplot(2,2,1)
plot(KRAC,SDAC,'.');
xlabel('variable stiffness ratio')
ylabel('normalized static free stroke')
title('AC architecture')
grid on

subplot(2,2,2)
plot(KRAD,SDAD,'.');
xlabel('variable stiffness ratio')
ylabel('normalized static free stroke')
title('AD architecture')
grid on

subplot(2,2,3)
plot(KRBC,SDBC,'.');
xlabel('variable stiffness ratio')
ylabel('normalized static free stroke')
title('BC architecture')
grid on

subplot(2,2,4)
plot(KRBD,SDBD,'.');
xlabel('variable stiffness ratio')
ylabel('normalized static free stroke')
title('BD architecture')
grid on

end % end of the Main function                                        %
```

```
function [ang,era,wth] = designvar(N)
% ================================================================== %
% This is the subroutine to construct the F2MC physical variables    %
% ================================================================== %
erai   = 50;
eraf   = 6000;
wthi   = 0.6;
wthf   = 0.95;

% set up the physical variables                                      %
Q      = (1:N)'-1;
q_ang1 = (30/1)^(1/(N-1));      % ratio of geometric series (angle)  %
ang1   = 1*ones(N,1).*(q_ang1.^(Q));% array of fiber angle           %
q_ang2 = (50/30)^(1/(N-1));     % ratio of geometric series (angle)  %
ang2   = 30*ones(N,1).*(q_ang2.^(Q));% array of fiber angle          %
q_ang3 = (89/50)^(1/(N-1));     % ratio of geometric series (angle)  %
ang3   = 50*ones(N,1).*(q_ang3.^(Q));% array of fiber angle          %

ang4   = (1:(89-1)/49:89)';
ang = [ang1';ang2';ang3';ang4'];

q_era  = (eraf/erai)^(1/(N-1));  % ratio of geometric series (E1/E2) %
era    = erai*ones(N,1).*(q_era.^(Q));% array of E1/E2 ratio         %

era    = [era';era';era';era'];

wth    = (wthi:(wthf-wthi)/(N-1):wthf);% array of wall thickness ratio%
wth    = [wth;wth;wth;wth];

end % end of subroutine "desinvar"
```

```
function [af,bf,df] = pair(ai,bi,di,wpz,M,I,g,style)
% ================================================================== %
% This is the subroutine to calculate 2nd cell design               %
% ================================================================== %
ai     = reshape(ai,[],1);
bi     = reshape(bi,[],1);
di     = reshape(di,[],1);
n      = numel(di);

wp1    = wpz(1);
wp2    = wpz(2);
wz     = wpz(3);

% required stiffness matrix element (mormalized value)             %
S3     = wz^2*I;
S1     = M*(wp1^2+wp2^2-wz^2);
S2     = -sqrt((I*M)*(wp2^2-wz^2)*(wz^2-wp1^2));

% calculate the corresponding #2 cell design                        %
switch style
    case 'AC'
        den    = -g*S1-g^2*S2^2*ai+g^2*S1*S3*ai+2*g*S2*bi...
                 -g*S3*bi.^2+di-g*S3*ai.*di;
        af     = (g*S1*ai-bi.^2-ai.*di)./den;
        bf     = (-g*S1*bi+g*S2*bi.^2+g*S2*ai.*di)./den;
        df     = -g*(-g*S2^2*bi.^2+g*S1*S3*bi.^2-S1*di...
                 -g*S2^2*ai.*di+g*S1*S3*ai.*di)./den;
    case 'AD'
        den    = -1+g*S3*ai;
        af     = ai./den;
        bf     = (g*S2*ai-bi)./den;
        df     = (-g*S1-g^2*S2^2*ai+g^2*S1*S3*ai+2*g*S2*bi...
                 -g*S3*bi.^2+di-g*S3*ai.*di)./den;
    case 'BC'
        den    = g*S2^2-g*S1*S3+S3*di;
        af     = -(g*S1-di)./den/g;
        bf     = -S2*di./den;
        df     = -g*(S2^2-S1*S3)*di./den;
    case 'BD'
        af    = ones(n,1)*1/g/S3;
        bf    = ones(n,1)*S2/S3;
        df    = -(g*S2^2+di*S3-g*S1*S3)/S3;
end


end % end of subroutine "pair"                                     %
```

```
function ID = check(af,bf,df,a,b,d,N,scl)
%  ================================================================  %
%  This subroutine check if the candidate constitutive parameters     %
%  for cell #2: af, bf and df are in Omega space                      %
%  ================================================================  %

ID     = 0;
% the omega space is split into three subspace, and the a-b-d value   %
% for cell #2 is checked against the boundaries of the three subspace %
for zz = 1:3

    idz = (zz-1)*N+1:zz*N;
    % the boundary surfaces and their normal for parametric subspace  %
    [A,B,D,NA,NB,ND] = ...
        bdsur(a(idz,:,:),b(idz,:,:),scl(zz)*log10(d(idz,:,:)),N);

    % find the upper bound of the a, b, and d in the parametric sub-  %
    % space                                                           %
    a_ub   = max(max(max(a(idz,:,:))));
    b_ub   = max(max(max(b(idz,:,:))));
    d_ub   = max(max(max(d(idz,:,:))));

    % find the lower bound of the a, b, and d in the parametric sub-  %
    % space                                                           %
    a_lb   = min(min(min(a(idz,:,:))));
    b_lb   = min(min(min(b(idz,:,:))));
    d_lb   = min(min(min(d(idz,:,:))));

    % selecting a-b-d pair with its value locating within this range  %
    ida    = find(and(af>a_lb,af<a_ub));
    idb    = find(and(bf>b_lb,bf<b_ub));
    idd    = find(and(df>d_lb,df<d_ub));
    id     = intersect(ida,intersect(idb,idd));

    sol    = zeros(size(id));

    % check if the remaining a-b-d pairs are in the subspaces of omega%
    for ii = 1:length(id)
        u      = af(id(ii));
        v      = bf(id(ii));
        w      = df(id(ii));
        sol(ii) = inOmega(u,v,scl(zz)*log10(w),A,B,D,NA,NB,ND);
    end

    id_sol = id(sol == 1);

    ID     = [ID;id_sol];
end

ID(1) = [];

end % end of subroutine "check"                                       %
```

```
function IDP = IDPP(bi,di,af,bf,df,wpp,ID,style,g,I)
%  ================================================================  %
%  This subroutine check whether the cell #2 design satisfy the      %
%  requirements from target II                                       %
%  ================================================================  %

switch style

    case 'BD'
        zp   = (1-bi(ID).*bf(ID))/g/I./af(ID);

    case 'BC'
        zp   = (bf(ID).*((-1).*bf(ID)+bi(ID))+(-1).*af(ID).*( ...
               df(ID)+di(ID))).^(-1).*(bf(ID).^2+af(ID).*( ...
               df(ID)+di(ID))).^(-1).*(bf(ID).*bi(ID).*(df( ...
               ID)+(-1).*((-1)+bf(ID).^2+af(ID).*df(ID)).*di( ...
               ID))+(-1).*(df(ID)+di(ID)).*(bf(ID).^2+af( ...
               ID).*(df(ID)+di(ID)))).*I.^(-1).*g.^(-1);
end

IDp   = zp<0|zp>wpp^2;
IDP   = ID(IDp==1);

end % end of the subroutine "IDPP"                                   %
```

```
function [KR,RGBKR] = KR(ai,bi,di,af,bf,df,ID,g,style)
%  ================================================================  %
%  This subroutine calculate the variable stiffness ratio of each    %
%  design contained in ai, bi, di, af, bf, df                         %
%  ================================================================  %
a1     = ai(ID);
b1     = bi(ID);
d1     = di(ID);
a2     = af(ID);
b2     = bf(ID);
d2     = df(ID);

%% calculate the variable stiffness performance                      %
Kc1    = (a1.*d1+b1.^2)/g./a1;      % closed valve cell stiffness     %
Kc2    = (a2.*d2+b2.^2)/g./a2;      % closed valve cell stiffness     %
Ko1    = d1/g;                      % open valve cell stiffness       %
Ko2    = d2/g;                      % open valve cell stiffness       %

switch style
    case 'AC'
        Kc = Kc1.*Kc2./(Kc1+Kc2);
        Ko = Ko1.*Ko2./(Ko1+Ko2);
    case 'BC'
        Kc = Kc1.*Kc2./(Kc1+Kc2);
        Ko = Ko1.*Ko2./(Ko1+Ko2);
    case 'AD'
        Kc = Kc1+Kc2;
        Ko = Ko1+Ko2;
    case 'BD'
        Kc = Kc1+Kc2;
        Ko = Ko1+Ko2;
end

KR     = Kc./Ko;

%% generate the heat map color index                                 %
Rmin   = min(KR);
Rmax   = max(KR);

rgB    = [0 0 255];
Rgb    = [255 0 0];
rGb    = [0 255 0];

rgbKR  = (KR-Rmin)./(Rmax-Rmin);
RGBKR  = zeros(length(rgbKR),3);

for ii = 1:length(rgbKR)
    if rgbKR(ii) <= 0.5
        xrgb = rgbKR(ii)*2;
        RGBKR(ii,:) = rGb*xrgb+rgB*(1-xrgb);
    else
        xrgb = (rgbKR(ii)-0.5)*2;
        RGBKR(ii,:) = Rgb*xrgb+rGb*(1-xrgb);
    end
end

end % end of subroutine "KR"                                         %
```

```
function [SD,RGBSD] = SD(bi,di,bf,df,ID,g,style)
%  ================================================================  %
%  This subroutine calculate the static actuation authority of each   %
%  design contained in ai, bi, di, af, bf, df                         %
%  ================================================================  %
b1     = bi(ID);
d1     = di(ID);
b2     = bf(ID);
d2     = df(ID);

switch style
    case 'AC'
        SD = g*(b1./d1+b2./d2);
    case 'BC'
        SD = g*(b1./d1+b2./d2);
    case 'AD'
        SD = (b1-b2)./(d1+d2)*g;
    case 'BD'
        SD = (b1-b2)./(d1+d2)*g;
end

SDmin  = min(SD);
SDmax  = max(SD);

rgB    = [0 0 255];
Rgb    = [255 0 0];
rGb    = [0 255 0];

rgbSD = (SD-SDmin)./(SDmax-SDmin);
RGBSD = zeros(length(rgbSD),3);

for ii = 1:length(rgbSD)
    if rgbSD(ii) <= 0.5
        xrgb = rgbSD(ii)*2;
        RGBSD(ii,:) = rGb*xrgb+rgB*(1-xrgb);
    else
        xrgb = (rgbSD(ii)-0.5)*2;
        RGBSD(ii,:) = Rgb*xrgb+rGb*(1-xrgb);
    end
end

end % end of the subroutine "SD"                                      %
```

Reference

Anderson CT, Carrol A, Akhmetova L and Somerville C (2010) Real-time imaging of cellulose reorientation during cell wall expansion in Arabidopsis roots. *Plant Physiology* 152(2): 787-796.

Balmer RT and Franks JG (1975) Contractile characteristics of mimosa pudica L. *Plant Physiology* 56(4): 464-467.

Bar-Cohen Y (2005) *Biomimetics: Biologically Inspired Technologies* 1st ed. CRC Press.

Baskin TI (2005) Anisotropic expansion of the plant cell wall. *Annual Review of Cell and Developmental Biology* 21: 203-222.

Burgert I and Fratzl P (2009) Actuation systems in plants as prototypes for bio-inspired devices. *Philosophical Transactions of the Royal Society A: Mathematical, Physical and Engineering Sciences* 367(1893): 1541-1557.

Cave ID and Hutt L (1968) The anisotropic elasticity of the plant cell wall. *Wood Science and Technology* 2: 268-278.

Chandra R, Singh S P and Gupta K (1999) Damping studies in fiber-reinforced composites–a review. *Composite structures* 46(1): 41-51.

Chou, CP and Hannaford B (1996) Measurement and modeling of McKibben pneumatic artificial muscles. *IEEE Transactions on Robotics and Automation* 12(1): 90-102.

Chu MT and Golub GH (2005) *Inverse Eigenvalue Problems: Theory, Algorithms, and Applications*. New York: Oxford University Press.

Cosgrove DJ (2005) Growth of the plant cell wall. *Nature Reviews Molecular Cell Biology* 6(11): 850-861.

Davis S, Tsagarakis N, Canderle J and Galdwell DG (2003) Enhanced modelling and performance in braided pneumatic muscle actuators. *Journal of Robotics Research*, 22(3-4): 213-227.

Dawson C, Vincent JFV and Rocca AM (1997) How pine cones open. *Nature* 390 (6661): 668-668.

Dumais J and Forterre Y (2012) "Vegetable dynamics": *The role of water in plant movements Annual Review of Fluid Mechanics* 44: 453-478.

Elbaum R, Zaltzman L, Burgert I and Fratzl P (2007) The role of wheat awns in the seed dispersal unit. *Science* 316(5826): 884-886.

Forterre Y, Skotheim JM, Dumais J, and Mahadevan L (2005) How the venus flytrap snaps. *Nature* 433(7024): 421-425.

Fratzl P (2003) Cellulose and collagen: from fibres to tissues. *Current opinion in colloid & interface science* 8(1): 32-39.

Fratzl P, Burgert I and Keckes J (2004) Mechanical model for the deformation of the wood cell wall. *Zeitschrift Fur Metallkunde*, 95(7): 579-584.

Fratzl P, Elbaum R and Burgert I (2008) Cellulose fibrils direct plant organ movements. *Faraday Discussions* 139: 275.

Gladwell GML (2006) Minimal mass solutions to inverse eigenvalue problems. *Inverse Problems* 22(2): 539-551.

Hald OH (1976) Inverse eigenvalue problems for Jacobi matrices. *Linear Algebra and its Applications* 14(1): 63-85.

Harrington MJ, Razghandi K, Ditsch F, Guiducci L, Rueggeberg M, Dunlop JWC, Fratzl P, Neinhuis C and Burgert I (2011) Origami-like unfolding of hydro-actuated ice plant seed capsules. *Nature Communications*, 2: 337.

Hill BS and Findlay GP (2009) The power of movement in plants: the role of osmotic machines. *Quarterly reviews of biophysics* 14(02): 173.

Hubbard JH and Hubbard BB (2001) *Vector Calculus, Linear Algebra, and Differential Forms: A Unified Approach* 2nd ed. Prentice Hall.

Joseph KT (1992) Inverse eigenvalue problem in structural design. *AIAA Journal* 30(12): 2890-2896.

Kang BS, Kothera CS, Woods BKS and Wereley NM (2009) Dynamic modeling of Mckibben pneumatic artificial muscles for antagonistic actuation. *Proc. In IEEE International Conference on Robotics and Automation* 182-187.

Kim, GW, Li S and Wang KW (2010) Variable stiffness actuator based on fluidic flexible matrix composites and piezoelectric-hydraulic pump. *Proc. In Proceedings of SPIE Conference* 7643-76431Y-1.

Kuiken GDC (1984) Wave propagation in a thin-walled liquid-filled initially stressed tube. *Journal of Fluid Mechanics* 141: 289-308.

Lekhnitskii SG (1963) *Theory of Elasticity of an Anisotropic Body* 1st ed. Holden-Day Inc.

Li S and Wang KW (2012) Learning from plants - recent advances in fluidic flexible matrix composite based multi-cellular and multi-functional adaptive structures. *Plants and Mechanical Motion: a Synthetic Approach to Nastic Materials and Structures* DES-tech Publications Inc 115-140.

Li S, Lotfi A, Shan Y, Wang KW, Rahn CD and Bakis CE (2008) A variable transverse stiffness sandwich structure using fluidic flexible matrix composite (F^2MC). *Proc. In Proceedings of SPIE Conference* 69280M-1.

Lotfi A, Scarborough LH, Rahn CD, Smith EC (2012) Passive and switched stiffness vibration controllers using fluidic flexible matrix composites. *Journal of Vibration and Acoustics* 134: 021001.

Luo E, Radebaugh R, Dai W, Lewis M, Wu Z and Zhang Y (2005) Thermoacoustic turbulent-flow model for inertance tubes used for pulse tube refrigerators. *In International Cryogenic Engineering Conference* 383-386.

Luo Q and Tong L (2013a) Adaptive pressure-controlled cellular structures for shape morphing I: design and analysis. *Smart Materials and Structures* 22(5): 055014.

Luo Q and Tong L (2013b) Adaptive pressure-controlled cellular structures for shape morphing: II. numerical and experimental validation. *Smart Materials and Structures*, 22(5): 055015.

Martone PT, Boller M, Burgert I, Dumais J, Edward J, Mach K, Rowe N, Rueggeberg M, Seidel R and Speck T (2010) Mechanics without muscle: biomechanical inspiration from the plant world. *Integrative and Comparative Biology* 50(5): 888-907.

Mechel FP (2002) *Formulas of Acoustics* 1st ed. New York: Springer.

Merritt HE (1991) *Hydraulic Control Systems* 1st ed. Wiley.

Niklas KJ (1992) *Plant Biomechanics: An Engineering Approach to Plant Form and Function* 1st ed. Chicago: University Of Chicago Press.

Pagitz M and Bold J (2013) Shape changing shell-like structures. *Bioinspiration & Biomimetics*, 8(1): 016010.

Pagitz M, Lamacchia E and Hol JMAM (2012) Pressure-actuated cellular structures. *Bioinspiration & Biomimetics*, 7(1): 016007.

Palacios J (1964) *Dimensional Analysis* 1st ed. London: Macmillan.

Philen MK (2012a) Fluidic flexible matrix composite semi-active vibration isolation mounts. *Journal of Intelligent Material Systems and Structures* 23(3) 353-363.

Philen MK (2012b) Force tracking control of fluidic flexible matrix composite variable stiffness structures. *Journal of Intelligent Material Systems and Structures* 22(1): 31-43.

Philen MK (2009) On the applicability of fluidic flexible matrix composite variable impedance materials for prosthetic and orthotic devices. *Smart Materials and Structures* 18(10): 104023.

Philen MK, Shan Y, Prakash P, Wang KW, Rahn CD, Zydney AL and Bakis CE (2007) Fibrillar network adaptive structure with ion-transport actuation. *Journal of Intelligent Material Systems and Structures*, 18(4): 323-334.

Pontecorvo ME, Barbarino S and Gandhi FS (2012) Cellular honeycomb like structures with internal inclusions in the unit cell. *Proc. In ASME Conference on Smart Materials, Adaptive Structures and Intelligent Systems* SMASIS2012-8075

Puttmann J, Beblo R, Joo J, Smyers B and Reich G (2012) Design of a morphing skin by optimizing a honeycomb structure with a two phase material infill. *In ASME Conference on Smart Materials, Adaptive Structures and Intelligent Systems* SMASIS2012-8131

Ramrakhyani DS, Lesieutre GA, Frecker M and Bharti S (2005) Aircraft structural morphing using tendon-actuated compliant cellular trusses. *Journal of Aircraft* 42(6): 1615–1621.

Reynolds DB. Repperger DW, Phillips CA and Bandry G (2003) Modeling the dynamic characteristics of pneumatic muscle. *Annals of Biomedical Engineering* 31(3): 310-317.

Richmond PA, Metraux JP and Taiz L (1980) Cell expansion patterns and directionality of wall mechanical proterties in *Nitella*. *Plant Physiology* 65: 211-217.

Scarborough LH, Rahn CD and Smith EC (2012) Fluidic composite tunable vibration isolators. *Journal of Vibration and Acoustics*, 134(1): 011010.

Schenk M and Guest SD (2013) Geometry of Miura-folded metamaterials. *Proceedings of the National Academy of Sciences*, 110(9): 3276–3281.

Shan Y (2006) *Flexible Matrix Composites: Dynamic Characterization, Modeling, and Potential for Drivershaft Applications*. State College: The Pennsylvania State University.

Shan Y, Philen M, Lotfi A, Li S, Bakis CE, Rahn CD and Wang KW (2008) Variable stiffness structures utilizing fluidic flexible matrix composites. *Journal of Intelligent Material Systems and Structures* 20(4): 443-456.

Skotheim JM and Mahadevan L (2005) Physical limits and design principles for plant and fungal movements. *Science* 308(5726): 1308-1310.

Stahlberg R and Taya M (2006) Nastic structures: The enacting and mimicking of plant movements. *Biomemetics: Biologically inspired technologies*, 1st ed. CRC Press 473-491

Sun C (1988) Three-dimensional effective elastic constants for thick laminates *Journal of Composite Materials* 22: 629-639

Tondu B and Lopez P (2000) Modeling and control of McKibben artificial muscle robot actuators. *Control Systems, IEEE*, 20(2): 15–38.

Ueda J, Secord TW and Asada HH (2010) Large effective-strain piezoelectric actuators using nested cellular architecture with exponential strain amplification mechanisms. *IEEE/ASME Transactions on Mechatronics* 15(5): 770-782.

Vasista S and Tong L (2012) Design and testing of pressurized cellular planar morphing sructures. *AIAA Journal* 50(6): 1328-1338.

Volkov AG, Foster JC and Markin VS (2010a) Signal transduction in mimosa pudica: biologically closed electrical circuits. *Plant, Cell & Environment* 33(5): 816-827.

Volkov AG, Foster JC, Ashby TA, Walker RK, Johnson JA and Markin VS (2010b) Mimosa pudica: electrical and mechanical stimulation of plant movements. *Plant, Cell & Environment* 33(2): 163-173.

Vos R, Barrett R and Romkes A (2011) Mechanics of pressure-adaptive honeycomb. *Journal of Intelligent Material Systems and Structures* 22(10): 1041-1055.

Wagg D, Bond I, Weaver P and Friswell M (2008) *Adaptive Structures*. John Wiley and Sons.

Watton J (1989) *Fluid Power Systems: Modeling, Simulation, Analog and Microcomputer Control*. Prentice Hall.

Zhang Z and Philen MK (2012) Pressurized artificial muscles. *Journal of Intelligent Material Systems and Structures*, 23(3): 255-268.